Stratospheric Composition Measurements in the Arctic and at Mid-latitudes and Comparison with Chemical Fields from Atmospheric Models

by

Elham Farahani

A thesis submitted in conformity with the requirements
for the degree of Doctor of Philosophy
Graduate Department of Physics
University of Toronto

Abstract

Stratospheric Composition Measurements

in the Arctic and at Mid-latitudes

and Comparison with

Chemical Fields from Atmospheric Models

Elham Farahani

Doctor of Philosophy

Graduate Department of Physics

University of Toronto

2006

The purpose of this research is to contribute to our understanding of the processes determining the Arctic stratospheric ozone budget by deploying an ultraviolet-visible spectrometer at the Arctic Stratospheric Ozone Observatory (AStrO) located at Eureka, NU (80.1ºN, 86.4ºW). For four years, O_3 columns, NO_2 vertical columns and profiles, and OClO slant columns (in 2000) were measured during polar spring. The spectrometer was also deployed in Vanscoy, SK (52ºN, 107ºW) in 2000 and 2002 as part of the Middle Atmosphere Nitrogen TRend Assessment (MANTRA) project. The resulting O_3 columns were compared with Brewer, TOMS and GOME data. The NO_2 columns, NO_2 reference column density (RCD) and NO_2 diurnal variability were also determined.

The Arctic measurements were analysed in detail and combined with infrared Fourier transform spectrometer measurements at AStrO and with HNO_3 measurements at Thule, Greenland (76.5ºN, 68.8ºW) and Kiruna, Sweden (67.8ºN, 20.4ºE) (in 2001-2002). To assess the chemical fields of atmospheric models, the observational data set was compared with chemical fields from the Canadian Middle Atmosphere Model (CMAM) and SLIMCAT, a 3D Chemical Transport Model.

The comparison of CMAM with measurements made during the warm Arctic winters

(1999, 2001, 2002 and 2003) provided an excellent opportunity to test the model simulations under PSC-free conditions. Generally, the CMAM inter-annual variability is small and does not fully cover the range of the observed variability. SLIMCAT O_3 columns were generally higher than the observed values. Comparison with O_3 profiles from sondes indicated that O_3 mixing in the lower stratosphere was too fast in SLIMCAT.

A sensitivity study on the contributions of NO_2 RCD uncertainty to the retrieval of NO_2 profiles showed that a 10% uncertainty in the RCD changes the retrieved profile by 5-10% at northern high latitudes.

This project extended the temporal-geographical range of polar stratospheric observations and strengthened Canadian capabilities in monitoring the mid-latitude and particularly the Arctic stratosphere. As part of an ongoing research program, it will provide a long-term data set in the Canadian High Arctic, which can be used for future trend analysis.

Dedication

To you, my loving mom and dad

for surrounding me with limitless love

for besieging me with endless joy

To you, Sir $\bar{\text{A}}$K Emami

for teaching me how to glance at light,

how to touch love and to live life

Acknowledgements

Contents

List of Tables

List of Figures

xiv

xvi

List of Acronyms

AASE: Airborne Arctic Stratospheric Experiment

ACE-FTS: Atmospheric Chemistry Experiment Fourier Transform Spectrometer

AERI: Atmospheric Emission Radiometric Interferometer

AMF: Air Mass Factor

AStrO: Arctic Stratospheric Ozone observatory

ATMOS: Atmospheric Trace Molecule Spectroscopy experiment

BBL: Beer-Bouguer-Lambert law

BUV: Backscatter Ultraviolet

CANDAC: Canadian Network for the Detection of Atmospheric Change

CCCma: Canadian Centre for Climate modeling and analysis

CFC: Chlorofluorocarbon

CHEOPS: Chemistry of Ozone in the Polar Stratosphere

CMAM: Canadian Middle Atmosphere Model

CTM: Chemical Transport Model

DNA: DeoxyriboNucleic Acid

DOAS: Differential Optical Absorption Spectroscopy

DOD: Differential Optical Depth

DSCD: Differential Slant Column Density

DTCM: Diabatic Trajectory-Chemistry Model

DU: Dobson Unit

DU AERI-X: Denver University Atmospheric Emission Radiometric Interferometer

EASOE: European Arctic Stratospheric Ozone Experiment

ECMWF: European Centre for Medium-Range Weather Forecasts

ENVISAT: Environmental Satellite

EOS-AURA: Earth Observaing System - Association of Universities for Research in Astronomy

ERS: European Remote Sensing satellite

FOV: Field of View

FWHM: Full Width at Half Maximum

GCM: General Circulation Model

GHG: Greenhouse Gas

GOME: Global Ozone Monitoring Experiment

GOMOS: Global Ozone Monitoring by Occultation of Stars

HALOE: Halogen Occultation Experiment

HCFC: Hydrochlorofluorocarbon

HIRDLS: High Resolution Dynamics Limb Sounder

InSb: Indium Antimonide

IR: Infrared

IPV: Inter-Pixel Variability

KOPRA: Karlsruhe Optimized Precise Radiative transfer Algorithm

LLG: Liquid Light Guide

MAESTRO: Measurement of Aerosol Extinction in the Stratosphere and Troposphere
                 Retrieved by Occultation

MANTRA: Middle Atmosphere Nitrogen TRend Assessment

MCT: Mercury Cadmium Telluride

MIPAS: Michelson Interferometer for Passive Atmospheric Sounding

MLS: Microwave Limb Sounder

MOS: Metal Oxide Semiconductor

MSC FTS: Meteorological Service of Canada Fourier Transform Spectrometer

NAT: Nitric Acid Trihydrate

NCAR: National Center for Atmospheric Research

NCEP/CPC: National Centers for Environmental Prediction/Climate Prediction Cen-
                 ter

NDSC (NDACC): Network for the Detection of Stratospheric Change (Network for the
                 Detection of Atmospheric Composition Change)

NLLS: Non-Linear Least Squares

OEM: Optimal Estimation Method

OMI: Ozone Monitoring Instrument

OPD: Optical Path Difference

OSIRIS: Optical Spectrograph and Infrared Imager System

ppbv: parts per billion by volume

ppmv: parts per million by volume

PROFFIT: PROFile FIT

PSC: Polar Stratospheric Cloud

PV: Potential Vorticity

QBO: Quasi-Biennial Oscillation

RCD: Reference Column Density

RT: Radiative Transfer

RTE: Radiative Transfer Equation

SAGE: Stratospheric Aerosol Gas Experiment

SAOZ: Systeme D'analyse par observations Zénithales

SBUV: Solar Backscatter Ultraviolet

SCIAMACHY: Scanning Imaging Absorption Spectrometer for Atmospheric Chartography

SCISAT: Science Satellite

SESAME:	Second European Arctic and Midlatitude Experiment
SMR:	Submillimeter Radiometer
SNR:	Signal-to-Noise Ratio
SOLVE:	SAGE Ozone Loss Validation Experiment
SST:	Sea-Surface Temperature
STP:	Standard Temperature Pressure
STS:	Supercooled Ternary Solution
SZA:	Solar Zenith Angle
THESEO:	Third European Stratospheric Experiment on Ozone
TOMS:	Total Ozone Mapping Spectrometer
TTL:	Tropical Tropopause Layer
UARS:	Upper Atmospheric Research Satellite
UT GBS:	University of Toronto Ground-Based Spectrometer
UV:	Ultraviolet
VCD:	Vertical Column Density
VMR:	Volume Mixing Ratio

Chapter 1

Introduction

Ozone (O_3) is one of the most important atmospheric constituents chemically and radiatively. Stratospheric O_3 is located in a layer of the atmosphere mainly between 20 and 40 km, while its peak mixing ratio of 8 to 10 parts per million by volume (ppmv) occurs around 30-35 km, as shown in Figure 1.1 (*Dessler*, 2000). Ozone's role as an ultraviolet (UV) filter is crucial in sustaining life in the biosphere. On average, less than 10% of the solar energy incident on the top of the Earth's atmosphere is in the UV spectral region (100-400 nm) (*ACIA*, 2005).

While atmospheric oxygen (O_2) and O_3 almost entirely absorb photons in the wavelength range 100-280 nm (referred to as UV-C radiation), photons in the wavelength range 280-320 nm (UV-B radiation) are absorbed efficiently but not entirely by atmospheric O_3. UV-B photons have enough energy to harm human beings, ecosystems and materials once they reach the Earth's surface (*UNEP*, 1998). UV-B photons can cause corneal damage, cataracts, immune suppression, aging of the skin, erythema and even break the bonds of DNA molecules (*UNEP*, 2003). Generally, living cells are able to repair the damaged DNA, although sometimes the damaged DNA molecules can replicate which is the cause of dangerous forms of skin cancer (*Newman*, 1998). UV-A photons (320-400 nm) are absorbed by atmospheric O_3 in small amounts compared to the UV-C
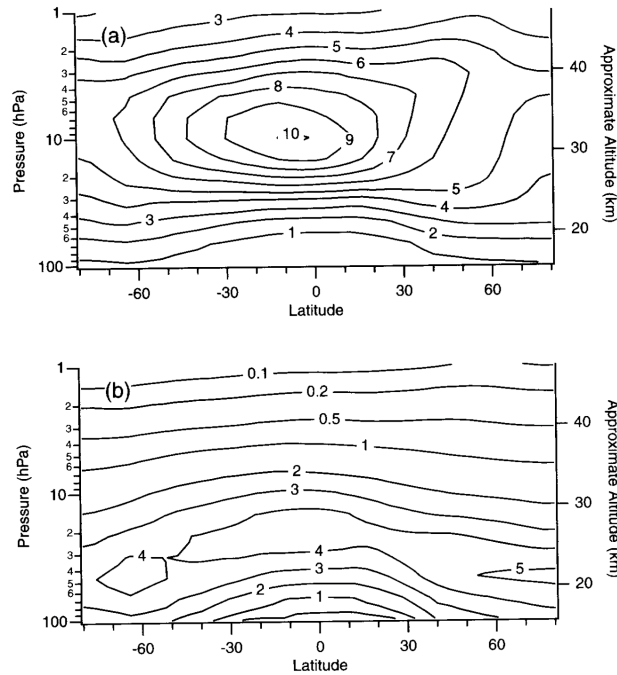
Figure 1.1: Contours of (a) average zonal-mean O_3 volume mixing ratio (VMR) (ppmv) and (b) average zonal-mean O_3 number density (10^{12} molec/cm^3) in the latitude-altitude plane in December 1992. Data are from the UARS Reference Atmosphere Project. O_3 reaches maximum values of both VMR (10 ppmv at $\sim$32 km) and number density (4.6×10^{12} molec/cm^3 at $\sim$25 km) over the equator (reproduced from *Dessler*, 2000).

and UV-B photons. At the same time, UV-A photons are low-energy photons compared to UV-C and UV-B photons, which makes them less harmful (*ACIA*, 2005).

In general, the gravitational force of the Earth holds the Earth's atmosphere in place and causes the density (mass per unit volume), ρ, and thus the pressure, p, to decrease exponentially with altitude, z, according to the hydrostatic equation:

$$p(z) = p(z_0)exp\left(-\frac{z - z_0}{H}\right) \tag{1.1}$$

where H is the atmospheric scale height and is defined as:

$$H = \frac{RT}{g} \tag{1.2}$$

where R is the ideal gas universal constant, equal to 287 JK^{-1}kg^{-1}, T is the temperature

in Kelvin (assumed constant) and g is the gravitational acceleration, equal to 9.80665 ms^{-2} (*Brasseur et al.*, 1999).

The atmosphere is divided into several layers according to the changes in temperature with altitude as seen in Figure 1.2 (*Brasseur et al.*, 1999). The stratosphere is characterized by increasing temperature with increasing altitude and extends from the tropopause, the transition region in which temperature reaches a minimum, located between about 10 and 15 km altitude ($\sim$100-200 hPa in pressure coordinates), to the stratopause, another transition region in which temperature reaches a maximum, and located near 50 km altitude ($\sim$1 hPa in pressure coordinates). As shown in Figure 1.1, the O_3 peak both in volume mixing ratio (VMR) and number density is in the stratosphere, where it plays a vital role in the energy balance in this region. By absorbing solar UV and visible photons as well as the Earth's thermal radiation around 9.6 μm, O_3 largely determines the shape of the stratospheric temperature profile and the resulting stability of the stratosphere. Therefore, any change in the concentration of stratospheric O_3 has the potential to affect the climate and life on the Earth (*Dessler*, 2000; *Brasseur et al.*, 1999).

1.1   Ozone - Historical Context

In 1930, Chapman proposed the first photochemical theory for the formation of atmospheric O_3 through photolysis of molecular oxygen (O_2) by UV radiation, although this theory overestimated the observed mixing ratios of O_3 (*Chapman*, 1930). In the 1970s and 1980s, our understanding of the interactions of the odd-nitrogen, hydrogen, oxygen and halogen families and their effects on O_3 abundance was improved based on a consideration of homogeneous gas-phase processes and thanks to studies done on the HO_x radical by *Hampson* (1964), on nitrogen compounds by *Crutzen* (1970), on chlorine compounds by *Cicerone et al.* (1974) and on chlorofluorocarbons (CFCs) by *Molina and Rowland* (1974).
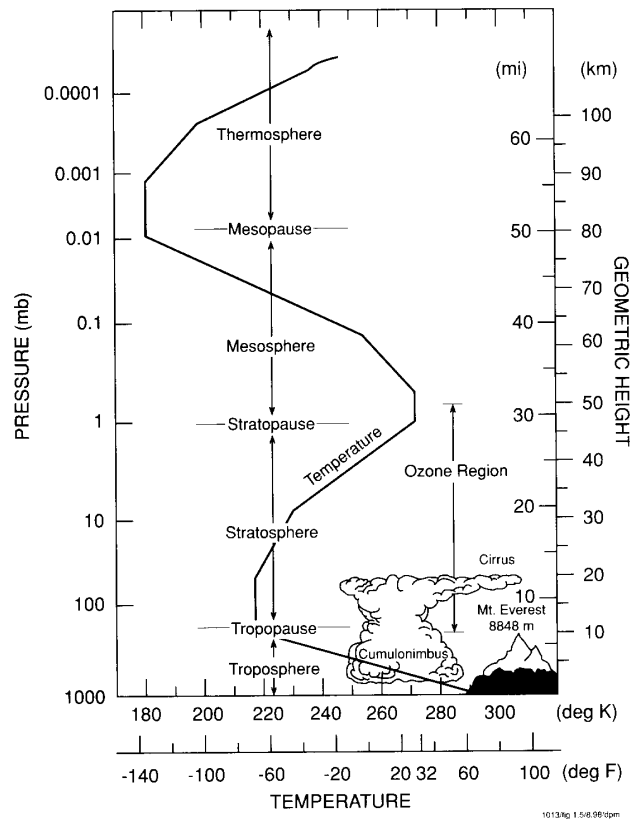
Figure 1.2: Vertical profile of the temperature between the surface and 100 km altitude as defined in the U.S. Standard Atmosphere (1976), and related atmosphere layers (*Brasseur et al.*, 1999).

In 1985, *Farman et al.* (1985) reported the first observations of the extreme decline in the total O_3 column above Halley Bay, Antarctica. This phenomenon was named the *ozone hole*, and was seen in the springtime total O_3 column, which declined from 320 DU (1 Dobson Unit (DU) is defined to be 0.01 mm thickness at STP) to less than 200 DU over the period 1979-1985. The results of *Farman et al.* were confirmed by TOMS satellite data, which showed that from September to November, the O_3 depletion occurred over a very extended region of Antarctica (*Stolarski et al.*, 1986; *Solomon et al.*, 1986). The springtime Antarctic ozone hole has persisted, with minimum values around 100 DU, since the early 1990s (*WMO*, 2003). Seventy percent of the total column O_3 was disappearing over the Antarctic by 1989 during the months of September and early October (*Deshler et al.*, 1992). Such loss means removal of 3% of the global ozone in a period of six weeks and shows how fast the state of the atmosphere can change (*Anderson et al.*, 1991). In recent years, meteorological observations report more persistent Antarctic vortices, which last until early December, whereas in the period from 1970 to 1980, the vortex usually broke up in late November (*Randel and Wu*, 1999; *WMO*, 2003) with the exception of the 2002 Antarctic vortex which was unusually weak and warm due to large planetary wave activity in winter stratosphere (*Allen et al.*, 2003).

The discovery of the ozone hole over Antarctica raised concerns over the possibility of similar O_3 losses in the Arctic. The evolution of O_3 and other related atmospheric species such as some in the chlorine and nitrogen families have been observed over the Arctic for more than two decades by several satellite instruments. In particular, long-term polar ozone measurements from space started with the Nimbus 4 BUV instrument followed by TOMS on board Nimbus 7 (*Fleig et al.*, 1986). Later versions of TOMS, as well as other instruments such as MLS on UARS (*Jackman and Douglass*, 2003) and GOME on ERS-2 (*Burrows et al.*, 1999b), collectively have observed the evolution of O_3 for more than two decades. More recently, a new generation of satellite instruments such as GOMOS, MIPAS and SCIAMACHY on ENVISAT (*Wehr*, 2002); OSIRIS and SMR

on Odin (*Murtagh et al.*, 2002); MAESTRO and ACE-FTS on SCISAT-1 (*Bernath et al.*, 2005); and OMI, HIRDLS and MLS aboard EOS-AURA (*Schoeberl et al.*, 2006) provide measurements of ozone and many other species which provide insight into processes causing changes in the O_3 concentration and improve the observation quality compared to the previous generation of instruments.

Also, a series of field campaigns, started in the late 1980s, were undertaken to study a number of aspects of ozone changes in the Arctic. Some of the pioneering work was done during AASE (*Henriksen et al.*, 1994) in 1988-1989, which continued during CHEOPS I-III in 1988-1990 (*Pommereau and Schmidt*, 1991); EASOE (*Pyle et al.*, 1994) and AASE II in 1991-1992 (*Anderson and Toon*, 1993); SESAME (*de Valk et al.*, 1997) in 1994-1995; SOLVE and THESEO in 2000 (*Newman et al.*, 2002) and the recent ACE Arctic validation campaigns in spring 2004, 2005, and 2006 (*Kerzenmacher et al.*, 2005). Meanwhile, several kinds of models have been developed to study the Earth's atmosphere, in particular, ozone depletion in the Arctic; these include trajectory models (*Pierce and Fairlie*, 1993), trajectory-chemistry models (*Becker et al.*, 2000), diabatic trajectory-chemistry model (DTCM) (*Lukyanov et al.*, 2003), and three-dimensional chemical transport models (3D-CTM) (*Lefevre et al.*, 1994; *Chipperfield*, 1999).

Analysis of TOMS data from 1979 to 1991 revealed O_3 column trends of -1 to -1.5 DU yr^{-1} in early winter, which reached -2 to -2.5 DU yr^{-1} by March (O_3 losses were averaged in PV coordinates) (*Randel and Wu*, 1995). *Fioletov et al.* (2002) reported a trend of -4% per decade in the mean spring Arctic ozone column in the latitude band of 60º-80º N in the period from 1979 to 2000. The O_3 total column trends again changed, when the large estimates of Arctic ozone chemical depletion during the cold winters of 1990s were considered together with negligible chemical loss during recent warm winters (*Proffitt et al.*, 1990; *Hofmann and Deshler*, 1991; *Manney et al.*, 1995; *Müller et al.*, 1997; *Rex et al.*, 1997, 1999). In general, ozone trends in the Arctic are smaller than in the Antarctic, mostly due to the differences between the polar stratospheric vortices

(*Manney et al.*, 1994). In the Antarctic, the vortex and the cold temperatures within it persist longer into spring than is the case with the less circular and generally weaker and warmer Arctic vortex. The combination of low temperatures ($\leq$196 K) and sunlight, which allows rapid destruction of ozone, occurs to a much greater extent in Antarctica than in the Arctic (*WMO*, 2003).

Since it has been confirmed that Arctic ozone chemical depletion is closely coupled with temperature variation (*WMO*, 2003), Arctic ozone studies have focused on minimum and average stratospheric temperatures. Indications of a slight cooling, which is barely significant, were found in satellite and radiosonde observations (*WMO*, 2003; *Ramaswamy et al.*, 1994; *Lanzante et al.*, 2003) while the average area extent of Polar Stratospheric Cloud (PSC) conditions has increased over the past four decades. *Rex et al.* (2004) concluded that in the cold years, the potential for PSC existence throughout the winter has increased in the past 40 years in a manner consistent with ozone loss estimates. Several studies suggest increased persistence of the springtime Arctic vortex (*Waugh and Randel*, 1999; *Offermann et al.*, 2004). On the other hand, the recent warm winters in the Arctic (*Manney et al.*, 2005) together with evidence for a stronger, colder vortex regime in the late 1970s (*Christiansen*, 2003) raise the possibility of a shift back to a more disturbed Arctic regime.

In addition to the uncertainties in and inconsistent results of current studies, coupled chemistry-climate model simulations generate different pictures in the Arctic. Some climate model simulations result in more disturbed Arctic vortices in future due to an increase in planetary wave activity and suggest that this dynamical heating will balance the radiative cooling due to the increase in greenhouse gas (GHG) concentrations. Therefore, the recovery of the ozone layer in the Arctic could be expected in a reduced-chlorine stratosphere (*Schnadt et al.*, 2002; *Schnadt and Dameris*, 2003). However, other climate model simulations suggest that observed changes in ozone and GHG concentrations may not be enough to explain the cooling trends in the Northern Hemisphere lower strato-

sphere and dynamic strengthening of the polar vortex seems to be required to match observed cooling rates (*Austin et al.*, 2003; *WMO*, 2003; *Shindell*, 2003). Thus, in the Arctic where the detection of any trend is difficult due to large inter-annual and intra-seasonal variability; the winter stratosphere is considered to be at a threshold where ozone losses are predicted in cooler conditions (*Chipperfield and Pyle*, 1998; *Tabazadeh et al.*, 2000; *WMO*, 2003).

1.2   Basic Concepts in Stratospheric Chemistry

1.2.1   Gas Phase Ozone Chemistry

O_3 formation is a two-step process described by the Chapman cycle, which is also the cycle responsible for the increase of temperature with altitude in the stratosphere. In the first step we have the photolysis of molecular oxygen (O_2) by solar photons at wavelengths less than 242 nm (Reaction 1.3) followed by the reaction between atomic (O) and molecular oxygen (O_2) in a three-body reaction to create O_3:

$$O_2 + h\nu \quad \rightarrow \quad O + O \tag{1.3}$$

$$2 \times (O + O_2) \quad \xrightarrow{\text{M}} \quad 2 \times O_3 \tag{1.4}$$

$$net: 3 \times O_2 \quad \rightarrow \quad 2 \times O_3 \tag{1.5}$$

M represents a third molecule (usually N_2) which removes the excess energy in the chemical reaction. As O and O_3 cycle very rapidly between one another, we refer to O+O_3 as the odd oxygen family, denoted by O_x. Other Chapman reactions that control the concentration of the odd oxygen family are (*Chapman*, 1930):

$$O_3 + h\nu \quad \rightarrow \quad O + O_2 \tag{1.6}$$

$$O + O_3 \quad \rightarrow \quad O_2 + O_2 \tag{1.7}$$

$$O + O \quad \xrightarrow{\text{M}} \quad O_2 \tag{1.8}$$

where the wavelengths of solar photons in Reaction 1.6 are less than 336 nm. The above reactions cannot explain observed O_3 levels (which are lower than predicted by the Chapman cycles) because Reaction 1.6 is too slow to balance the rate of O_3 production (*Wayne*, 1991). Stratospheric O_3 is chemically destroyed not only by Reactions 1.7 and 1.8 but also by radical catalysis. The following chemical reaction sequence describes the catalytic cycles:

$$X + O_3 \quad \rightarrow \quad XO + O_2 \tag{1.9}$$

$$XO + O \quad \rightarrow \quad X + O_2 \tag{1.10}$$

$$net : O + O_3 \quad \rightarrow \quad 2 \times O_2 \tag{1.11}$$

where X can be NO (*Crutzen*, 1970; *Johnston*, 1971), Cl (*Molina and Rowland*, 1974), and H or OH (*Hampson*, 1964). X is the catalyst and by definition the catalyst increases the reaction rate without being consumed, thus even a small amount of X can destroy many O_3 molecules.

Other important catalytic O_x loss cycles in the Arctic stratosphere are those involving ClO and BrO (*Solomon et al.*, 1986). OClO is important in stratospheric O_3 chemistry since it can be used as an indicator for stratospheric chlorine activation. Measurements of OClO can address open questions like the duration of chlorine activation, its dependence on the abundance of nitrogen oxides or the influence of stratospheric mountain waves (*Kühl et al.*, 2004). In the winter polar stratosphere, the only important reaction that forms OClO is the reaction of ClO and BrO (*Canty et al.*, 2005).

$$ClO + BrO \quad \rightarrow \quad OClO + Br \qquad 59\% \tag{1.12}$$

$$ClO + BrO \quad \rightarrow \quad ClOO + Br \qquad 34\% \tag{1.13}$$

$$ClO + BrO \quad \rightarrow \quad BrCl + O_2 \qquad 7\% \tag{1.14}$$

If the reaction between ClO and BrO follows the path of Reaction 1.12, we have the

following sequence which results in no net O_x loss:

$$Cl + O_3 \rightarrow ClO + O_2 \tag{1.15}$$

$$Br + O_3 \rightarrow BrO + O_2 \tag{1.16}$$

$$ClO + BrO \rightarrow OClO + Br \tag{1.17}$$

$$OClO + h\nu \rightarrow ClO + O \tag{1.18}$$

$$net: O_3 + h\nu \rightarrow O_2 + O \tag{1.19}$$

while the other two reactions, 1.13 and 1.14, result in net loss of O_x through the following reactions, respectively:

$$Cl + O_3 \rightarrow ClO + O_2 \tag{1.20}$$

$$Br + O_3 \rightarrow BrO + O_2 \tag{1.21}$$

$$ClO + BrO \rightarrow ClOO + Br \tag{1.22}$$

$$ClOO \xrightarrow{M} Cl + O_2 \tag{1.23}$$

$$net: 2 \times O_3 \rightarrow 3 \times O_2 \tag{1.24}$$

$$Cl + O_3 \rightarrow ClO + O_2 \tag{1.25}$$

$$Br + O_3 \rightarrow BrO + O_2 \tag{1.26}$$

$$ClO + BrO \rightarrow BrCl + O_2 \tag{1.27}$$

$$BrCl + h\nu \rightarrow Br + Cl \tag{1.28}$$

$$net: 2 \times O_3 \rightarrow 3 \times O_2 \tag{1.29}$$
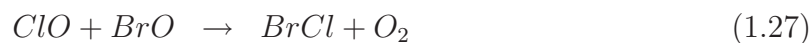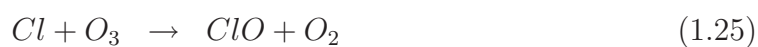
Another catalytic O_x loss cycle which was discovered through laboratory measurements

is the ClO dimer (ClOOCl) catalytic cycle shown below:

$$2 \times (Cl + O_3) \quad \rightarrow \quad 2 \times (ClO + O_2) \tag{1.30}$$

$$ClO + ClO \quad \overset{M}{\rightarrow} \quad ClOOCl \tag{1.31}$$

$$ClOOCl + h\nu \quad \rightarrow \quad ClOO + Cl \tag{1.32}$$

$$ClOO \quad \overset{M}{\rightarrow} \quad Cl + O_2 \tag{1.33}$$

$$net : 2 \times O_3 \quad \rightarrow \quad 3 \times O_2 \tag{1.34}$$
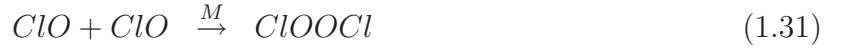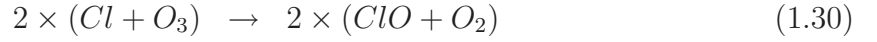
Total odd nitrogen (NO_y=NO+NO_2+NO_3+$ClONO_2$+$2N_2O_5$ +HNO_3+HO_2NO_2+ $BrONO_2$), also plays a crucial role in the photochemistry of polar lower-stratospheric O_3 in the winter and early spring because it is the moderator of chemical O_3 depletion during warm winters, while during cold Arctic winters, it can be removed by large PSC particles and sediment out of the stratosphere (denitrification) (*Fahey et al.*, 1990; *Kondo et al.*, 2000; *Santee et al.*, 2000; *Popp et al.*, 2001), which significantly increases the rate of Arctic chemical O_3 depletion (*Chipperfield and Pyle*, 1998; *Waibel et al.*, 1999; *Tabazadeh et al.*, 2000). Additionally, NO_y can be used as a diagnostic of transport processes as it is brought into the vortex by mixing across the polar vortex edge or downward vertical transport.

Active nitrogen (NO_x= NO+NO_2) can either enhance or moderate O_3 depletion, depending on altitude. NO_x is the agent which shuts down the O_3 destruction catalytic cycles by converting odd chlorine and bromine molecules into their benign reservoir forms below 25 km (*Dessler*, 2000). Nitrogen dioxide (NO_2) has been known as an important atmospheric constituent in controlling stratospheric O_x since 1970 (*Crutzen*, 1970; *Crutzen and Brühl*, 2001; *Akiyoshi et al.*, 2004). The reactions involving NO_x form a catalytic O_x loss cycle between 25 and 40 km that results from production of NO and O_2 in the

photolysis of NO_3, via one of two reaction sequences:

$$NO + O_3 \rightarrow NO_2 + O_2 \tag{1.35}$$

$$NO_2 + O_3 \rightarrow NO_3 + O_2 \tag{1.36}$$

$$NO_3 + h\nu \rightarrow NO + O_2 \tag{1.37}$$

$$net : 2 \times O_3 \rightarrow 3 \times O_2 \tag{1.38}$$

$$ClONO_2 + h\nu \rightarrow Cl + NO_3 \tag{1.39}$$

$$NO_3 + h\nu \rightarrow NO + O_2 \tag{1.40}$$

$$NO + O_3 \rightarrow NO_2 + O_2 \tag{1.41}$$

$$Cl + O_3 \rightarrow ClO + O_2 \tag{1.42}$$

$$ClO + NO_2 \xrightarrow{M} ClONO_2 \tag{1.43}$$

$$net : 2 \times O_3 \rightarrow 3 \times O_2 \tag{1.44}$$
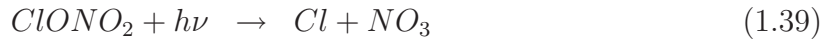
At the same time, NO_x moderates O_x loss through reacting with active hydrogen (HO_x) and halogen species (ClO_x and BrO_x) and converting them to their inactive reservoir forms such as HNO_3 and $ClONO_2$ (*Solomon*, 1999).

$$NO_2 + OH \xrightarrow{M} HNO_3 \tag{1.45}$$

$$NO_2 + ClO \xrightarrow{M} ClONO_2 \tag{1.46}$$

$$NO_2 + BrO \xrightarrow{M} BrONO_2 \tag{1.47}$$
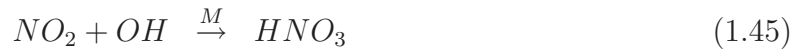
Apart from the catalytic O_x loss cycles, there are null cycles with NO_x, ClO_x (Cl+ClO) and HO_x (HO+HO_2) which cycle through O_x molecules without any net destruction of O_x molecules. For example, the NO_x null cycle, which is in competition with the NO_x catalytic O_x loss cycle, is as follows:

$$NO + O_3 \rightarrow NO_2 + O_2 \tag{1.48}$$

$$NO_2 + h\nu \rightarrow NO + O \tag{1.49}$$

$$O + O_2 \xrightarrow{M} O_3 \tag{1.50}$$

$$net \quad : \quad no\ change \tag{1.51}$$
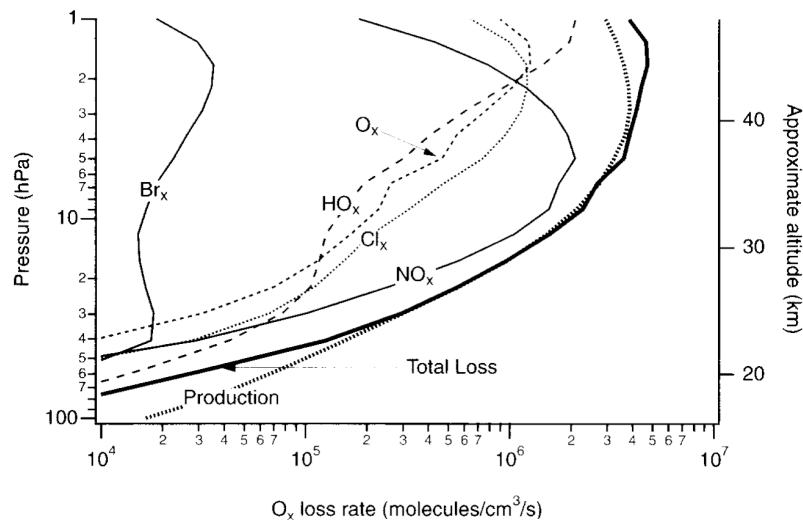
Figure 1.3: Twenty-four hour average O_x production and loss rates for the various gas-phase catalytic cycles. Calculated for 35°N, September conditions (*Dessler*, 2000).

The contributions of various catalytic cycles to the total O_x loss rate is presented in Fig. 1.3 (*Dessler*, 2000). The O_x curve shows the odd-oxygen loss due to direct reaction between O_3 and O (Chapman Reaction 1.7), which is seen to represent only a few percent of the total loss in the lower stratosphere and about 30% of the total loss in the upper stratosphere. Thus to have a sensible estimate of the O_x loss rate, we need to account for catalytic cycles.

1.2.2 Heterogeneous Ozone Chemistry

In Antarctica, large O_3 losses due to Cl_x occur between 12 and 24 km, which is much lower in altitude than was predicted based on gas phase chemistry, which was about 40 km where loss via the Cl_x cycle peaks (*Hofmann et al.*, 1987, 1997). Observations of the vertical profile of PSCs at the same altitude range as O_3 loss ($\sim$10-25 km) at the South Pole confirmed the critical role of PSCs in O_3 depletion through providing surfaces for heterogeneous reactions (*McElroy et al.*, 1986; *Molina and Molina*, 1987; *Collins et al.*, 1993).

PSCs are divided into two general empirical catagories based on their constituents and formation temperature threshhold: Type I and Type II (*Toon et al.*, 1986). Type II PSCs are essentially large water-ice particles and form when the stratospheric temperatures are below 191 K (the ice frost point) where the ice vapour pressure is $\sim 4 \times 10^{-7}$ bar (*Brasseur et al.*, 1999). Type I PSCs are composed predominantly of nitric acid particles. They occur when the stratospheric temperatures fall below 196 K (*Toon et al.*, 1989; *Koop et al.*, 1997). Type I is further divided into Type I(a) and Type I(b). Based on observations, Type I(a) PSCs are predominantly large solid Nitric Acid Trihydrate (NAT) particles (*Voigt et al.*, 2000) and Type I(b) PSCs are supercooled liquid ternary solutions ($H_2O/H_2SO_4/HNO_3$) (*Tabazadeh et al.*, 1994; *Carslaw et al.*, 1994; *Beyerle et al.*, 1997; *Schreiner et al.*, 1999).

As shown in Figure 1.4, meteorological data from the European Centre for Medium Range Weather Forecasts (ECMWF) and from the FU-Berlin stratospheric analyses indicate that the maximum PSC volume during five-year intervals has increased steadily, by about a factor of three, since the late 1960s (*Rex et al.*, 2004).

The following are the most important heterogeneous reactions which take place on the surface of PSCs in polar regions. Although none of these reactions destroy O_3 molecules, they convert inactive chlorine and bromine reservoirs to their chemically active forms (*Solomon*, 1999):

$$HCl + ClONO_2 \overset{\text{PSC}}{\rightarrow} HNO_3 + Cl_2 \tag{1.52}$$

$$N_2O_5 + H_2O \overset{\text{PSC}}{\rightarrow} 2 \times HNO_3 \tag{1.53}$$

$$ClONO_2 + H_2O \overset{\text{PSC}}{\rightarrow} HNO_3 + HOCl \tag{1.54}$$

$$HCl + HOCl \overset{\text{PSC}}{\rightarrow} H_2O + Cl_2 \tag{1.55}$$

$$BrONO_2 + H_2O \overset{\text{PSC}}{\rightarrow} HNO_3 + HOBr \tag{1.56}$$

$$HCl + BrONO_2 \overset{\text{PSC}}{\rightarrow} HNO_3 + BrCl \tag{1.57}$$

$$HCl + HOBr \overset{\text{PSC}}{\rightarrow} H_2O + BrCl \tag{1.58}$$
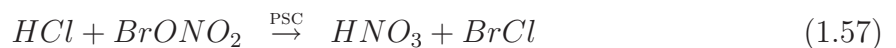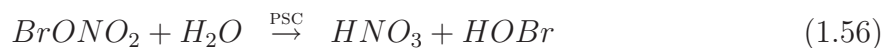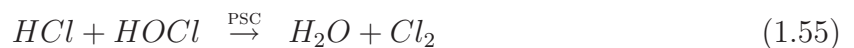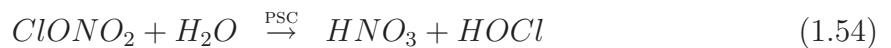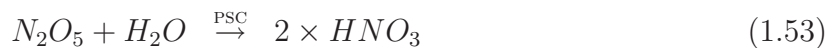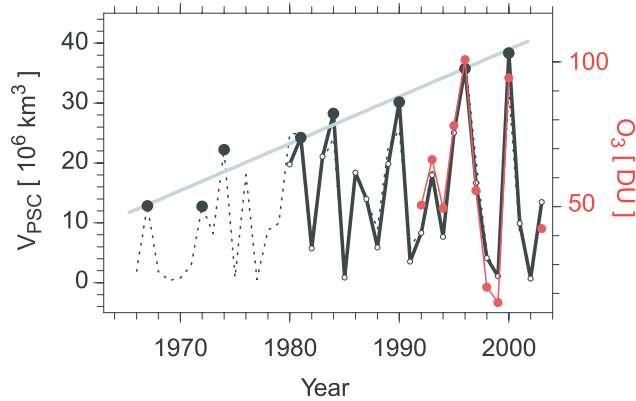
Figure 1.4: Evolution of V_{PSC} over the past 37 years composed from ECMWF data (solid black line) and data from the FU-Berlin (dashed line). The blue line represents a linear fit through the maximum values of V_{PSC} at five-year intervals. Also shown is the estimate of chemical depletion (ΔO_3) for the years 1992 to 2003 (red line), scaled such that V_{PSC} represents the best fit through ΔO_3 (*Rex et al.*, 2004).

As discussed, HNO_3 is the primary constituent of PSCs which provide surfaces for heterogeneous chemistry through which active chlorine (ClO, ClOOCl, OClO) is released from its reservoir species, thereby becoming available to participate in ozone-depleting processes (*Grooß et al.*, 2005; *WMO*, 2003; *Solomon et al.*, 1986). Additionally, the sedimentation of large HNO_3 particles removes the active nitrogen (NO_x) from the stratosphere and makes conditions more favourable for destruction of O_3 by preventing the formation of inactive chlorine reservoirs such as $ClONO_2$ (*WMO*, 2003).

HNO_3 has a winter maximum in polar regions because of the conversion of NO and NO_2 to N_2O_5 and HNO_3 during periods of darkness. Also, HNO_3 abundances increase toward the poles in all seasons, due to the combination of poleward transport and decreasing solar illumination except in regions of PSC formation (*Santee et al.*, 2004). These two processes contribute to the observed seasonal behaviour of HNO_3 at high latitudes (*WMO*, 2003).

Apart from the presence of PSCs in the stratosphere, there are several other prereq-

uisites for polar O_3 loss. High concentrations of active chlorine as the main catalyst of O_3 depletion, combined with low concentrations of NO_2, are needed; otherwise active chlorine goes back to its reservoir $ClONO_2$ through reaction with NO_2. The role of NO_2 is to control the duration and extent of O_3 loss in lower stratosphere (below 25 km) through regulation of active chlorine concentrations (*Solomon*, 1990). Finally, we need solar radiation in spring to photolyze active chlorine and bromine, which subsequently participate in the O_3 catalytic cycles.

1.3   Long-Lived Tracers

There are three long-lived tracers, nitrous oxide (N_2O), methane (CH_4), and hydrogen fluoride (HF), which are widely used to interpret transport processes in the stratosphere. N_2O has a long lifetime of many years in the lower stratosphere. It is produced exclusively in the troposphere and it has a photochemical sink in the middle and upper stratosphere. Measurements have shown that the zonally averaged lower stratospheric N_2O mixing ratios change systematically with season, latitude and altitude, thus local changes from the seasonal zonal mean profiles can be interpreted as the result of stratospheric transport (*Strahan et al.*, 1999).

CH_4 is produced at the surface, and is destroyed at higher altitudes through reaction with OH, O^1D and Cl radicals as well as photolysis in the stratosphere. It has a long lifetime in the lower stratosphere (more than 30 years at an altitude of 20 km) which makes it a suitable tracer of transport processes (*Brasseur and Solomon*, 1984).

HF is considered crucial in monitoring anthropogenically produced changes in the composition of the stratosphere. The main production region for HF is believed to be the stratosphere where the photodissociation of chlorofluorocarbons (CFCs) and hydrochlorofluorocarbons (HCFCs) leads to HF production. Stratospheric HF has a very long lifetime so it accumulates and finally it is removed by downward transport and rainout

in the troposphere. Having a long stratospheric lifetime makes HF an excellent tracer of meridional transport as well as subsidence in the lower stratosphere (*Rinsland et al.*, 2002, 2005).

1.4   Basic Concepts in Stratospheric Dynamics

The concentration of an atmospheric constituent at any point in space is not only a function of chemical production and chemical loss but also a function of transport of the constituent at that point. The continuity equation states that the rate of change of concentration of constituent X is:

$$\frac{\partial [X]}{\partial t} = P_X - L_X [X] - \nabla . (V [X]) \tag{1.59}$$

where P is the rate of photochemical production, L is the loss rate, which is multiplied by the abundance of X to represent the photochemical loss term, and $\nabla . (V [X])$ represents the divergence of the flux of X that is the net transport of X into or out of the point in space (*Brasseur et al.*, 1999).

   A few key features of atmospheric transport are reviewed here to describe how O_x and other atmospheric constituents involved in O_x chemistry are transported. As discussed at the begining of this chapter, the Earth's atmosphere is divided into several layers based on the thermal structure; these layers also represent different transport regimes. The global-scale circulation contains two major parts: a strong zonal (east-west) circulation that distributes atmospheric constituents in the longitudinal direction and a meridional (latitude-altitude) circulation that transports the atmospheric constituents across isentropes, upwelling in the tropics and downwelling in extratropics (*Dessler et al.*, 1998).

1.4.1   Atmospheric Circulation

Figure 1.5 (*Panel on Climate Change*, 2005; *Fortuin and Kelder*, 1998) shows the dominant transport feature in the atmosphere, which is the Brewer-Dobson circulation. This
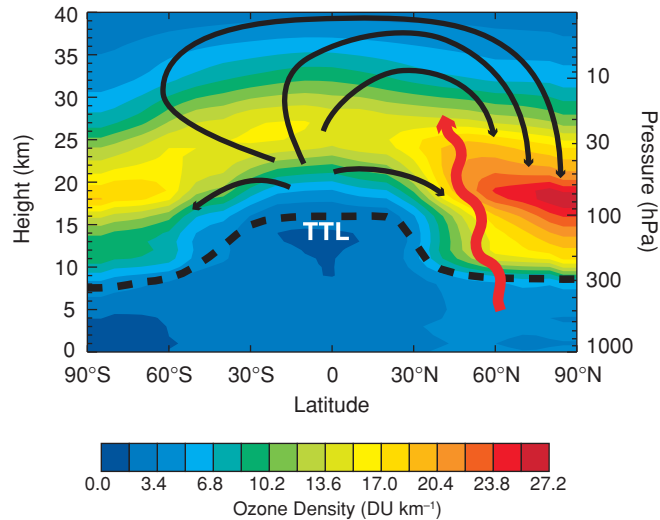
Figure 1.5: Meridional cross-section of the atmosphere showing O_3 density (colour contours, in DU km^{-1}) during NH winter (January to March), from the climatology of *Fortuin and Kelder* (1998). The dashed line denotes the tropopause, and TTL stands for tropical tropopause layer. The black arrows indicate the Brewer-Dobson circulation during NH winter, and the wiggly red arrow represents planetary waves that propagate from the troposphere into the winter stratosphere.

is an upward motion of the air parcels at low latitudes into the stratosphere, then a poleward motion in the stratosphere followed by a slow descent back into the troposphere at high latitudes (*Andrews*, 2000). Dissipation of planetary waves in the stratosphere and above leads to meridional and vertical flow.

If an air parcel is viewed in a rotating reference frame, for example the Earth in this discussion, based on Newton's second law of motion there is an apparent force that deflects the air parcel from a straight path in a direction normal to the direction of the reference frame's rotation. The apparent force is known as the Coriolis force which acts to the right of the direction of motion in the Northern Hemisphere and to the left in the Southern Hemisphere. Therefore an air parcel moving due to the pressure gradient force is deflected until it flows parallel to the isobars where the pressure gradient force

balances the Coriolis force, which is the condition called geostrophic balance (*Holton*, 2004). There is no radiative heating through absorption of solar radiation in the polar regions during the dark months after the autumn equinox; therefore the contrast between low polar temperatures and relatively high mid-latitude temperatures creates a strong pressure gradient in winter. As a consequence of geostrophic balance, the north-south pressure gradient creates a strong zonal wind belt known as the polar night jet that extends vetically from about 100 hPa to the upper stratosphere.

1.4.2 Potential Vorticity

Potential Vorticity (PV) is a dynamically conserved quantity (to a first approximation) that is important to consider when the intention is to isolate the effects of chemistry from dynamics in polar O_3 loss processes. PV is defined as a combination of the absolute vorticity, η, with the three-dimensional gradient of a conservative thermodynamic property, usually potential temperature, θ:

$$PV = \rho^{-1}\eta.\nabla\theta \tag{1.60}$$

where ρ is the density, ∇ is the three-dimensional gradient operator and θ is the potential temperature, the temperature a parcel of dry air at pressure p and temperature T would obtain if it were compressed adiabatically to the reference pressure p_0=1000 hPa. Potential temperature is given by:

$$\theta = T \left(\frac{p_0}{p}\right)^{R/c_p} \tag{1.61}$$

where c_p is the specific heat of air at constant pressure.

PV is a dynamical variable that characterises the flow of an air parcel and is a conserved tracer over short to medium time scales. PV is a function of altitude, latitude and season, with the edge of the polar vortex marked by strong PV gradients.

1.4.3 Wave Motion

There are two types of atmospheric waves of importance to middle atmosphere circulation, both of which depend on the stratosphere's stable stratification. The first are small-scale gravity waves that are generated in a stably stratified atmosphere when air parcels are displaced vertically on isentropic surfaces (surfaces of constant potential temperature) and undergo buoyancy oscillations on time scales of hours to minutes (*Holton*, 2004). If an air parcel is lifted, it cools and becomes more dense than its surroundings, then descends to its original altitude but overshoots to a lower altitude due to its kinetic energy and starts oscillating around its original altitude; this oscillation is known as a gravity wave. There are also gravity waves generated in the troposphere by large-scale topography and meteorology which propagate upward to the stratosphere (*McIntyre*, 1992).

The other important type of atmospheric waves are Rossby waves. Relatively slow large-scale Rossby waves, which displace air parcels along isentropic surfaces on time scales of days (*McIntyre*, 1992), are a direct consequence of the conservation of PV. Consider a closed chain of air parcels initially aligned along a latitude circle where the absolute vorticity, η, is (*Holton*, 2004):

$$\eta = \zeta + f \tag{1.62}$$

where ζ is the relative vorticity, which is due to the rotation of the air parcel itself, $\zeta = \hat{z}.\nabla \times \mathbf{u}$, $\mathbf{u}$ is the air velocity relative to the Earth, $f = 2\Omega\sin\varphi$ is the planetary vorticity, Ω is the Earth's angular velocity, and φ is latitude. If at time t_0 we consider ζ zero then at some later time t_1 we have:

$$(\zeta + f)_{t_1} = f_{t_0} \tag{1.63}$$

$$\text{or}$$

$$\zeta_{t_1} = f_{t_0} - f_{t_1} \approx \beta\delta y \tag{1.64}$$

where $\beta = df/dy$ is the planetary vorticity gradient at the original latitude and δy is the meridional displacement of the air parcel from its original latitude. For the PV to be conserved, Equation 1.62 for a poleward displacement implies a larger value of f, which implies a negative perturbation vorticity (clockwise circulation), while a displacement towards the equator induces a positive perturbation vorticity (counterclockwise circulation) (*Shepherd*, 2003). These vorticity perturbations generate a meridional velocity field which causes the chain of air parcels to oscillate about their equilibrium latitude while the pattern of vorticity maxima and minima propagates towards the west and constitutes a Rossby wave. Large-scale topography or thermal contrasts can generate vertically propagating Rossby waves.

Both gravity waves and Rossby waves dissipate through wave-breaking processes and consequently contribute to the atmospheric mean circulation and change the distribution of atmospheric constituents in the middle atmosphere. In the case of gravity waves, as they move to higher altitudes their amplitude grows due to the density decrease until the local lapse rate exceeds the adiabatic lapse rate. At this point, convection will mix air parcels in the vertical, thus reducing the wave amplitude, a process known as wave breaking (*Visconti and Garcia*, 1987).

For Rossby waves, the wave breaking happens when the wave amplitude becomes large enough to overcome the mean PV gradient.

Stratospheric sudden warming events, which are rapid warmings of the wintertime polar stratosphere caused by polar downwelling, can cause vortex displacement from the pole, change the shape of the vortex, and even cause the break up of the vortex. Stratospheric sudden warming events are observed much more often in the Arctic than in Antarctica, because of the larger orographic features and land-sea temperature differences in the Northern Hemisphere, resulting in a stronger generation of vertically propagating Rossby waves and a warmer Arctic vortex which breaks up earlier in the spring.

1.5 Arctic Ozone

During the past four decades, meteorological observations indicate that the coldest winters became colder in the Arctic, with more isolated polar vortices and increased volume of PSCs, all favouring more chemical ozone depletion (*Christensen et al.*, 2005). Unusually low O_3 columns have been observed during the Arctic winters of 1993, 1995, 1996, and 2000 (*Staehelin et al.*, 2001; *Rex et al.*, 2004) while total column O_3 exhibited increased variability reflecting the variable meteorology of the Northern Hemisphere (*Andersen and Knudsen*, 2002). Both chemical and dynamical processes contribute to low Arctic O_3 columns. Based on our current knowledge, 0-100 DU is the estimate of springtime chemical loss during the past decade, which represents about half of the observed year-to-year variability of total column ozone with typical O_3 column amounts of 300-500 DU for late March in the Arctic (*Rex et al.*, 2004).

1.5.1 Observed Trends in the Canadian Arctic

Canadian measurements of column O_3 in the High Arctic (north of 70ºN) date back to 1957 when Dobson spectrophotometers started measurements at Resolute Bay (74.72ºN, 94.98ºW) and Alert (82.5ºN, 62.3ºW). Dobson spectrophotometers were replaced by automated Brewer spectrophotometers in 1988 at Resolute Bay, and in 1987 at Alert. Both instruments measure the O_3 total column with an accuracy of about 2% (*Fioletov et al.*, 1997). Vertical profile measurements using ozonesondes began at Resolute Bay in 1966, at Alert in 1987 and at Eureka (80.1ºN, 86.4ºW) in 1992. Usually, sondes are launched once per week except in winter at Eureka and Alert when the launch frequency is generally increased to 2-3 per week for Match campaigns (*Fioletov et al.*, 1997). Since 1993, the Canadian High Arctic O_3 data set is composed of measurements at three locations, Resolute Bay, Alert and Eureka.

Extremely low O_3 columns ($\leq$300 DU), about 45% lower than the 1957-1992 average,

were first observed in March 1996 and again in March 1997 in the Canadian High Arctic where the vortex pattern was quite similar to the Antarctic spring vortex with very low stratospheric temperatures (*Fioletov and Evans*, 1997). However, in both years, the annual average column O_3 from Canadian sites in the 50º-60ºN latitude band was only 3.5% lower than the 1957-1992 average. Profile analysis for the same period determined that trends in O_3 concentrations as a function of altitude are most significant in the lower and middle stratosphere, at pressure altitudes of approximately 100 to 25 hPa (*Tarasick et al.*, 2005). Figure 1.6 shows that the strongest decline in total column O_3 over the Northern Hemisphere between 1979 and 2000 occurred in the period from March to May over the subpolar region of the Canadian Arctic, Siberia and Northern Europe with the trend being 4-7% per decade (*Fioletov et al.*, 2002); however the five recent warm winters since 2000 are not included in this trend calculation.

1.5.2   Polar Processes

As discussed in Section 1.3.1, the polar vortex forms in the Arctic every year after fall equinox and isolates the polar regions from mid-latitudes. In the absence of solar heating, the stratospheric temperatures can drop to values low enough for PSC formation and heterogeneous reactions on the surface of PSCs can then take place. During the dark season, chemical O_3 depletion is limited by the lack of solar radiation to photolyze active chlorine (ClO_x) and bromine (BrO_x) species, although during this period O_3 levels can change due to dynamical processes such as sudden stratospheric warming events which mix O_3-rich air masses from mid-latitudes with the Arctic air mass. Once the Sun returns in the spring, the primary reactions which destroy O_3 are those involving ClO_x and BrO_x: Reactions 1.20-1.24, 1.25-1.29 and 1.30-1.34. These three cycles depend on ClO_x concentrations and sunlight, for example the last cycle completely shuts down in the night due to lack of ClO (*Rex*, 2005). Although chemical O_3 loss in the late winter-early spring in the Arctic arises from the same mechanisms that generate the Antarctic ozone hole; we
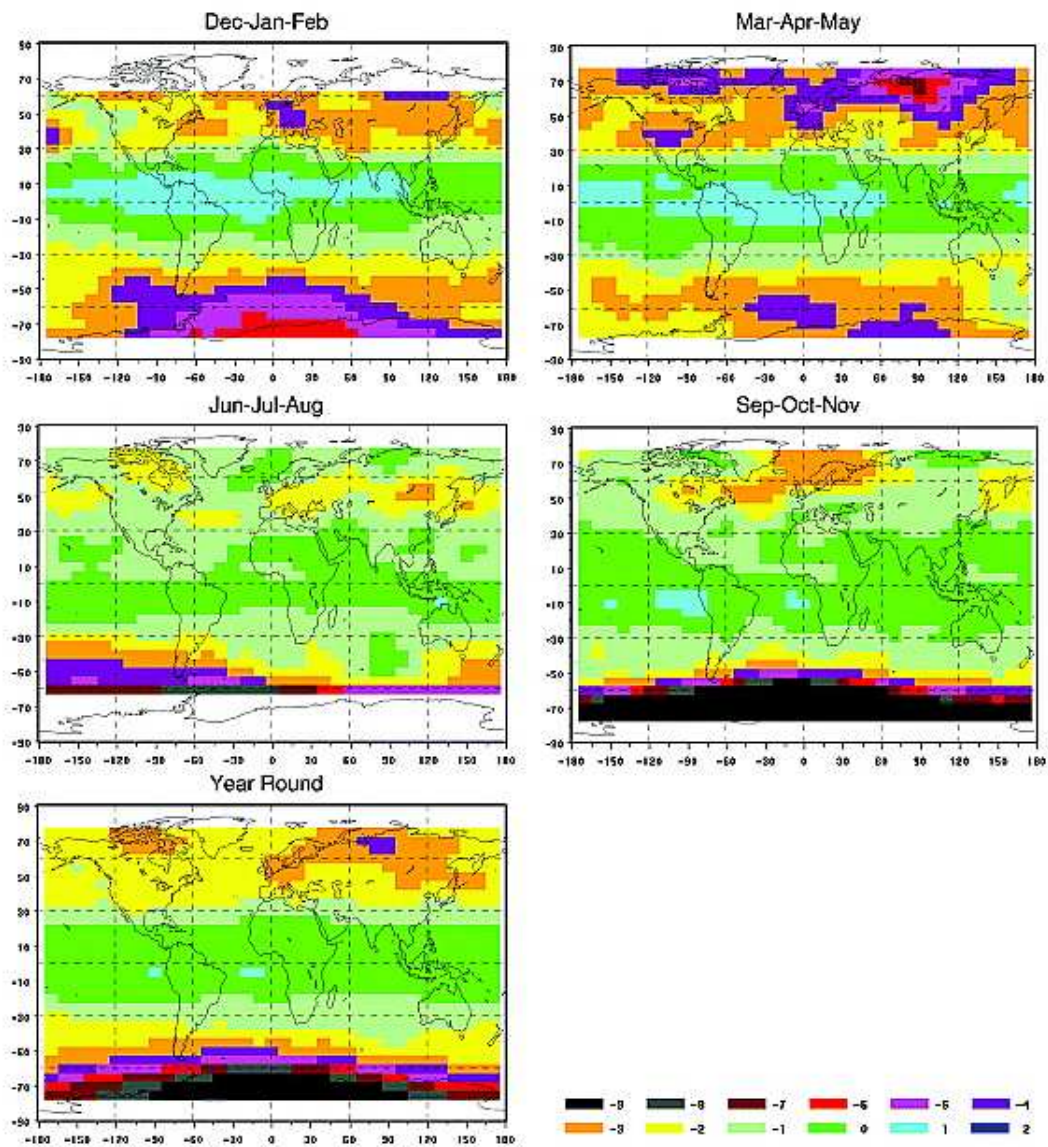
Figure 1.6: Seasonal and year-round total O₃ trends for the period 1979-2000 in percent per decade, estimated using the merged satellite data set which is the combined TOMS and SBUV data (*Fioletov et al.*, 2002).

do not observe extremely low values of O_3 in the Arctic due to the differing meteorological conditions. A stronger Brewer-Dobson circulation in the Northern Hemisphere results in higher Arctic stratospheric temperatures, a smaller probability for PSC formation, more O_3 transport and larger column O_3 compared to Antarctica. Nonetheless, column O_3 in the Arctic decreased while its variability increased in the period 1992-2000 (*Andersen and Knudsen*, 2002). *Rex et al.* (2004) showed that during the past four decades, the coldest winters, where extreme ozone losses occur, have grown colder and the volume of PSCs has increased steadily. However, other studies suggest a slowdown in Arctic O_3 loss and even an increase in O_3 column starting in the 1996-1998 time frame (*Fioletov et al.*, 2002; *Newchurch et al.*, 2003; *Cunnold et al.*, 2004) which are consistent with changes in chlorine loading (*WMO*, 2003). Additionally, a series of cold winters in the 1990s followed by a series of warm winters after 2000 has raised questions regarding the change in the patterns and/or magnitude of inter-annual variability of O_3 in the Arctic stratosphere. These changes would trigger changes in O_3 trends and the stratospheric circulation pattern. Recent studies discuss how the change in dynamical activity combined with increasing GHGs may be an important factor in the timing of ozone recovery (*Austin et al.*, 2003; *Shine et al.*, 2003; *WMO*, 2003). Both early O_3 recovery due to an increase in dynamical activity, and delayed recovery due to lower stratospheric temperatures and decreased dynamical activity have been found in climate model simulations (*Austin et al.*, 2003; *WMO*, 2003).

1.6 Objectives

The primary goal of this thesis was to study the Arctic stratosphere during the crucial period of late winter-early spring, when O_3 depletion occurs. To accomplish this goal, a four-year record of the concentrations of O_3 and of other key trace gases in the Canadian Arctic stratosphere was constructed by combining the University of Toronto ground-

based UV-visible grating spectrometer (UT GBS) and Meteorological Service of Canada Fourier Transform Spectrometer (MSC FTS) observations at AStRO, located at Eureka, NU (80.1ºN, 86.4ºW). The combined UV-visible-IR data set extends the temporal and geographical range of polar stratospheric observations while strengthening Canadian capabilities in monitoring the Arctic atmosphere. This data set also contributes to the provision of a long-term data set of stratospheric constituents in the Canadian High Arctic for future atmospheric trend analysis. In addition, complementary mid-latitude measurements were made and used to assess the quality of the O_3 and NO_2 columns retrieved from the UV-visible spectra.

The second objective was to determine the timing and extent of Arctic ozone loss over Eureka each year and to unravel the coupled chemical and dynamical processes which cause the Arctic stratospheric ozone loss; to achieve this aim a detailed analysis of the UT GBS measurements was performed, in conjunction with meteorological observations. Another important goal of this work was to establish a collaboration with atmospheric modelling groups to help with both improved modelling of the atmosphere and with the interpretation of the measurements. Thus the chemical fields of atmospheric models were evaluated by comparing them with the combined UV-visible-IR data set.

The final goal of this work was to look into the the quality of the NO_2 profiles retrieved from ground-based measurements in the Arctic and to evaluate how closely the retrieved NO_2 profiles represent the true state of the atmosphere in order to perform routine NO_2 vertical profile retrieval on the UT GBS Arctic data set. To achieve this goal, a feasibility study using a radiative transfer (RT) model and climatological NO_2 profiles was undertaken. Also, the impact of NO_2 reference column density (RCD) on the retrieved profile was determined.

1.7 Scope of the Thesis

Given the uncertainties in recent studies and inconsistent results of atmospheric model simulations (*Austin et al.*, 2003), both ongoing measurements of O_3 and related gases and the evaluation of the atmospheric models using observational data sets are important in improving our understanding of future changes. During 1999-2003, the UT GBS was characterized and deployed five times in the Canadian High Arctic, at Environment Canada's Arctic Stratospheric Ozone Observatory (AStrO), located at Eureka, NU (80.1ºN, 86.4ºW) and at Resolute Bay; and twice as part of the Middle Atmosphere Nitrogen TRend Assessment (MANTRA) project in Vanscoy, SK (52ºN, 107ºW). The differential optical absorption spectroscopy (DOAS) method was used to retrieve O_3 and NO_2 columns and is explained in Chapter 2. The instrument and its calibration process are explained in Chapters 3 and 4.

During the MANTRA balloon campaigns in August 2000 and 2002, the UT GBS recorded data as part of the ground-based component from which O_3 and NO_2 columns were retrieved. The NO_2 slant columns are being used by S.M.L. Melo for NO_2 profile retrieval and model comparison. The UT GBS measurements during the MANTRA 2000 and 2002 balloon campaigns are discussed in Chapter 5.

Deploying the UT GBS at AStrO, a four-year springtime Arctic data set was obtained from which O_3, NO_2, and $OClO$ columns were retrieved using WinDOAS software. Comparison between the retrieved data using DOAS and WinDOAS software is presented in the beginning of Chapter 6. Data retrieved during this project, combined with data obtained by other instruments at AStrO, particularly by an infrared Fourier Transform Spectrometer (FTS), were used to determine the day-to-day as well as the inter-annual variability of ozone, NO_x and partial NO_y. Additionally, to have an estimate of chlorine activation, $OClO$ column measurements during the cold spring of 2000 for which the $OClO$ level was enhanced, were made. Vertical profiles of O_3 and temperature, together with total columns of O_3, HF, N_2O, HNO_3, NO_2, NO, CH_4, HCl, and $ClONO_2$, enabled

us to look at the relationship between chemical and dynamical fields, specifically for cases where Eureka was inside and outside the polar vortex. The Arctic measurements are presented in Chapter 6.

The four-year combined Arctic data set was compared with the chemical fields from two atmospheric models: a general circulation model (GCM) and a chemical transport model (CTM) to assess their chemical fields, to address discrepancies between observed and modeled values, and to facilitate improved modeling of the atmosphere. For the first time, Canadian Middle Atmosphere Model (CMAM) chemical fields were compared with ground-based observations in the high Arctic to evaluate the CMAM chemical fields, particularly with regard to their representation of the mean state of the atmosphere and their estimates of inter-annual variability for O_3 and the nitrogen family. SLIMCAT fields were compared to observations to evaluate CTM chemical fields. The comparison between the Arctic measurements and the two models is presented in Chapter 7.

FTS solar and lunar column measurements of HNO_3 during 2001-2002 at AStrO were combined with HNO_3 column measurements at two other Arctic sites, Thule and Kiruna, which allowed the first comparison among these three NDSC Arctic sites. Lunar HNO_3 columns at AStrO and solar HNO_3 columns at Kiruna were compared with CMAM HNO_3 columns, providing insight to the evolution of the HNO_3 field in the period of darkness. The results of this comparison are also presented in Chapter 7.

Using NO_2 measurements made in the UV-visible and applying the inverse method, a sensitivity study of NO_2 reference column density (RCD) in the retrieval of NO_2 vertical profiles was undertaken. In addition, climatological NO_2 vertical profiles were used in combination with a radiative transfer model to evaluate the NO_2 vertical profile retrieval method. Chapter 8 discusses the result of these two studies. The thesis concludes with Chapter 9, which provides a summary of all other chapters as well as recommendations for the future work.

1.8 Scientific Contributions

The UT GBS was assembled by M.R. Bassford and K. Strong in 1998 and was first deployed as one of the ground-based instruments in the MANTRA 1998 balloon campaign, followed by its first Arctic campaign in March 1999 at AStrO by M.R. Bassford. I joined the group in Fall 2000 and deployed the instrument in the Arctic during the winter/spring period of 2000, 2001 and 2003 as well as during the MANTRA 2000 and 2002 balloon campaigns. The instrument was also deployed at Resolute Bay in 2002, but data from that campaign is of poor quality and is not discussed in this work. I used existing DOAS software and performed the analysis of the Arctic data sets for 1999 and 2000 as well as for MANTRA 2000 and 2002. Later, using the more flexible WinDOAS software, I re-analysed the 1999 and 2000 Arctic data sets for O_3, NO_2 and OClO and completed the analysis of the 2001 and 2003 Arctic data sets. I applied K.E. Preston's NO_2 vertical profile retrieval software to the 2000 Arctic data set and used climatological NO_2 profiles to perform a sensitivity study on the effect of the NO_2 reference column on the retrieved profile and to evaluate the NO_2 vertical profile retrieval method. I used C.A. McLinden's radiative transfer model both for air mass factor (AMF) calculations and for NO_2 slant column density calculations from climatological profiles. SLIMCAT columns and vertical profiles for different model runs were provided by M.P. Chipperfield. I used CMAM profiles of different chemical species from two model runs provided by C. McLandress to calculate column amounts. MSC FTS measurements at AStrO and their retrievals for 1999 to 2003 were done by R.L. Mittermeier and H. Fast. Denver University Atmospheric Emission Radiometric Interferometer (DU AERI-X) measurements of HNO_3 at AStrO and their retrievals for 1994 to 1996 were done by P.F. Fogal. J.W. Hannigan and M.T. Coffey provided HNO_3 columns for spring 2002 at Thule. T. Blumenstock and F. Hase provided HNO_3 columns for fall 2001 and spring 2002 at Kiruna. I performed all comparisons between these measurements and the CMAM and SLIMCAT model simulations.

Chapter 2

Measurement Techniques

To determine remotely the concentrations of O_3 and related atmospheric species such as NO_2, OClO, BrO, and NO_3, UV-visible absorption spectroscopy can be used. Solar radiation traveling through the Earth's atmosphere is absorbed and scattered by atmospheric constituents, thus the Sun is the light source for such measurements.

2.1   The Electromagnetic Spectrum

Electromagnetic radiation interacts with molecules during absorption, emission or scattering by changing their electric or magnetic properties, such as the electron distributions or the molecule's magnetic dipole moment. These changes trigger changes in the electric or magnetic field of the electromagnetic radiation. The energy of the electromagnetic radiation determines the type of the molecular process, as shown in Table 2.1 (*Banwell and McCash*, 1994) and in Figure 2.1.

In this work, we use the solar spectrum, which is a continuous electromagnetic emission with a superimposed line structure. In the visible and infrared regions of the solar spectrum, H, Mg, Fe, Ca, Si and singly ionized Ca and Mg in the Sun's photosphere create absorption lines known as Fraunhofer lines (*Goody and Yung*, 1989; *Dessler*, 2000).

The Sun's emission spectrum approximates a blackbody at ~ 6000 K with the maxi-

Spectral Region	Approximate Wavelength	Process
Radio	100 m - 1 cm	reversal of spin of a nucleus or an electron
Microwave	1 m - 100 μm	rotational transitions
Infrared	100 μm - 1 μm	vibrational transitions
Visible-UV	1 μm - 10 nm	electronic transitions
X-ray	10 nm - 100 pm	inner electron transitions
γ-ray	100 pm - 1 pm	re-arrangement of nuclear particles

Table 2.1: Different regions of the electromagnetic spectrum and the associated processes giving rise to them (adapted from *Banwell* and *McCash*, 1994).

mum energy at a wavelength $\sim$0.5 μm, resulting in short-wave radiation in the wavelength range of $\sim$0.2-5 μm, while the Earth's thermal emission spectrum is of a blackbody at $\sim$255 K with the maximum energy at a wavelength $\sim$10 μm, resulting in infrared radiation in the wavelength range of $\sim$5-100 μm. Depending on the spectral region, atmospheric constituents interact with the electromagnetic radiation either through extinction or emission. Once perturbed solar or thermal radiation is recorded on the ground or from space, the Beer-Bouguer-Lambert (BBL) law of radiation can be applied to retrieve column amounts or altitude information for desired atmospheric constituents (*Perrin*, 1948).

2.2 The Radiative Transfer Equation

The transfer of solar radiation in the Earth's atmosphere can be expressed with a single equation called the Radiative Transfer Equation (RTE), which consists of four terms and
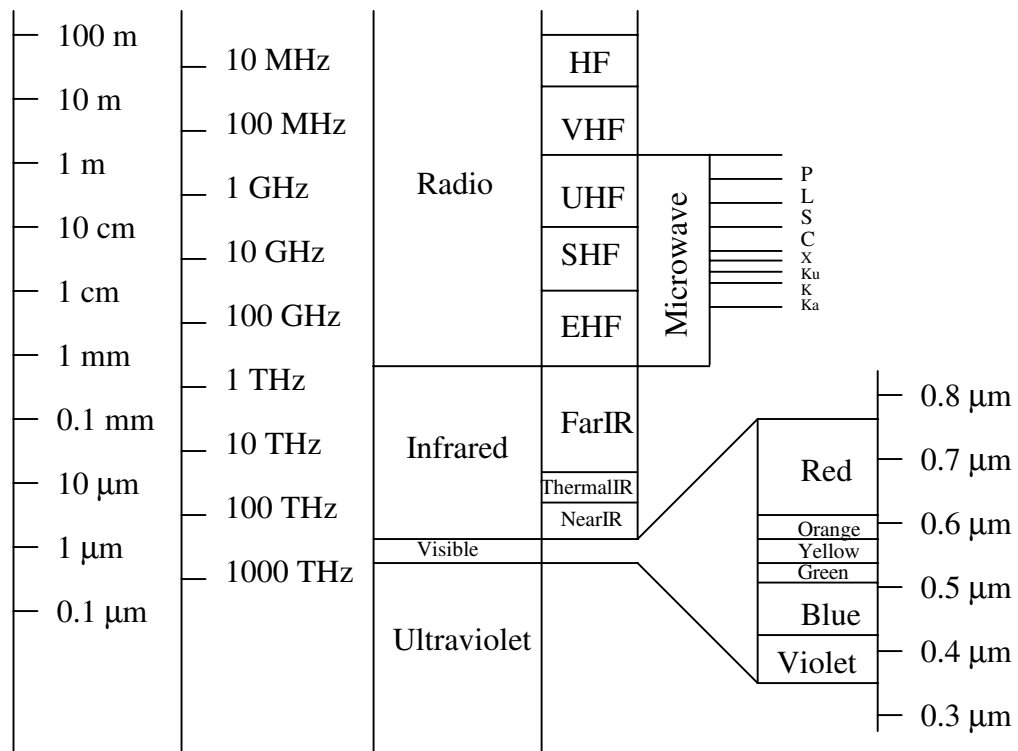
Figure 2.1: The electromagnetic spectrum, showing those regions that are important in remote sensing (adapted from *Rees*, 2001).

can be written as:

$$\frac{dI(\lambda)}{dz} = -\sigma_a(\lambda)I(\lambda) + \sigma_a(\lambda)B_\lambda(T) - \sigma_s(\lambda)I(\lambda) + \frac{\sigma_s(\lambda)}{4\pi}\int_0^{2\pi}\int_0^{\pi}I(\lambda)p(\psi_s)sin\theta'd\theta'd\varphi \quad (2.1)$$

where the first term is the absorption term given by the BBL Law of radiation (*Perrin*, 1948; *Liou*, 1980); the second term is the emission term given by Kirchoff's Law which states that a material is as good an emitter as it is an absorber; the third term is the scattering sink term which follows the form of the BBL Law; and the fourth term is the scattering source term, which is more complex as the radiation is scattered into the beam from all directions. The above equation does not include the inelastic part of scattering (the Ring effect). $I(\lambda)$ is the solar radiance at a particular wavelength, $dI(\lambda)$ is the fractional change of the solar radiance along the beam in a distance dz due to the presence of a radiatively active atmospheric constituent, $\sigma_a(\lambda)$ is the volume absorption/emission coefficient, $\sigma_s(\lambda)$ is the volume scattering coefficient, and the directionally weighted average of $I(\lambda)$, $\langle I'\rangle$, is expressed as:

$$\langle I'\rangle = \frac{1}{4\pi}\int_0^{2\pi}\int_0^{\pi}I(\lambda)p(\psi_s)sin\theta'd\theta'd\varphi' \quad (2.2)$$

where ψ_s is the scattering angle, the angle between the incoming radiation and the original beam and $p(\psi_s)$ is the scattering phase function which specifies the amount of the radiation scattered into the beam.

The full RTE can be simplified in the UV-visible and near IR regions where neither the Earth nor its atmosphere emit significant radiation. The extinction coefficient, $\sigma_e(\lambda)$ is the sum of $\sigma_a(\lambda)$, the absorption coefficient, and $\sigma_s(\lambda)$, the scattering coefficient. Thus the fractional decrease of the solar radiance, $I(\lambda)$, in a distance dz due to the presence of active atmospheric constituent becomes:

$$dI(\lambda) = -\sigma_e(\lambda)I(\lambda)dz \quad (2.3)$$

where $\sigma_e(\lambda)=\sigma_a(\lambda)+\sigma_s(\lambda)$ can be written as $\rho k_e(\lambda)$ where ρ is the density of the absorbing or the scattering material and $k_e(\lambda)$ is the sum of the absorption cross section, $k_a(\lambda)$,

and the scattering cross section, $k_s(\lambda)$. The strength of the absorption is often defined by the absorption cross section $k_a(\lambda, T, p)$ in units of $cm^2 molecule^{-1}$. The absorption cross section can be interpreted as the cross-sectional area of the particle that absorbs all of the radiation incident upon it. The absorption cross section may change with wavelength, temperature and pressure. Assuming that $k_e(\lambda)$ is independent of temperature and pressure (and therefore altitude) (*Houghton*, 2002), we can integrate the above equation over the distance l along the beam between the radiation source and the detector, which results in:

$$I(\lambda) = I_0(\lambda)exp[-(k_a(\lambda) + k_s(\lambda))\rho l] \qquad (2.4)$$

where $I(\lambda)$ is the transmitted spectral radiance, and $I_0(\lambda)$ is the incident spectral radiance. We can define the absorption optical depth (δ_a) and the scattering optical depth (δ_s) as:

$$\delta_a = k_a(\lambda)\rho l \qquad (2.5)$$

$$\delta_s = k_s(\lambda)\rho l \qquad (2.6)$$

To further expand Equation 2.4, we need to discuss the scattering process and assign the scattering coefficient to each process. The physical process called scattering is defined such that a particle in the path of electromagnetic radiation continuously removes energy from the incident radiation and reradiates the energy in all directions. The amount of scattering depends on a particle's size, shape, index of refraction, and also on the number of particles, the thickness of the layer containing the particles, and the wavelength of the incident radiation. There are two types of scattering that need to be discussed in this application: Rayleigh and Mie scattering. Rayleigh scattering occurs when photons are elastically scattered by particles whose dimensions are much less than the wavelength of the radiation (*Andrews*, 2000). In the case of UV-visible radiation, the Rayleigh scattering is due to molecules in the atmosphere.

A more complex scattering is Mie scattering, whereby photons are elastically scattered by particles such as aerosols and cloud droplets. Mie scattering occurs when the

wavelength of the incident radiation is comparable to the circumference of the particle, and the scattering cross section depends on the viewing angle, index of refraction and the size and shape of the particle (*Andrews*, 2000). In Differential Optical Absorption Spectroscopy (DOAS), the scattering terms are considered to be slowly varying with wavelength and it is convenient to subtract them using a polynomial fit (i.e. a high-pass filter) as discussed in Section 2.3.4.

We can now write Equation 2.4 as:

$$I(\lambda) = I_0(\lambda) exp \left[- \left(\sum_i \delta_{a_i}(\lambda) + \delta_s^R(\lambda) + \delta_s^M(\lambda) \right) \right] \tag{2.7}$$

where the absorption optical depth is now summed over all atmospheric constituents, thus $\delta_{a_i}(\lambda)$ is the optical depth of the ith constituent from which the line-of-sight column density of the constituent can be derived when we have knowledge of the absorption cross section, $k_a(\lambda)$. $\delta_s^R(\lambda)$ and $\delta_s^M(\lambda)$ are the optical depths due to Rayleigh and Mie scattering, respectively.

2.3 Ground-Based UV-Visible Spectroscopy

Applying Equation 2.7 to the solar radiation in the UV-visible region enables us to measure the line-of-sight column densities (slant column densities), vertical column densities and vertical profiles of atmospheric constituents that have detectable absorption features in this region.

2.3.1 Fundamentals of UV-Visible Spectroscopy

In the UV-visible region, many absorption processes are a combination of electronic and vibrational transitions. In this region, the absorption of a high-energy photon can lead to the excitation of a molecule from one electronic state to another. As the excited state is unstable, the molecule either decomposes into its constituents through photodissociation
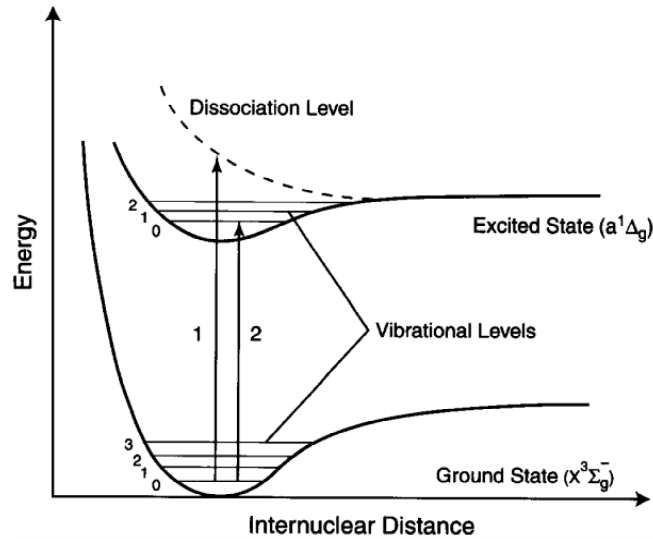
Figure 2.2: Potential energy curves for two electronic states of a diatomic molecule. The horizontal lines in the potential well represent the vibrational energy levels (*Liou*, 1980).

or is photoionized. As most molecules are in the ground vibrational state at atmospheric temperatures, in vibrational transitions usually there are two possibilities once a photon is absorbed. The molecule is excited either into a level known as the dissociation level, or into a specific vibrational level of the upper electronic state, shown in Figure 2.2. The spectrum consists of a smooth continuum at short wavelengths above the dissociation level and of absorption lines at discrete wavelengths (*Liou*, 1980).

Absorption Cross Sections of Atmospheric Constituents

The following is a brief description of the molecules which can be detected using UV-visible zenith-sky absorption spectroscopy.

Ozone molecule

The O_3 molecule absorbs UV-visible radiation between 200 and 790 nm, mostly due to electronic transitions. The UV-visible O_3 absorption bands are shown in Figure 2.3. The Hartley bands from 200-300 nm are the strongest absorption bands, and are due to fast photodissociation of ozone in the upper electronic state, accompanied by a superimposed
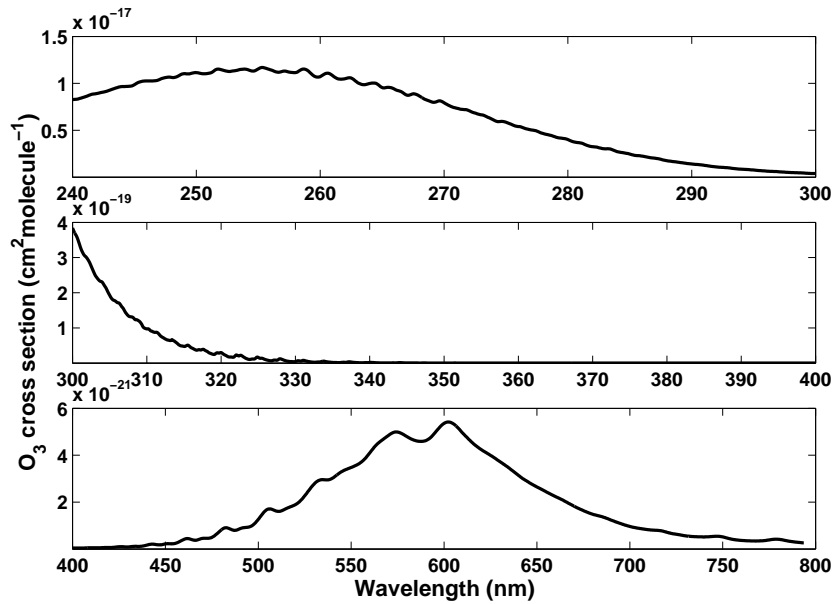
Figure 2.3: The Hartley, Huggins and Chappuis absorption bands of O_3 are shown in the top, middle and bottom panels, respectively, measured at 241 K with the GOME Flight Model spectrometer (*Burrows et al.*, 1999).

vibrational structure. The Huggins bands start around 300 nm and extend to 390 nm. The Hartley and Huggins bands are mostly responsible for limiting UV radiation at the Earth's surface. Huggins bands are strongly temperature dependent. The temperature dependence of these bands is explained by changing rotational and vibrational distributions in the electronic ground state. The Chappuis band is the broad ozone absorption band in the visible, extending from 380 to 800 nm. The Chappuis band is smooth in shape but shows superimposed structures due to interferences between two interacting excited electronic states. This band is slightly temperature dependent and is weak, more than a thousand times weaker than the Hartley bands. Both the Chappuis and Huggins bands are used for atmospheric remote sounding applications. At the long-wavelength tail of the Chappuis band, from 700 to 1100 nm, are the very weak Wulf bands (*Burrows et al.*, 1999a).

NO$_2$ molecule

The absorption of radiation by NO$_2$ also occurs in the UV-visible region. The NO$_2$ absorption spectrum is due to electronic transitions and extends from 300 to 1100 nm as shown in Figure 2.4, however there are rotational and vibrational fine structures superimposed on the absorption spectrum (*Douglas and Huber*, 1965). The NO$_2$ peak absorption cross sections are over an order of magnitude weaker than those of the O$_3$ Chappuis band, so NO$_2$ causes much smaller absorption in the solar spectrum for comparable atmospheric concentrations. The NO$_2$ absorption spectrum also has narrow spectral features which are temperature and pressure dependent. Therefore NO$_2$ cross sections have to be recorded at relatively high spectral resolution and pressures and temperatures representative of the atmosphere. NO$_2$ differential structure increases with decreasing temperature, which is due to changes in the lower state's rotational population with temperature (*Burrows et al.*, 1998).

BrO molecule

The BrO absorption spectrum, shown in Figure 2.4, extends from 300 to 400 nm and has banded structures at longer wavelengths due to vibrational transitions. There is a continuum under the strong structured features of the spectrum of BrO. When the temperatures are lower, the structured features are sharper and the apparent continuum cross section decreases. The overlap of rotational lines from the adjacent vibrational levels are thought to be the cause of the temperature dependence of BrO cross sections (*Wahner et al.*, 1988).

OClO molecule

The OClO absorption spectrum, shown in Figure 2.4, has a strong band system due to electronic transitions with narrow features from 270 to 470 nm. The OClO absorption cross section is temperature dependent because the OClO bands are a complex overlap of rotational lines from several vibrational transitions. It has been observed that OClO bands are sharper at lower temperatures (*Wahner et al.*, 1987).

NO$_3$ molecule

The NO$_3$ molecule absorbs very strongly in the visible region of solar radiation due to electronic transitions. It has two strong wide bands at 623 nm and 662 nm with the main absorption feature is centered at 662 nm (*Renard et al.*, 2001). The 623-nm band usually is not used in retrievals because it is partly overlapped by an oxygen band which has a similar shape, which can thus lead to an overestimation of the NO$_3$ (*Renard et al.*, 1999a). The 650-670 nm spectral band is usually used, particularly the 662-nm band which is the most intense band (*Weaver et al.*, 1996). The NO$_3$ absorption cross section is temperature dependent and the studies of *Yokelson et al.* (1994) and *Sander* (1986) show a 36% increase in absorption with decreasing temperature from 298 K to 200 K.

O$_4$ molecule

Also shown in Figure 2.4 is the oxygen dimer, O$_4$, which mostly absorbs from 330 to 670 nm and is due to electronic transitions by oxygen molecules when they are in a collisional complex. At very low temperatures around 90° K, there is also a bound state van der Waals molecule, O$_4$, with fine structure absorption bands due to combinations of electronic and vibrational transitions (*Greenblatt et al.*, 1990).

H$_2$O molecule

The H$_2$O molecule absorbs in a wide spectral interval from the near UV to the infrared. As shown in Figure 2.4, in the UV-visible region, H$_2$O has an absorption spectrum due to electronic transitions that is weak compared to the intense absorption spectrum in infrared region (*Rothman et al.*, 1998).

Based on the absorption features of the O$_3$, NO$_2$, BrO, OClO, and NO$_3$ the wavelength region from 340 to 700 nm is ideal for their retrieval from solar spectra.

2.3.2 The Ring Effect

In 1962, Grainger and Ring observed that Fraunhofer lines in the scattered daylight spectrum are not as deep as in the direct lunar spectrum, a phenomenon known as the
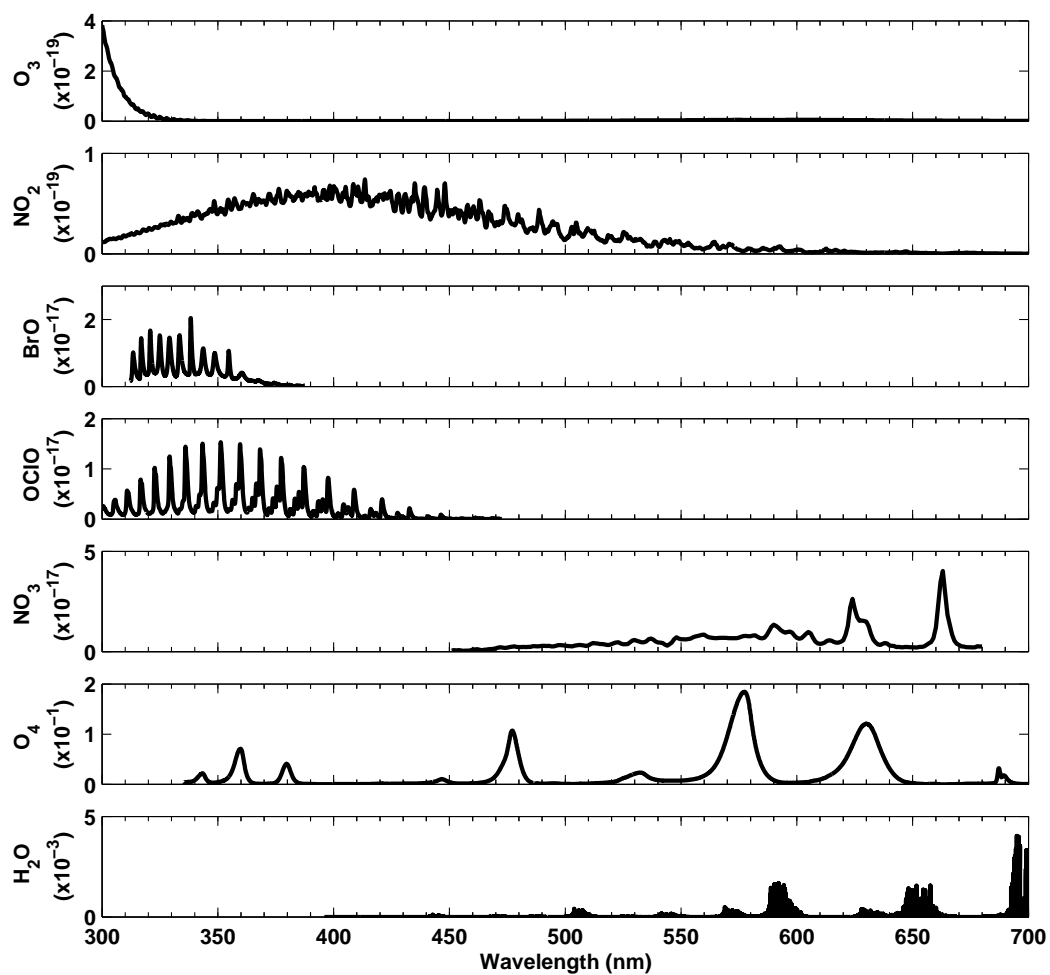
Figure 2.4: The absorption cross sections of O_3, NO_2, BrO, OClO, NO_3, O_4, and H_2O from 300 to 700 nm in cm^2 $molecule^{-1}$. Sources are mentioned in the text.

Ring effect (*Grainger and Ring*, 1962). Once we choose to measure scattered light from the zenith-sky, we have to deal with the Ring effect which is believed to be mostly due to rotational Raman scattering (*Chance and Spurr*, 1997; *Sioris et al.*, 2002).

It is important to account for the Ring effect in zenith-sky spectroscopy because through twilight the magnitude of the Ring effect varies. Thus in ratioing a high Sun spectrum to a twilight spectrum to eliminate the extraterrestrial features (see below), the Ring effect creates residual features that are comparable to the magnitude of absorptions due to NO_2 and BrO in the same region of the spectrum and interfere with the detection of these molecules (*Fish and Jones*, 1995).

2.3.3   Observational Geometry

A number of viewing platforms are used to detect the interaction of electromagnetic radiation with the Earth's atmosphere such as ground, balloons, aircraft and satellites. Ground-based instruments are used for long-term observations and detection of atmospheric trends. Compared to satellite, aircraft and balloon platforms, ground-based instruments are affordable, relatively easy to implement, and advantageous for their reliable continuous measurements. Ground-based observations are also used to validate satellite observations and to test atmospheric models. However the spatial resolution of these measurements is limited to one location on the surface of the Earth, and the vertical resolution is also limited.

Two widely used viewing geometries for ground-based UV-visible absorption spectroscopy are direct solar/stellar viewing and scattered light in zenith viewing/off-axis viewing. In the direct absorption, light emitted by the Sun, the Moon, a planet or a star traverses a direct path to the instrument as it passes through the Earth's atmosphere. However in zenith-sky viewing, the radiation is scattered by atmospheric molecules, and traverses a number of paths before reaching the instrument, which is pointed directly towards the zenith or with an angle relative to the zenith. Zenith-sky observations are
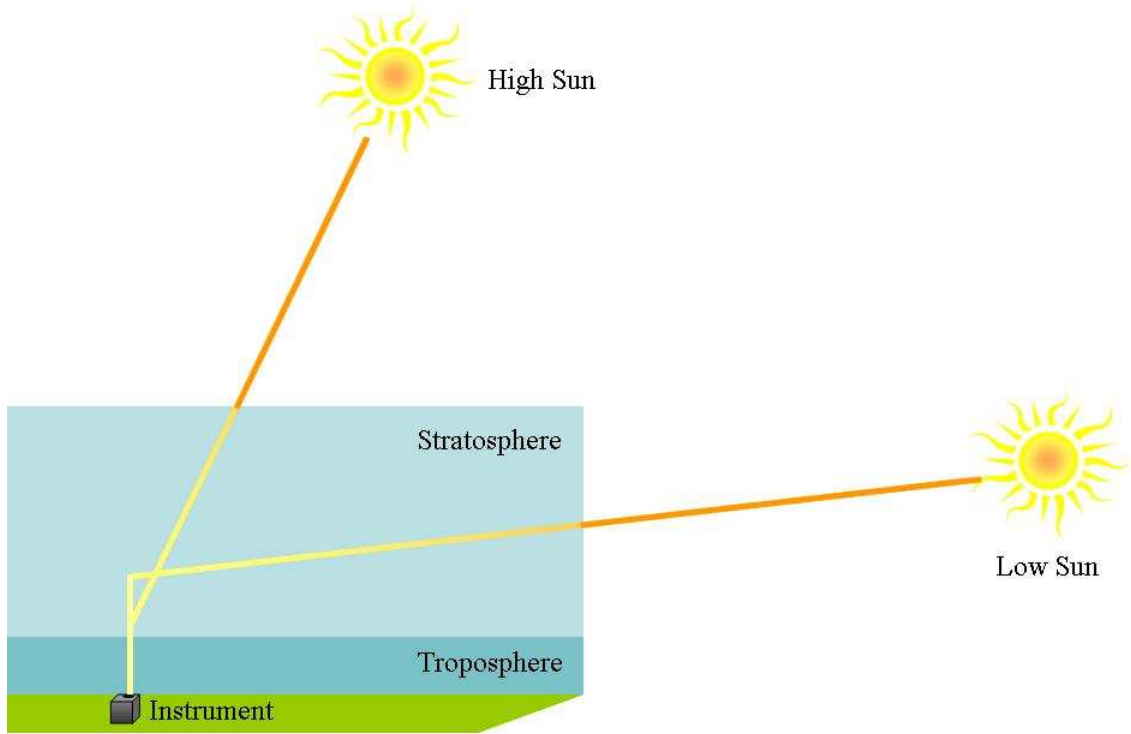
Figure 2.5: Zenith-sky viewing geometry for a ground-based instrument, showing a high Sun observation and a twilight observation with enhanced path in the stratosphere. Only one representative ray is shown here but note that scattering occures from a range of altitudes.

more sensitive to the stratosphere due to the stratospheric light path enhancement during twilight and they are less sensitive to the troposphere as shown in Figure 2.5.

2.3.4 Differential Optical Absorption Spectroscopy (DOAS)

The DOAS technique uses the BBL Law to derive the column density of an atmospheric constituent. We need to solve Equation 2.7 to derive the slant column density of the atmospheric constituent of interest. The amount of absorber along the path, or the slant

column density (u_i) (molec/cm^2), is written as:

$$u_i = l\rho_i. \tag{2.8}$$

Here, l is the the distance along the beam between the radiation source and the detector and ρ_i is the density of the ith atmospheric constituent.

Prior to solving Equation 2.7, $I_0(\lambda)$, the intensity of the radiation at the source, or in our case, the incident solar radiance at the top of the atmosphere should be determined. Not only is the determination of $I_0(\lambda)$ challenging, but also the overlap of the absorption features of different atmospheric constituents presents more challenges (*Platt*, 1994; *Noxon*, 1975).

Using DOAS, we solve the problem by taking the ratio of two spectra first as:

$$-ln\left(\frac{I_1(\lambda)}{I_2(\lambda)}\right) = \sum_i k_i(\lambda)(u_{i,1} - u_{i,2}) + \Delta\delta_s^R(\lambda) + \Delta\delta_s^M(\lambda) \tag{2.9}$$

where $I_1(\lambda)$ and $I_2(\lambda)$ are the high Sun and twilight spectra, $u_{i,1}$ and $u_{i,2}$ are the slant column densities of constituent i along the two paths, $\Delta\delta_s^R(\lambda)$ is the differential optical depth (DOD) of Rayleigh scattering, and $\Delta\delta_s^M(\lambda)$ is the differential optical depth of Mie scattering. Also the absorption cross section of any molecule can be separated into two terms as shown:

$$k_i(\lambda) = k_{i0}(\lambda) + k_i'(\lambda) \tag{2.10}$$

where $k_{i0}(\lambda)$ is the slowly varying part of the absorption cross section and defines the underlying slope of the spectrum, while $k_i'(\lambda)$, called the differential cross section, varies rapidly with λ. The extinction due to Rayleigh and Mie scattering is considered to be slowly varying with wavelength, so by substituting for $k_i(\lambda)$ in Equation 2.9 and rearranging the equation, grouping by the slowly and rapidly varying parts of the absorption

cross section, we have:

$$-ln\left(\frac{I_1(\lambda)}{I_2(\lambda)}\right) = \left[\sum_i k_i'(\lambda)(u_{i,1} - u_{i,2})\right]$$
$$+ \left[\sum_i k_{i0}(\lambda)(u_{i,1} - u_{i,2}) + \Delta\delta_s^R(\lambda) + \Delta\delta_s^M(\lambda)\right] \quad (2.11)$$

The first function contains only terms that rapidly vary with wavelength which show the differential absorption features of atmospheric constituents, while the second function has slowly varying absorption features together with the Rayleigh and Mie scattering terms.

It is convenient to derive the slowly varying term by fitting a polynomial to the LHS of Equation 2.11 and subtracting it. Removing the slowly varying terms leaves us with the differential optical depth and cross sections:

$$DOD = -ln\left(\frac{I_1(\lambda)}{I_2(\lambda)}\right)' = \left[\sum_i k_i'(\lambda)(u_{i,1} - u_{i,2})\right] \quad (2.12)$$

where now the LHS denotes the negative logarithm of the measured spectral radiances after the polynomial has been subtracted. In a typical DOAS measurement, as shown in Figure 2.6, the two spectra are taken at twilight and at high Sun to maximize the stratospheric path of the desired atmospheric constituent because the high Sun spectrum travels a short path in the stratosphere while the twilight spectrum travels a long path in the stratosphere. Thus, given laboratory measurements of the absorption cross sections, the differential slant column densities (DSCDs) of atmospheric constituents can be found by performing a simultaneous least squares fit to Equation 2.12. The DSCD for the ith constiuent can be written as:

$$DSCD_i = \Delta u_i = u_{i,1} - u_{i,2} = u_{i,twilight} - u_{i,reference}. \quad (2.13)$$

2.4 Vertical Column Retrieval

Vertical column densities of stratospheric constituents are calculated using the DSCDs and an appropriate enhancement factor for each absorber, referred to as the air mass
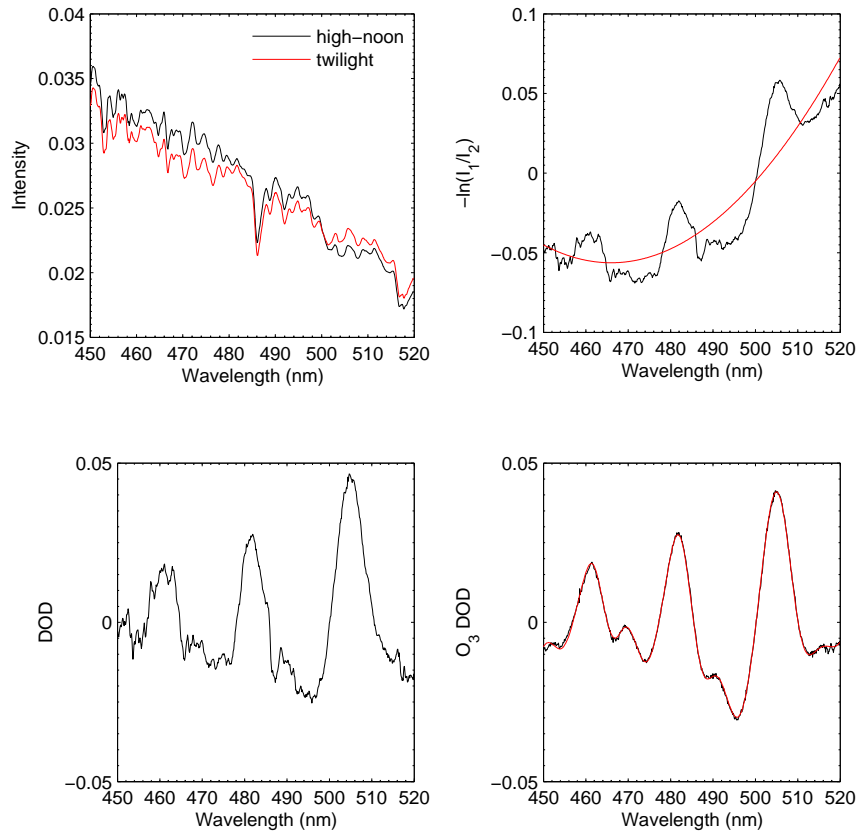
Figure 2.6: Practical example of differential optical absorption spectroscopy, looking at the O_3 absorption region. The top left panel shows the 90^0 SZA sunset (in red) and noon reference spectra (in black) and the top right panel is the difference in optical depth between the sunset and the noon spectra (in black) together with the second order polynomial fit to the difference in optical depth (in red). The bottom left panel shows the observed optical depths of all absorbers in the wavelength region used to retrieve O_3 abundances. The bottom right panel is the amount of O_3 that was fitted to the observed optical depth. The measured optical depth is black and the fit is red.

factor (AMF). The AMF is defined as the ratio of the number of molecules in the slant path to the number of molecules in the vertical path and in this work is determined using a radiative transfer (RT) model developed by *McLinden et al.* (2002) (also see Chapter 8). Following Equation 2.13, we can include the AMF definition and write the DSCD as:

$$DSCD(\theta) = AMF(\theta) \times VCD(\theta) - RCD \tag{2.14}$$

where reference column density (RCD) is the amount of absorber in the high Sun reference spectrum and VCD(θ) denotes the vertical column density at solar zenith angle (SZA), θ. The above equation has the linear form of y=mx+c, for absorbers with no or small diurnal variation, where y represents the DSCD, x represents the AMF, the y-intercept, c, is equal to the negative RCD value (in practice it may also contain instrumental artifacts) and the slope, m is equal to the VCD. Therefore by fitting the observed differential slant columns derived from a set of twilight spectra against the corresponding AMFs, the Langley plot, we can determine the VCD of the absorber as the slope of the line. For atmospheric constituents with strong diurnal variation such as NO_2 or BrO, the VCD at twilight, for SZA 90º, is usually calculated instead, using the following form of Equation 2.14:

$$VCD(\theta) = \frac{DSCD(\theta) + RCD}{AMF(\theta)} \tag{2.15}$$

2.4.1 Air Mass Factor

As discussed above, the retrieval of accurate vertical column amounts of stratospheric constituents from zenith-sky spectroscopy is dependent on accurately modeling the transfer of radiation through the atmosphere and calculating suitable air mass factors.

The air mass factor for a specific absorber is the ratio of the slant path optical depth, δ_{slant}, to the vertical optical depth, δ_{vertical}, of the absorber and can be written as:

$$AMF = \frac{\delta_{slant}}{\delta_{vertical}} = \frac{SCD}{VCD}. \tag{2.16}$$

Using the BBL Law and denoting the light intensity at the instrument with the absorber being present as $I(\lambda)$, and in the absence of the absorber as $I'(\lambda)$, the air mass factor can be expressed as (*Höiskar et al.*, 1997):

$$AMF = \frac{ln\left(\frac{I(\lambda)}{I'(\lambda)}\right)}{kVCD} \tag{2.17}$$

where k is the absorption cross section of the absorber and all scattering orders are considered. In this work, the AMFs for O_3 and NO_2 are calculated using a one-dimensional vector radiative-transfer model which is described in Chapter 8.

2.5 Vertical Profile Retrieval

The NO_2 DSCDs determined from zenith-scattered solar spectra at twilight contain information about the vertical distribution of NO_2 in the stratosphere. Generally as the SZA increases during twilight, the mean altitude at which Rayleigh scattering occures gradually increases, as do the SCDs of atmospheric constituents. However, the increase in SCD is even more pronounced for those diurnally variant absorbers such as NO_2, whose concentration increases with SZA due to photochemistry. Thus using an inversion method, the vertical distribution of the absorber can be derived using the variation of the SCDs with SZA.

After the pioneering works of *Brewer et al.* (1973) and *Noxon* (1975), other attempts at the retrieval of vertical distributions of atmospheric trace gases from ground-based zenith-sky observations have been reported (*McKenzie et al.*, 1991; *Preston et al.*, 1997; *Schofield et al.*, 2004). In this work, the vertical profile of NO_2 is derived using the Optimal Estimation Method (OEM) (*Rodgers*, 1976, 1990, 2000) implemented by *Preston* (1995).

Following Rodgers' method we have:

$$\mathbf{y} = F(\mathbf{x}, \mathbf{b}) + \epsilon_{\mathbf{y}} \tag{2.18}$$

where F is a forward model relating a series of NO_2 DSCDs, $\mathbf{y}$, as a function of SZA to the vertical profile of NO_x at a given SZA. $\mathbf{x}$ is the state vector, $\mathbf{b}$ is the vector of forward model parameters and $\epsilon_{\mathbf{y}}$ is the measurement error.

We can solve the problem by inverting Equation 2.18; however the inversion method does not result in a unique solution. In the real atmosphere, $\mathbf{x}$ is a continuous function of height while $\mathbf{y}$, the measurement vector, represents a finite number of NO_2 DSCD measurements. Therefore the problem is said to be underconstrained, or in other words the same measurement, $\mathbf{y}$, can result from different atmospheric profiles $\mathbf{x}$. Here we choose the OEM in which the optimum solution is selected from several possible solutions using an *a-priori* constraint to reject those solutions that might be consistent with the measurements but are not real. The inversion problem for the ground-based UV-visible observations is discussed in detail by *Preston et al.* (1997). The retrieved profile $\hat{\mathbf{x}}$ is given as:

$$\hat{\mathbf{x}} = \mathbf{x_a} + \mathbf{S_a}\mathbf{K}^{\mathrm{T}} \left(\mathbf{K}\mathbf{S_a}\mathbf{K}^{\mathrm{T}} + \mathbf{S}_\epsilon\right)^{-1} (\mathbf{y} - \mathbf{K}\mathbf{x_a}) \tag{2.19}$$

where $\mathbf{x}_a$ is the *a-priori* profile, usually derived from the measurements or a climatological mean profile, $\mathbf{S}_a$ is the *a-priori* uncertainty covariance matrix, $\mathbf{S}_\epsilon$ is the measurement uncertainty covariance matrix, and $\mathbf{K}^{\mathrm{T}}$ is the transpose of $\mathbf{K}$. $\mathbf{K}$ is the weighting function matrix also known as the Jacobian and its rows indicate the degree of sensitivity of the DSCD at each SZA to a change in the vertical profile and is defined as:

$$\mathbf{K} = \frac{\partial \mathbf{y}}{\partial \mathbf{x}}. \tag{2.20}$$

The weighting functions are calculated by consecutively perturbing each layer of the *a-priori* profile and recalculating $\mathbf{y}$ using the forward model.

Chapter 3

Instrumentation

In this chapter, the criteria for the instrument selection, the instrument's components, their specifications and the automated operation of the instrument are discussed.

3.1 Instrument Requirements

For this work, a UV-visible instrument was chosen to perform simultaneous measurements of O_3 and other atmospheric constituents which play a role in O_3 chemistry in the Arctic stratosphere, namely NO_2 and to a limited extent OClO and BrO which have absorption features in the UV-visible region of the atmospheric spectra. The instrument was designed to be robust, portable and fully automated since it was to be deployed under Arctic winter/spring conditions as well as mid-latitude summer conditions. Several considerations were taken into account to obtain the optimum wavelength region, resolution, sampling and signal-to-noise ratio of the detector.

3.1.1 Wavelength Region

The primary goal for the instrument is to measure O_3 and NO_2. The instrument has sufficient resolution and sensitivity in the UV region to measure OClO and BrO, and its

spectral coverage is wide enough to measure NO_3 without compromising O_3 and NO_2 measurements.

O_3 is generally measured using either the Huggins bands at 300-380 nm, or the Chappuis band at 380-800 nm. In this work, we are using the Chappuis band for O_3 retrieval. NO_2 and OClO are derived from their absorption bands at 340-450 nm and 310-440 nm, respectively. BrO absorption features appear around 300 nm and taper off about 390 nm.

To obtain NO_3 nighttime measurements, stellar/lunar absorption spectra can be recorded, while twilight NO_3 measurements are done using zenith-scattered sunlight spectra. The NO_3 absorption feature centred at 662 nm is commonly used to derive twilight NO_3 abundances. Considering the above information, a spectral bandwidth from 340 to 700 nm is optimum to allow the simultaneous retrieval retrieval of all five species.

3.1.2 Resolution, Sampling and Signal-to-Noise Ratio

The absorption features of our target atmospheric constituents differ in their shape. NO_2, OClO and BrO have absorption features with relatively narrow spectral features, so to avoid smoothing out these features, a spectral resolution of, or better, than 1 nm is needed. O_3 and NO_3, with their broader absorption features, can be measured at lower resolution that enables us to operate at higher sampling ratio and over a wider spectral band. To enable measurements at different resolutions, an instrument with an adjustable entrance slit is sought.

Another factor in the instrument selection process is to maintain a high sampling ratio of 6.5 pixels/FWHM or better to avoid undersampling (*Roscoe et al.*, 1996). In order to sufficiently distinguish a spectral feature from noise, a signal-to-noise ratio (SNR) of 1000:1, which corresponds to typical differential optical depths of 10^{-3}, is sought.

3.2   Instrument Description

The instrument selected for this work consists of three main components: input optics to collect the zenith-scattered sunlight and focus it onto the entrance slit of the spectrometer, a spectrometer to disperse the sunlight, and a Charge-Coupled Device (CCD) array detector. Apart from these primary components, there are necessary cables and controllers, a heating system, a cooling system and a weatherproof aluminum box.

3.2.1   Input Optics

Three different configurations for the input optics can be used with our system. These are briefly described below.

The simplest arrangement consists of a mirror with enhanced UV reflectivity (0.1 m by 0.1 m, aluminum coated, Melles Griot Inc., Irvine, CA, USA) angled at 45º, and a f/4 aperture. The mirror folds the scattered sunlight from the zenith into the horizontal plane. Then by use of apertures, the light is directed onto the entrance slit of the spectrometer. In order to reduce the effect of stray light, a six-position filter wheel is used. This is a workable setup but it is not the optimum configuration. It provides a large sky field-of-view (FOV) which results in spatial smearing of the incoming beam. It also preserves the polarization of sunlight, which is a disadvantage. The spectrometer's gratings are sensitive to the degree of polarization of the incoming light, thus it is important to have depolarized light at the entrance slit.

The second configuration includes the same mirror. It again folds the incoming light through 45º, which is then focused onto the entrance slit of the spectrometer by means of a fused silica lens (f=22.4 mm, f/4, Melles Griot). A six-position filter wheel is placed between the lens and the entrance slit of the spectrometer. The most frequently used filter is filter # BG-38 (Andover Corp., Salem, NH, USA) which covers 350-600 nm and effectively cuts out any light outside this wavelength range. The entrance optics are also
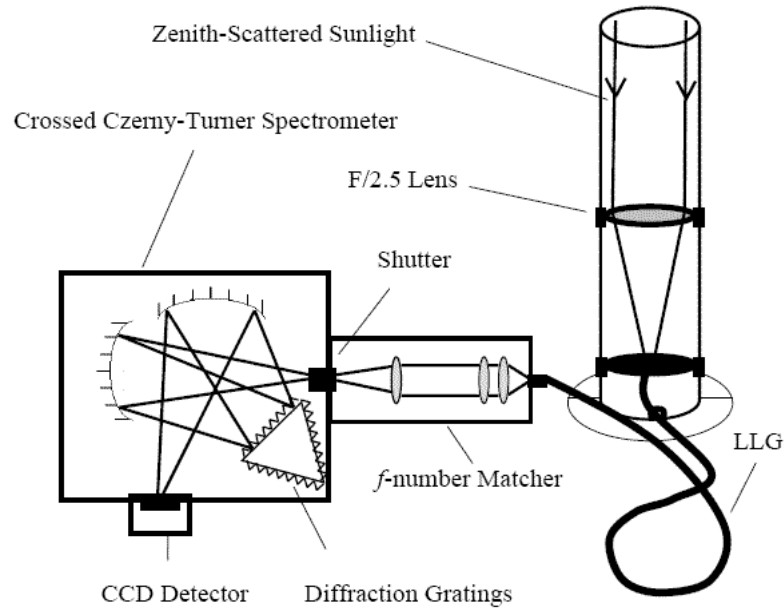
Figure 3.1: Basic elements and ray diagram of the University of Toronto ground-based UV-visible zenith-sky spectrometer.

well baffled to reduce the amount of stray light that enters the system. This configuration is also relatively simple, and provides a focused beam of light at the entrance slit of the spectrometer as well as a smaller sky FOV. However, it has the disadvantage of again preserving polarization.

In order to depolarize the incoming light prior to dispersion inside the spectrometer, another configuration is used. The input optics are modified to include a liquid light guide (LLG) (inner core f=3 mm, length=1 m, Oriel Instruments, Stratford, CT, USA). In the revised optical configuration, zenith-scattered light is collected and focused by a fused silica lens (f=40 mm, f/2.5) onto the liquid light guide. The outgoing light beam is then re-focused onto the entrance slit of the spectrometer by a three-lens f/# matcher. This method is slightly more complex and has the disadvantage of losing a portion of the incoming light beam due to use of the LLG and lenses. Figure 3.1 shows a schematic of the latter configuration that has been used throughout six field campaigns.
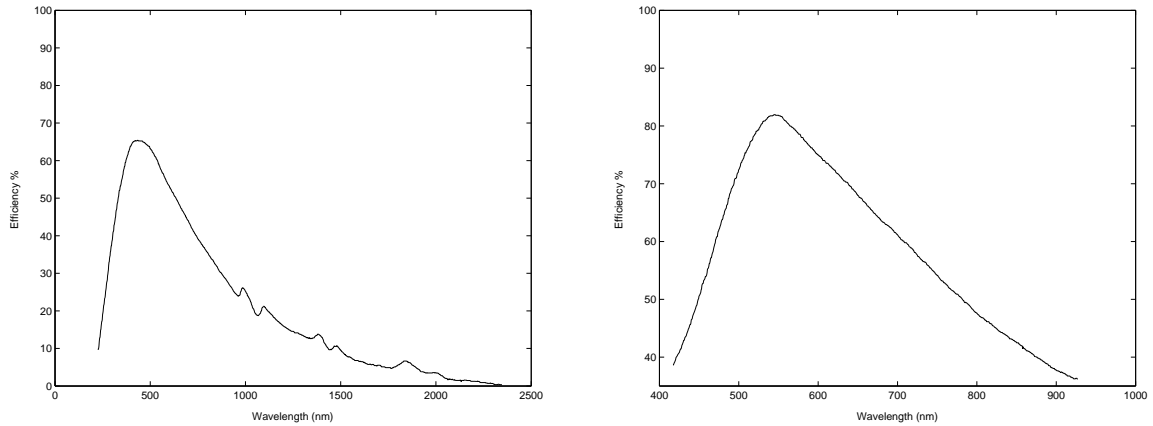
(a) 400 grooves/mm, blaze angle 4º30′, blaze wavelength 400 nm.

(b) 600 grooves/mm, blaze angle 8º38′, blaze wavelength 500 nm.

Figure 3.2: Diffraction grating efficiency for depolarized light of (a) 400 grooves/mm and (b) 600 grooves/mm gratings (adapted from ISA documents).

3.2.2   The Grating Spectrometer

A triple-grating imaging spectrometer (Triax 180, Instruments S. A. Inc., Edison NJ, USA) is the heart of the system. It is a crossed Czerny-Turner design with aspherical optics in order to correct astigmatism, generate a flat field output, and provide point-to-point imaging. It has a focal length of 0.190 m (f/3.9), and a 12 mm by 30 mm focal plane. It is fitted with an adjustable entrance slit (motorized) and a triple-grating turret. This setup ensures flexibility in resolution and spectral bandwidth. There are three plane holographic diffraction gratings mounted on the turret, of 400, 600 and 1800 grooves/mm at blaze wavelengths of 400, 500 and 500 nm, respectively. The 1800 grooves/mm grating was damaged and replaced in 2002 with another 1800 grooves/mm grating at blaze wavelength of 400 nm. The quantum efficiencies of all four gratings are shown in Figures 3.2 and 3.3. The resolution at the centre of the focal plane and the bandwidth of each of the diffraction gratings are shown in Table 3.1.
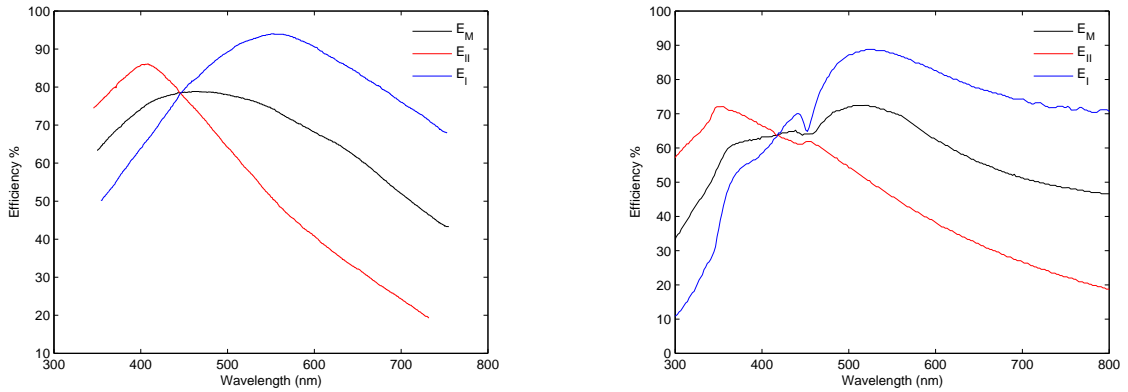
(a) 1800 grooves/mm, blaze angle $26^{\circ}45'$, blaze wavelength 500 nm.

(b) 1800 grooves/mm, blaze angle $21^{\circ}6'$, blaze wavelength 400 nm.

Figure 3.3: Diffraction grating efficiency, 1800 grooves/mm grating, (a) from 1998 to 2002 (b) 2002 to present. E_M is for totally depolarized light while $E_\perp$ shows the S plane, polarized perpendicular to grooves and $E_{||}$ shows the P plane, polarized parallel to grooves (adapted from ISA documents).

Grating (grooves/mm)	Approximate Spectral Bandwidth (nm)	FWHM (nm)
400	360	0.96 - 1.28 (1999-2003)
600	234	0.78 - 0.96 (2000-2003)
1800	66	0.20 - 0.49 (1999-2003)

Table 3.1: Typical measured values of the spectral resolution in the middle of the CCD and the bandwidth of the UT GBS for 100 μm slit width.
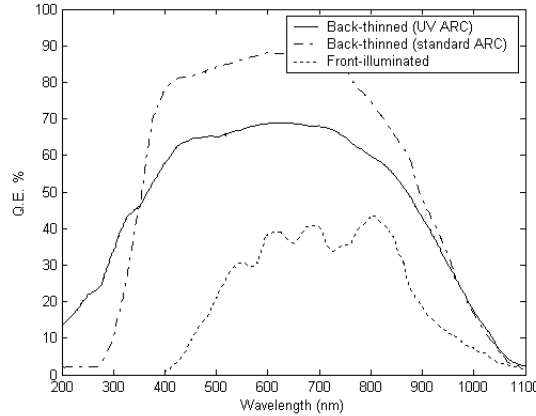
Figure 3.4: Typical quantum efficiencies for SITe CCDs (ISA, Selection and Specifications of SITe chips), including back-thinned with UV enhanced Anti Reflection Coating (ARC), back-thinned with standard ARC and front-illuminated. In this work, a back-thinned CCD with UV enhanced ARC is used (adapted from ISA documents).

3.2.3 CCD Detector

A CCD silicon photodetector array (Instruments S. A. Spectrum One with SITe chip) of 2000×800 pixels is used as the detector. The size of each pixel is 15 μm×15 μm. The active area of the CCD detector, the focal plane, is 30 mm wide by 12 mm high. A thermoelectric cooling device is designed to hold the CCD at -30° C and on-chip binning of each pixel column can be carried out to maximize the SNR. The CCD is back-illuminated in order to improve the quantum efficiency of the detector in the UV region, as shown in Figure 3.4. The CCD has an antireflection coating optimized for the UV and visible.

3.2.4 Additional Components

There are four additional components to the instrument, a weatherproof box, an aluminum breadboard that was replaced with a two-story aluminum frame in 2002, a heating system for Arctic winter/spring conditions and a cooling system for mid-latitude summer-

time. As shown in Figure 3.5, the instrument is contained in a watertight aluminum box that has a Plexiglas window (UV-grade) mounted on the top to furnish the instrument with a zenith view of the sky. The aluminum boxes were custom designed (the first box was manufactured by Quantum Scientific and the second one by Cases Unlimited Inc.). The exterior walls of the boxes were painted white to reduce the absorption of sunlight and were designed to be portable, yet robust enough to be operated outdoors in the field environment. Inside the first box, there was an aluminum tray which was replaced with an aluminum frame in the second box, with both mounted on anti-vibration mounts. The instrument is mounted on this frame (previously on a breadboard that sat on the tray). The boxes are insulated by 1.27 cm black foam insulation. At the back of the boxes, there are feedthroughs for the power cable and communication cables, and a cooling system is mounted on the side of the second box. A heating circuit and temperature monitor are also installed inside the box to control and record the internal temperature. A schematic diagram of the heating circuit is shown in Figure 3.6. The heating circuit contains a solid state relay that is connected to a temperature controller and heater pads. The temperature controller (CN 77344, OMEGA, Quebec) is set to the required temperature and a solid-state relay (OMEGA, Quebec) acts as a switch while connected to the AC power and heats the heater pads to the required temperature. Internal temperatures in the box are recorded by connecting thermocouples (CHAL-010, OMEGA, Quebec) to a 16-channel temperature monitor (SR 630, Stanford Research Systems, SunnyVale, CA, USA).

3.3 Automated Operation

Continuous measurements are possible using an automated scheme that is remotely controllable. Customized LabVIEW software developed by *Jha* (1999) is used to control the spectrometer settings and to automate data acquisition for long-term monitoring (see

Figure 3.5: The UT GBS system assembled and located inside the second box for the MANTRA 2002 campaign.
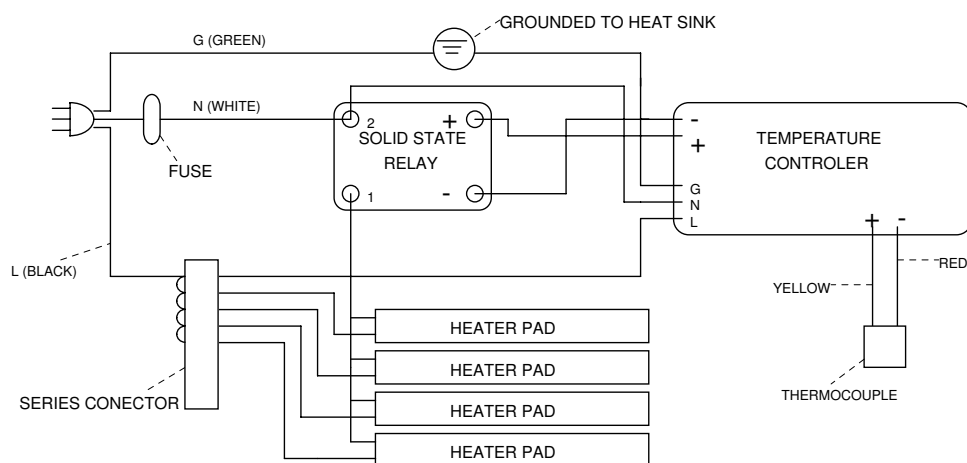
Figure 3.6: Schematic diagram of the heating circuit for the UT GBS system.

the LabVIEW diagrams in Appendix B). One of the features of the code is the use of a short series of 'snapshot' spectra that are taken prior to the recorded spectra in order to optimize the integration time depending on the light level present at the time. Such a procedure facilitates stand-alone operation and the unattended collection of zenith-scattered spectra. To further automate the system, commercial software (pcANYWHERE, Symantec Corp, Cupertino, CA, USA) allows the host PC to be controlled from a distant site. This approach was found to be successful and proved most valuable during Arctic campaigns. Spectra are routinely downloaded during the field campaigns and it is possible to check and modify spectrometer settings remotely from Toronto.

Chapter 4

Calibration

Prior to recording the atmospheric spectra, a series of tests is performed in the laboratory to characterize the instrument. These tests include bias, dark current and inter-pixel variability measurements to characterize the CCD detector, resolution and SNR measurements to characterize the spectrometer and the detector, and polarization and stray light tests to determine the performance of the optical set-up.

4.1   Bias Calculation

An electronic offset, called the bias, is added to all pixels of the CCD chip to prevent readings of any spurious negative signal. The bias is determined and subtracted from measured spectra prior to further data analysis. To calculate the bias, first in the laboratory a set of dark spectra with different integration times are taken, then a linear fit is performed on the dark counts versus integration time for each pixel. The y-intercept of this fit is the bias. Bias calculation is normally perfomed prior to, during and after each field campaign.

Figure 4.1 shows the derived bias during the four Arctic campaigns of 1999, 2000, 2001 and 2003 which show a gradual increase across the chip. The bias for the Eureka 1999 field season shows the smoothest values across the chip with few anomalous pixels.
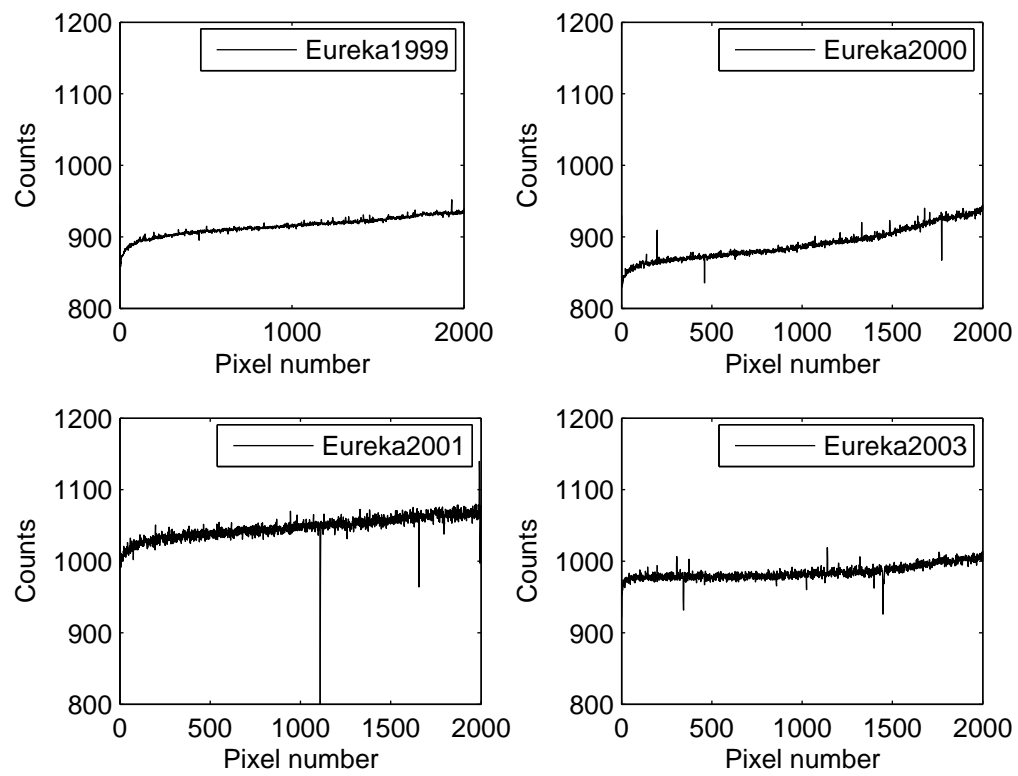
Figure 4.1: Calculated bias for binning across all 800 rows for the Arctic campaigns.

However, for the Eureka 2000 field campaign, the slope is steeper and several pixels with anomalous values are seen. Prior to the 2001 field season, in order to reduce the CCD operating temperature, the CCD was pumped by ISA; however they accidentally mounted it backward in the camera head and its controller produced more spurious signal on the chip which resulted in flipped high-noise spectra and a higher bias with more anomalous counts. After the 2001 field season, the CCD was re-installed correctly and its controller was fixed which resulted in a bias of about 1000 counts and decreased slope.

4.2 Dark Current Measurements

The term 'dark current' is used for the thermally generated charge carriers. The dark current can be written as:

$$I_D = Ce^{-eV_{BG}/kT} \tag{4.1}$$

where C is a constant, V_{BG} is the band gap of silicon (1.1 V), k is Boltzmann's constant, e is the electric charge and T is the absolute temperature (*Shepherd*, 2002). Therefore the number of dark counts is a function of the CCD temperature and the integration time. To determine the dark counts for our instrument, the calculated bias is subtracted from each pixel's dark counts. Then the dark count per second is derived as the average of these bias-subtracted dark counts divided by their integration times.

As shown in Figure 4.2, the dark current spectra for the 1999, 2000, 2001 and 2003 Arctic field campaigns show strong dependence on the CCD's operating temperature. The CCD vacuum was intact during the Eureka 1999 field season which resulted in an average CCD temperature of about 235 K and an average dark current of 50 counts per second. However by the time the Eureka 2000 field season started, the average CCD operating temperature had risen to about 245 K, resulting in 120 average dark counts per second. Prior to the Eureka 2001 campaign, the CCD was pumped which reduced the average CCD temperature to 232 K and the average dark counts to 40, although the
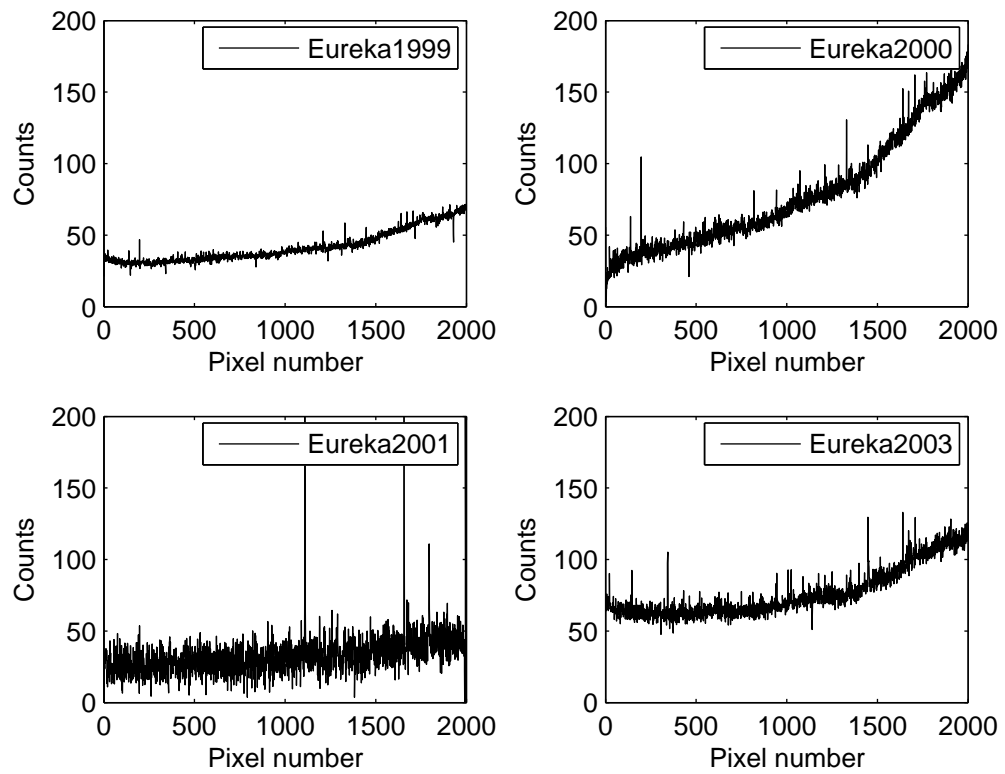
Figure 4.2: Calculated average dark count per second for the Arctic campaigns, measured during the campaigns.

fluctuation of dark counts was increased. After the Eureka 2001 campaign, the average CCD temperature increased due to problems with the vacuum and CCD electronics. Thus in an attempt to reduce the CCD temperature, the CCD chip was cleaned by the manufacturer. The average CCD temperature was reduced to 242 K and the average dark counts to 100 after the cleaning process. Our observations support the fact that dark current intensity decreases by about a factor of two each time the CCD temperature is lowered by 7°.

4.3   Resolution and Sampling Ratio

There are several ways to determine the spectral resolution. One widely used method is to define the spectrometer's resolution at a particular wavelength across the CCD detector as the full width at half maximum (FWHM) of a narrow spectral line at that wavelength. We use three pencil-style spectral calibration lamps, Mercury(Argon), Xenon and Neon, which have emission lines in the wavelength region of interest and help us to determine how the spectral resolution changes across the CCD. The resolution tests are normally repeated prior to, during, and after each field campaign.

Figure 4.3 shows the resolution across the CCD for the most commonly used grating and slit: 600 grooves/mm and a slit width of 100 μm. The FWHM varies between 0.6-4 nm during the three field Arctic campaigns that this grating was in place. Figure 4.4 shows the resolution for the 400 grooves/mm grating which was the default grating for Arctic campaign of 1999 since the 600 grooves/mm grating fell off during shipment to the Arctic. The FWHM for 400 grooves/mm and 100 μm slit width varies between 0.9-5.4 nm. Figure 4.5 shows the resolution for the 1800 grooves/mm grating and 100 μm slit width. This grating has a smaller bandwidth, 66 nm, however it provides a higher resolution of 0.2-0.5 nm, which can be used to record high-resolution spectra in the BrO and OClO regions.
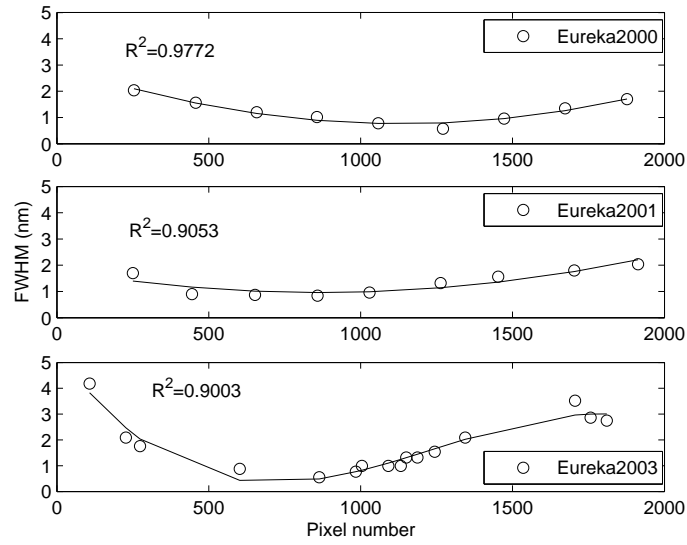
Figure 4.3: Measured resolution across the CCD chip for the 600 grooves/mm grating with 100 μm slit width (no measurements were made with this grating in 1999).
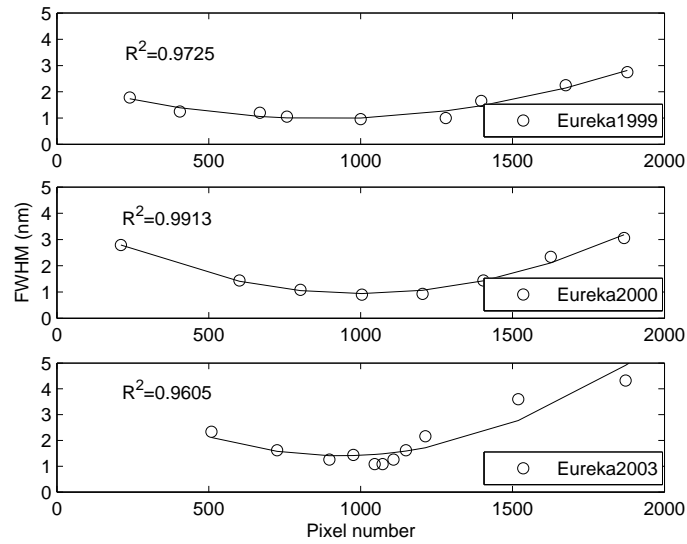
Figure 4.4: Measured resolution across the CCD chip for the 400 grooves/mm grating with 100 μm slit width (no measurements were made with this grating in 2001).
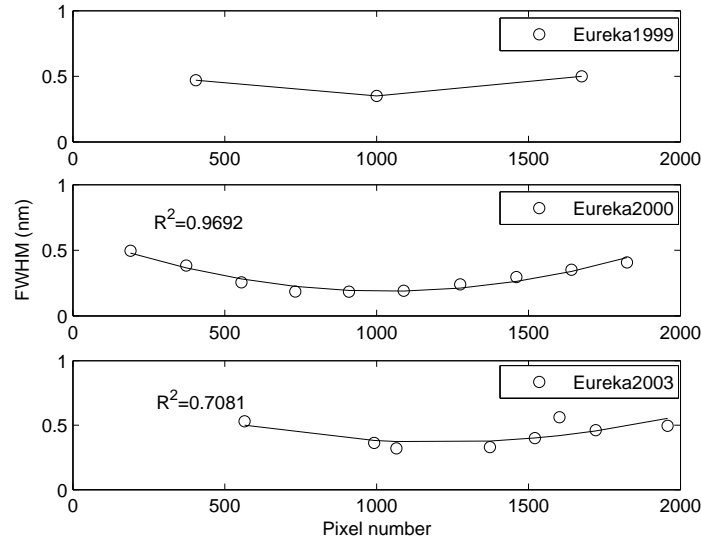
Figure 4.5: Measured resolution across the CCD chip for the 1800 grooves/mm grating with 100 μm slit width (no measurements were made with this grating in 2001).

Looking at the 600 grooves/mm grating, we find that the resolution is minimum in the centre of the chip around 400-450 nm (NO_2 region) and stays fairly constant. In the O_3 region (450-550 nm), it is increasing with increasing wavelength (pixel number), however during the WinDOAS analysis process a polynomial is fitted to the resolution and a variable slit function parameter is defined. A similar pattern is repeated in the other two gratings. Figure 4.6 shows the sampling ratio of approximately 7 pixels per FWHM (0.84 nm) for the 600 grooves/mm grating and slit width of 100 μm, which prevents undersampling (*Roscoe et al.*, 1996).

4.4 Signal-to-Noise Ratio Measurements

The ratio of the light intensity to the sum of all sources of noise is determined to evaluate the quality of the spectra. Generally, any recorded signal which is not desired is called noise and depending on the noise source we divide it into three catagories: dark noise, readout noise and shot noise. Dark noise is generated by the dark signal and is equal to
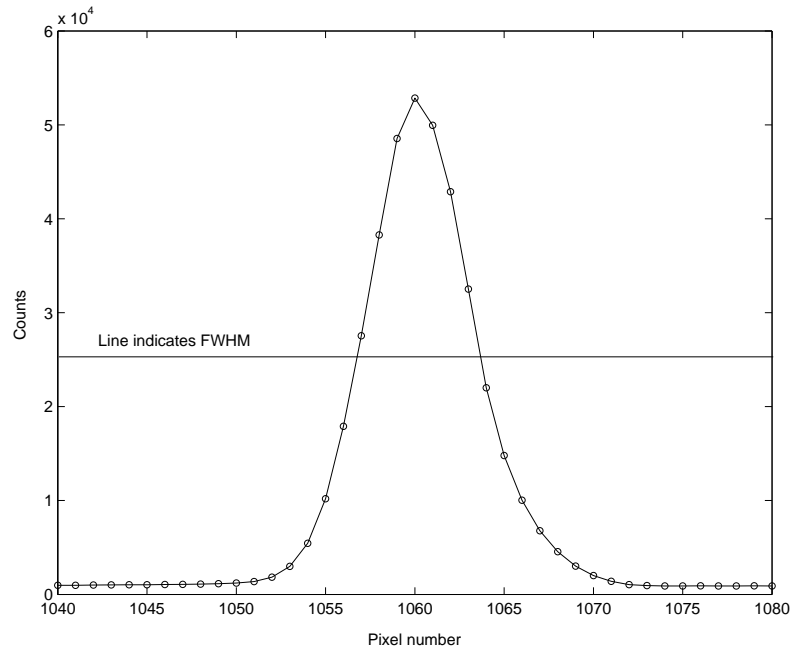
Figure 4.6: Sampling for the 435.8 nm Hg line recorded using the 600 grooves/mm grating and 100 μm slit width.

the square root of the number of electrons in the dark signal. Therefore if the recorded dark count is N_D, the dark noise will be:

$$\eta_D \quad = \quad \sqrt{N_D}. \tag{4.2}$$

Readout noise is signal independent and is generated while the pixels are binned, read out of the horizontal transfer register and their recorded charges are converted to voltage. Readout noise contains the amplifier noise, generated during the amplification of the signal by the spectrometer's controller, the conversion noise, produced while the analogue signal is converted to digital, and the reset noise, generated by remaining signal while the individual pixels are reset after a measurement (*Shepherd*, 2002). The readout noise for the UT GBS is on the order of 1-20 counts per pixel. Random statistical variations in light intensity introduce shot noise, which is the square root of the corrected signal.

The SNR has three different regimes shown in Figure 4.7 (*Gardner*, 2003). In the first
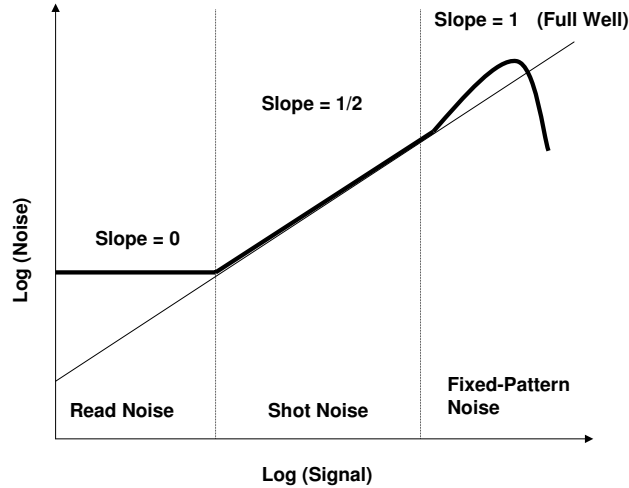
Figure 4.7: The photon transfer curve shows three signal-to-noise ratio regimes (*Gardner*, 2003).

regime, the signal is small, thus the readout noise is the dominant noise source and the SNR stays constant. In the second regime, the shot noise becomes the dominant noise source as the signal increases and the slope for a signal-noise log-log plot is expected to be one-half. In the last regime, the CCD response is non-linear and it becomes saturated with high signal levels so the SNR reaches a second plateau (*Mackay*, 1986). To record accurate spectra with longer exposure times such as for twilight measurements, the second regime is desirable as the shot noise dominates. Using a quartz-halogen lamp as a light source, a series of SNR tests at integration times between 100 ms to 2 s, limited by the lamp signal level, were performed from May to July 2003. The SNR calculations were done for two regions of the CCD pixels: 575-1000 and 1000-1770 which represent wavelength regions of 400-450 nm (NO_2 region) and 450-550 nm (O_3 region) respectively for the 600 grooves/mm grating. The signal was calculated by subtracting the dark spectrum from the light spectrum and averaging the result over the region of interest. The noise was calculated from:

$$N = \sqrt{\left(\sum_i (sp_{1,i} - sp_{2,i})^2 / 2N_p\right)} \qquad (4.3)$$
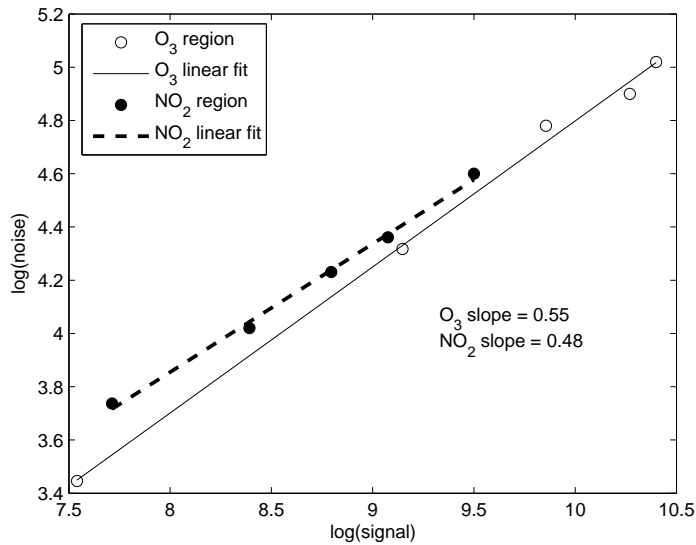
Figure 4.8: Log-log plot of signal and noise for the O_3 and NO_2 regions using laboratory measurements.

where N is the noise, sp_1 and sp_2 are two consecutive spectra, N_p is the number of pixels in the region and the sum is over the different pixels (*Gardner*, 2003). Figure 4.8 shows that the noise is linearly related to the signal with a slope of 0.55 for the O_3 region and 0.48 for the NO_2 region. These slopes are quite close to the expected value for the second SNR regime, 0.5, which is desired. The calculated SNR from the 1999 and 2000 Arctic measurements is typically 650-750 in the O_3 region and 600-770 in the NO_2 region for exposure times of 100-500 ms (which corresponds to the exposure time for a typical Arctic noon spectrum) and 3350-3400 in the O_3 region and 3380-3410 in the NO_2 region for exposure times of 25-30 s (which corresponds to the exposure time for a typical Arctic twilight spectrum near 90° SZA). Somewhat lower SNRs were obtained in 2001 and 2003. The limiting SNR is 4050, assuming on-chip binning of all 800 pixels in a column and 2^{16} counts per pixel.

4.5   Polarization Tests

In UV-visible zenith-scattered observations, measured solar photons are Rayleigh scattered. During the day, as the solar zenith angle changes, we record zenith-scattered spectra with different polarizations. Because the diffraction gratings are polarization-sensitive and diffract beams with different polarization angles differently, this introduces unwanted structures in the spectra which may interfere with absorption features of atmospheric constituents (see Figure 3.2 and Figure 3.3) (*Wolfe*, 1997). Thus it is wise to depolarize the zenith-scattered beam prior to the spectrometer's entrance slit. This is done using the liquid light guide which depolarizes the incident light through multiple total internal reflections. However, if the LLG does not totally depolarize the incident light, polarization features change during the day. Therefore once the ratio of a twilight to noon spectrum is taken in the DOAS technique, some additional features are introduced due to the changing polarization.

A series of tests were performed with the most frequently used grating (600 grooves/mm) and a camera polarizer, first to evaluate the polarization sensitivity of the grating and in turn to determine the depolarization capability of the LLG. Using a quartz-halogen lamp, a set of spectra with different exposure times were recorded first with no polarizer and then with the polarizer, which was placed inside the f-number matcher at four relative positions to its polarization axis, vertical, horizontal, 45º to the vertical axis, and 45º to the horizontal axis.

To evaluate the grating's sensitivity to the polarized light, the ratio of the four polarized spectra to the spectrum with no polarizer was taken at every exposure time without having the liquid light guide in the optical set-up. If the grating treats all the beams in the same manner, there should be no difference in these ratios. However in Figure 4.9, the four polarization curves diverge after about pixel 400, which shows the sensitivity of the 600 grooves/mm grating to polarized light. Due to the low output of the quartz-halogen lamp before pixel 400, the recorded signal in that region is essentially the dark signal.
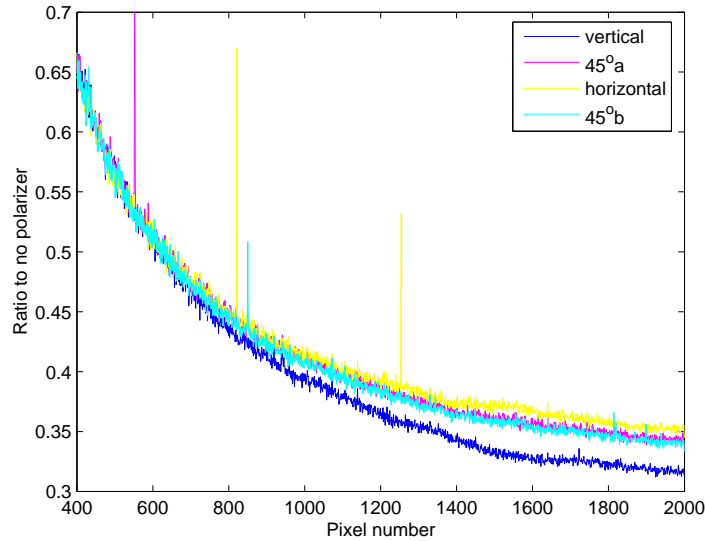
Figure 4.9: Ratios of spectra recorded with a polarizer in the f-number matcher to a spectrum recorded with no polarizer, with all taken at a 10 s exposure time. The results are similar for other exposure times.

Also the two 45° curves are expected to be the same; the slight difference between the two in Figure 4.9 comes from the uncertainties in determining the polarization axis.

To determine the depolarization capability of the LLG, the tests were repeated for the same four relative positions when the LLG was placed in the optical set-up. Figure 4.10 shows similar shapes for the curves to those in Figure 4.9; however the divergence of the curves after pixel 400 is not as significant. The fact that all the curves do not collapse to one indicates that the light is not completely depolarized, although the maximum difference while using the LLG is 1% compared 5% for no LLG. Also the ratio of the horizontal position to the vertical after pixel 400 remains constant which means the polarization residuals not removed by the liquid light guide should not introduce more uncertainty to the DOAS retrieval.
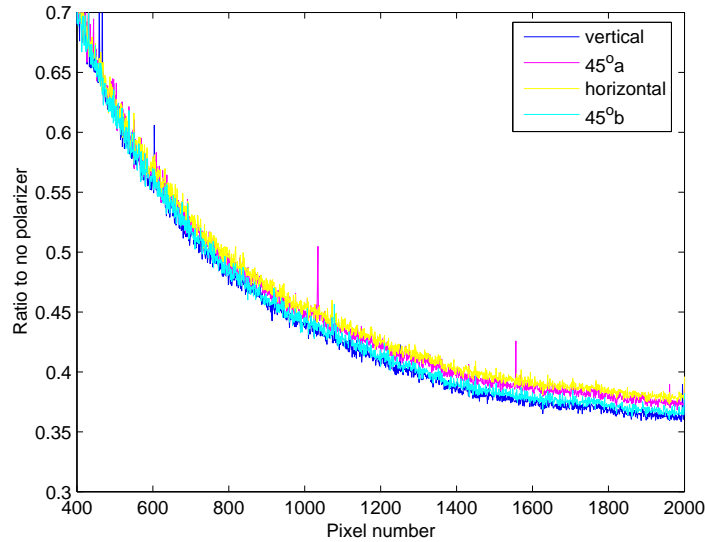
Figure 4.10: Ratios of spectra recorded with a polarizer on the input optics, before the liquid light guide, to a spectrum recorded with no polarizer, with all taken at a 10 s exposure time. The results are similar for other exposure times.

4.6 Stray Light Tests

Stray light is the light detected in an optical system (e.g. the CCD) which did not travel along the instrument's primary optical axis. Since the stray light can be scattered towards the detector at different angles, which differ from the designated optical path, it generates spurious signal on the detector which is superimposed on the real signal, particularly at short wavelengths. Thus, the stray light value needs to be determined prior to the operation of the system. A series of tests were performed using a quartz-halogen lamp as a light source, the 600 grooves/mm grating, which has a bandwidth of 330-570 nm, and a long-wave pass filter (Andover 590FG05) that cuts off wavelengths shorter than 600 nm. First, a set of spectra was recorded without the filter to determine the total signal and the required exposure time, then using the measured exposure time and placing the long-wave filter on the input optics, another set of spectra was recorded called filtered spectra. Finally, using the same exposure time and closing the spectrometer's entrance
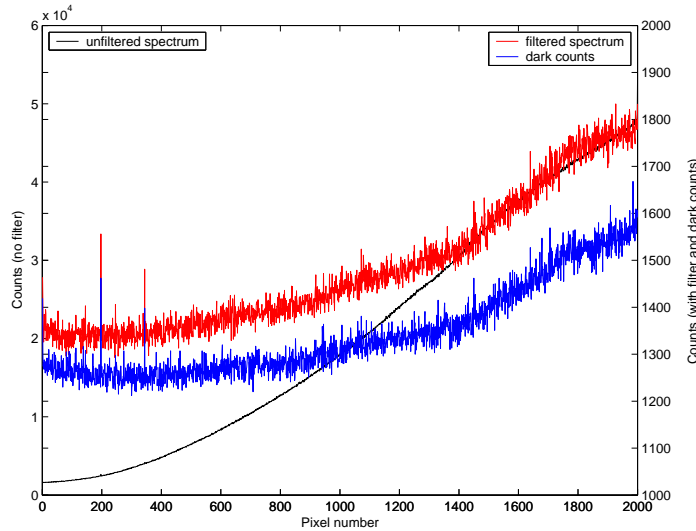
Figure 4.11: Unfiltered, filtered and dark spectra recorded for the stray light tests. Filtered and dark spectra scales are shown on the second axis.

slit, a set of dark spectra was recorded as shown in Figure 4.11. The stray light value is determined by subtracting the dark spectrum from the filtered spectrum. The stray light was calculated as a percentage of the total signal and shown in Figure 4.12.

4.7   Inter-Pixel Variability (IPV)

There can be pixels in CCD arrays that are physically different either in size, thickness of coating or both. The result is a small variation in the brightness of different pixels which should be characterized prior to the operation of the system. To determine the inter-pixel variability (IPV) of the CCD detector, a series of tests were performed in the laboratory using a quartz-halogen lamp as the light source, several filters and white cards. To have a uniform, wavelength-independent signal at the CCD location, the grating was replaced by a white card and a set of spectra for five wavelength target positions were recorded. The results showed little difference as a function of wavelength target position. A polynomial was fitted to and subtracted from all 2000 pixels across the CCD. To have the residuals with the least amount of structure while still correcting for the outstanding
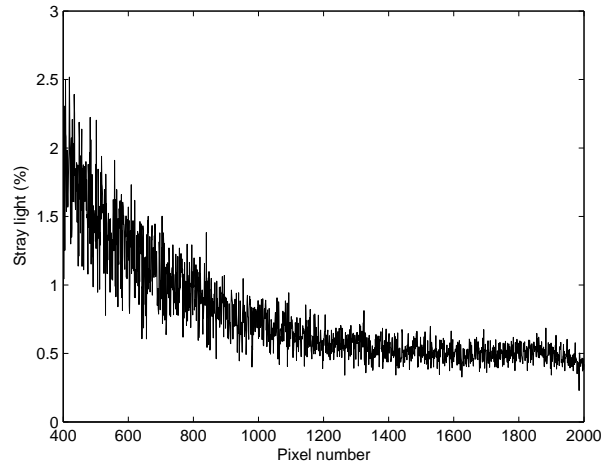
Figure 4.12: Stray light value shown as a percentage of the total signal.

pixels, a box-car average of 10 points was used. To avoid the sharp slope at the edges of the CCD the first and last 50 pixels were omitted. Finally, a set of IPV values were calculated for the other 1900 pixels to account for their varying responses. However, these values were very small compared to the bias and dark current corrections, and it was found that correcting for the IPV resulted in more scatter and worse spectral fits. Therefore no IPV correction was applied to the spectra analysed in this work.

Chapter 5

Mid-Latitude Measurements

The UT GBS has been one of the ground-based instruments in the Middle Atmosphere Nitrogen TRend Assessment (MANTRA) project *Strong et al.* (2005). During the past four campaigns in 1998, 2000, 2002, and 2004, the UT GBS was deployed in Vanscoy, Saskatchewan (52ºN, 107ºW, 511 m) in late August and took measurements through the pre-flight tests of the balloon instruments and the actual balloon flight. In this chapter, the UT GBS observations of O_3 and NO_2 column densities during the 2000 and 2002 campaigns are presented. Results from 1998 were discussed by *Bassford et al.* (2001, 2005) and data analysis for the 2004 campaign is underway by Ph.D. candidate A. Fraser.

5.1 The MANTRA Project

MANTRA consists of a series of high-altitude balloon flights conducted at Vanscoy, Saskatchewan biannually in late summer when the stratospheric zonal wind velocity changes from easterly to westerly, a phenomenon referred to as turnaround. During the turnaround period, the stratosphere is dynamically quiescent and under photochemical control (*Fioletov and Shepherd*, 2003; *Wunch et al.*, 2005) and the payload remains within the telemetry range (∼400 km) for the duration of the mission (typically 18 hours).

The primary objective of the MANTRA project is to investigate changes in the concentrations of O_3 and other related species, particularly the NO_y family, in the mid-latitude stratosphere (*Strong et al.*, 2005). Total columns and vertical profiles of O_3 and other stratospheric species that control the mid-latitude O_3 budget, such as NO_2, were measured by a suite of instruments on the balloon together with ground-based supporting instruments and regular ozonesonde flights.

5.2   Measurements

During the two MANTRA campaigns considered in this work, 2000 and 2002, the UT GBS recorded zenith-scattered spectra from ∼340 to 580 nm continuously throughout the day, with twilight measurements made for SZAs from 85º to ∼95º during both sunrise and sunset. The automated in-house LabVIEW software (described in Appendix C) was used during both campaigns, and allowed us to choose the CCD regions of interest, and the exposure time and number of accumulations comprising a spectral set in such a way as to maximize the total signal on each spectrum throughout the day. In order to avoid temporal smearing, the maximum total accumulation time was restricted to 5 minutes, corresponding to a change in SZA of about 0.7º during twilight. The recorded spectra were analyzed using the DOAS technique explained in Chapter 2.

5.2.1   Ozone Vertical Columns

O_3 DSCDs were retrieved from zenith-scattered spectra using the software described in *Bassford et al.* (2005). Converting retrieved O_3 DSCDs to VCDs requires accurate knowledge of the transfer of radiation through the atmosphere for the calculation of the appropriate AMFs. For O_3 and NO_2 AMF calculations, a radiative transfer model was used with the air and O_3 number densities input from ozonesonde data (explained in Chapter 8) (*McLinden*, 1998). Langley plots of DSCDs versus AMF were used to derive
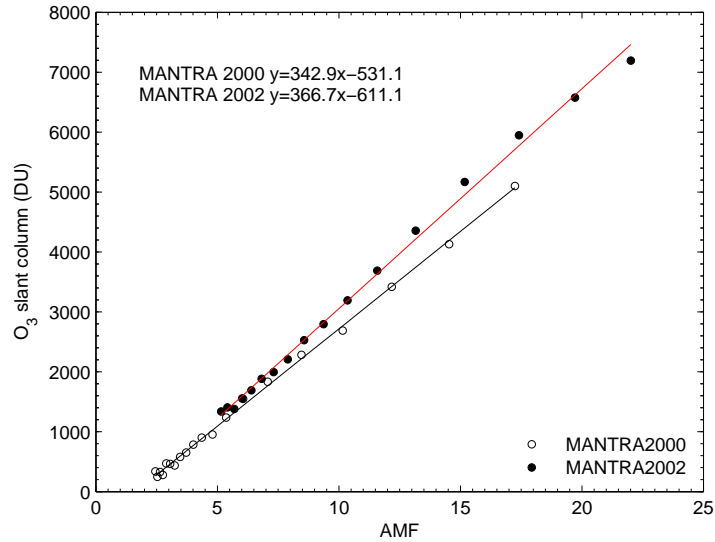
Figure 5.1: O_3 Langley plot on the day of the reference spectrum for both MANTRA 2000 (day 237, August 25) and 2002 (day 233, August 21). The slope represents O_3 vertical column density and the intercept is the negative of the O_3 reference column density.

the O_3 VCDs, as O_3 is a diurnally slowly-varying species. Figure 5.1 shows such a plot for the days that reference spectra were recorded during MANTRA 2000 and 2002.

During MANTRA 2000, a single bias spectrum was derived from dark current measurements in the field and daily dark currents were calculated as the average of the 1-s dark currents recorded every 40 cycles during the day. Corrected spectra were derived by subtracting the bias and daily dark current. The in-house DOAS software uses a shift and stretch procedure to perform the wavelength calibration. The common reference spectrum which was recorded at high noon under clear sky conditions on day 237 at SZA 56º, was first calibrated against a 90º SZA spectrum. All twilight spectra were then calibrated against the common reference spectrum using the 450 to 545 nm wavelength range. This range was used both for the calibration and the fitting region for O_3. The cross sections of O_3, NO_2, O_4 and H_2O were smoothed to the instrument resolution (FWHM) measured in the middle of the CCD chip, 1.24 nm, using a Gaussian function. The instrument's lineshape was derived for the 600 grooves/mm grating (used during this campaign) and
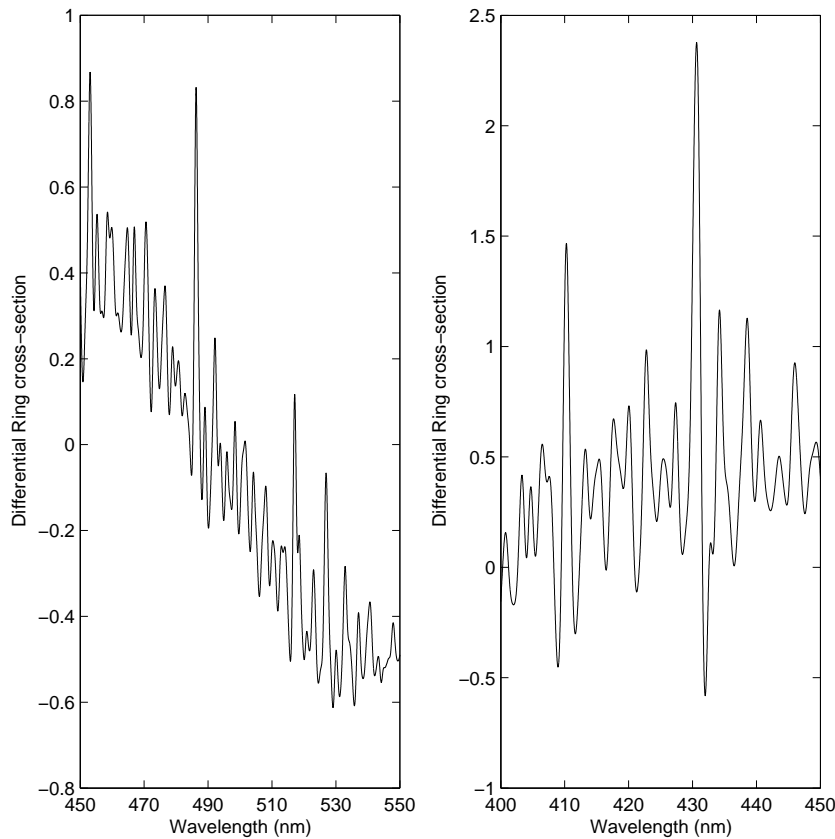
Figure 5.2: The differential Ring cross section calculated for a 1.24 nm slit function using K. Chance's model. The left panel shows the Ring contribution to the O_3 fitting region. The right panel shows the Ring contribution to the NO_2 fitting region.

100 μm slit width from the on-site measurements using calibration lamps. In this work, the differential Ring spectrum, shown in Figure 5.2, was created using a solar reference spectrum from 230-800 nm at 0.01 nm resolution in vacuum wavelength, accurate to better than 0.001 nm above 305 nm. The solar spectrum was convolved with the instrument's slit function, then convolved with rotational Raman cross sections to generate a Ring effect source spectrum. Finally, a cubic polynomial was fitted to and subtracted from the ratio of the Ring effect source spectrum to the solar reference spectrum giving a differential Ring spectrum (*Chance and Spurr*, 1997).
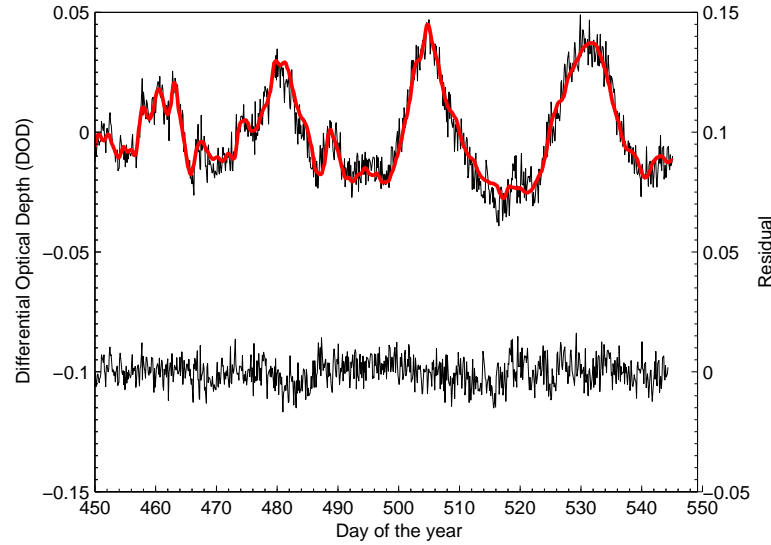
Figure 5.3: The fitted differential optical depth of O_3 and the observed optical depth after subtraction of absorptions due to NO_2, O_4, H_2O, Rayleigh scattering, and the Ring effect on day 236, 2000 at SZA 90º during sunset. The scale for the residual to the fit is shown on the right axis.

The in-house DOAS software, which uses the Marquardt-Levenberg technique to fit spectra (*Fish*, 1994), was used to derive the differential optical depths of O_3, and O_3 DSCDs for days 231 to 239 (August 19-27, 2000). Figure 5.3 shows measured and fitted O_3 differential optical depth and the fit residual for day 236 (August 24) during sunset. The daily O_3 VCDs were derived as the average of the slopes of Langley plots for sunrise and sunset. The VCDs for MANTRA 2000 are displayed in the top panel of Figure 5.4. The error bars on O_3 VCDs are $\pm 5\%$ (*Bassford et al.*, 2005).

During MANTRA 2002, the recorded spectra contained intense spikes which were first thought to be interference patterns; after further investigation, the source of the problem was identified as the CCD chip electronics. Thus during the campaign, we divided the CCD chip into four horizontal bands (each containing 200 pixels in the vertical) and removed the top and bottom regions as they were contaminated with the most intense spikes. The raw spectra used during this field campaign were the sum of the two middle
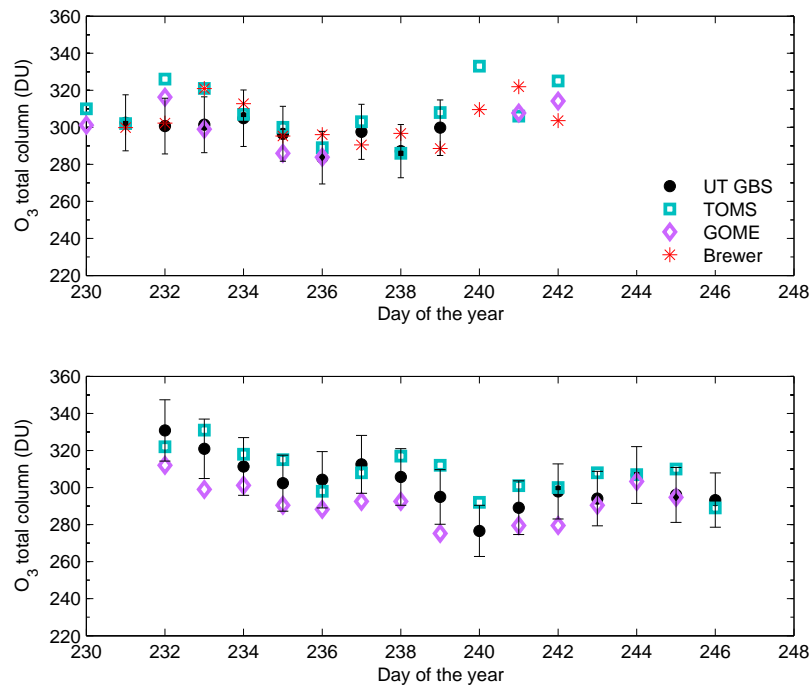
Figure 5.4: Time series of UT GBS O_3 vertical column densities, compared with measurements by the Brewer spectrometer, and the TOMS and GOME satellite instruments. The top panel shows the results for MANTRA 2000 and the bottom panel shows MANTRA 2002 results (Section 5.2.3 describes the TOMS, GOME, and Brewer data).

regions of the CCD.

Analysis of MANTRA 2002 data started with the derivation of individual daily bias spectra using a set of dark current measurements recorded at different exposure times each night. This was necessary because it was found that the electronic offset did not remain constant. A daily dark current spectrum was used in the raw spectra correction calculated in the same way as for MANTRA 2000. The MANTRA 2002 reference spectrum was recorded on day 233 (August 21, 2002) at SZA 40º. The resolution was derived from the on-site measurements for the 600 grooves/mm grating and 80 μm slit width. The resolution is 0.72 nm in the middle of the CCD chip. O_3 DSCDs and VCDs were derived for days 232 to 246 (August 20-September 3, 2002), and the latter are shown in the bottom panel of Figure 5.4.

5.2.2 NO_2 Vertical Columns

NO_2 DSCDs were derived in a similar manner to those for O_3, as just described. The calibration region used for the NO_2 retrieval was 420-450 nm while the fitting region was from 405 to 450 nm. Figure 5.5 shows measured and fitted NO_2 differential optical depth and the residual to the fit for day 236 (August 24, 2002) during sunset.

To convert NO_2 DSCDs to VCDs, we need accurate knowledge of the AMFs and the amount of NO_2 in the reference spectrum, the reference column density (RCD). The RCD value can be either calculated using a chemical box model or can be determined independently of a model by using observed DSCD values. In this work, NO_2 RCDs were determined by using pseudo-Langley plots of NO_2 DSCDs versus NO_2 AMFs in the SZA range of 80º-85º, where the change in NO_2 column due to photodissociation is expected to be small (*Vaughan et al.*, 2005). Thus, this relationship is approximately linear and the intercept represents the negative NO_2 RCD. The NO_2 RCD for each MANTRA campaigns is the average of RCDs for all days during that campaign and Figure 5.6 shows the pseudo-Langley plot for the days of the reference spectrum for MANTRA
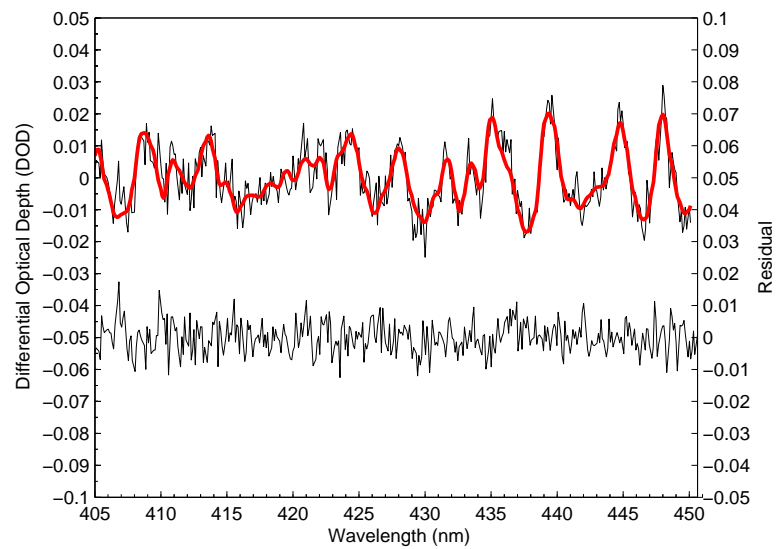
Figure 5.5: The fitted differential optical depth of NO_2 and the observed optical depth after subtraction of absorptions due to O_3, O_4, H_2O, OClO, Rayleigh scattering, and the Ring effect on day 236, 2000 at SZA 90º during sunset. The scale for the residual to the fit is shown on the right axis.
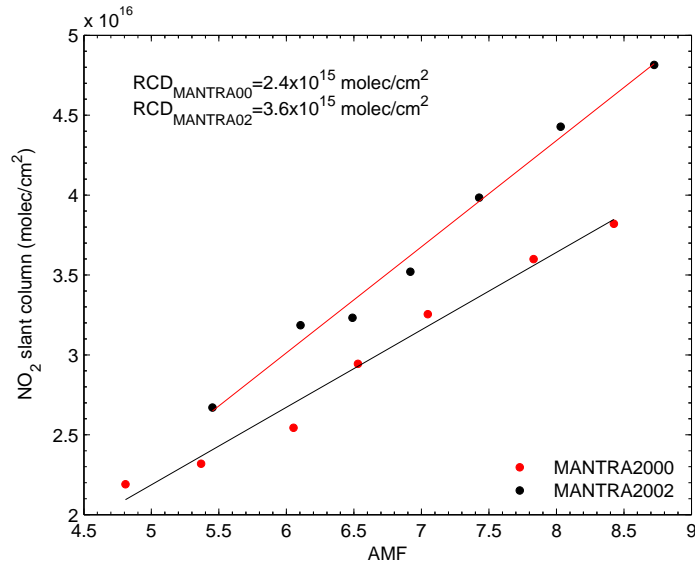
Figure 5.6: The pseudo-Langley plot for NO_2 in the SZA range of 80º-85º for day 237 (reference day for MANTRA 2000) and day 233 (reference day for MANTRA 2002).

2000 and 2002.

In Figure 5.7, NO_2 DSCDs on day 236 measured at sunset during the three campaigns, 1998, 2000 and 2002 are presented. One interesting feature in Figure 5.7 is that the NO_2 measurements taken on day 236, 1998 during sunset are consistently lower than the measurements taken in 2000 and 2002 and the overturn in NO_2 DSCDs at sunset is already observable at SZA 93.5º, while during 2002 it can not be detected as high as SZA 95º.

Figure 5.8 shows the UT GBS measurements of NO_2 vertical column densities calculated using Equation 2.15 at SZA 90º during sunrise and sunset for 2000 and 2002. The error bars, $\pm 12\%$, are the total uncertainty estimate on NO_2 vertical column densities (*Bassford et al.*, 2005).

NO_2 diurnal, seasonal and latitudinal variations are large and mostly attributed to homogeneous reactions (*Preston*, 1995). Figure 5.9 shows the chemical box model calculation of the diurnal variation in NO_2 vertical columns for mid-latitude summer (*Preston*, 1995). The NO_2 diurnal variation occurs due to its photochemical equilibrium with NO
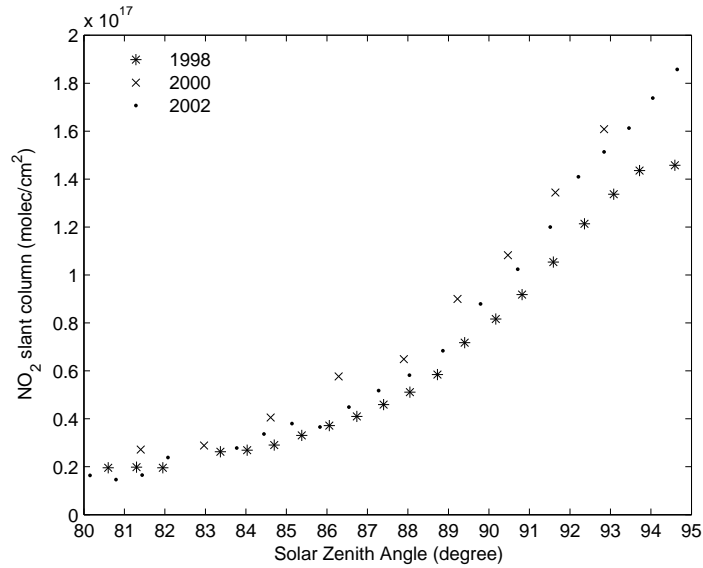
Figure 5.7: NO_2 differential slant columns for day 236 (August 24) for MANTRA 1998, 2000 and 2002.

during the day and by formation of its reservoirs. During the night, NO_2 is converted to its night-time reservoirs, N_2O_5, HNO_3 and $ClONO_2$, which causes a gradual decrease in the NO_2 column during the night. The same calculation using MANTRA 2000 data for the reference day is presented in Figure 5.10.

Figure 5.11 presents the ratio of NO_2 total columns at sunrise (SZA=90º) to NO_2 total columns at sunset (SZA=90º) as an estimate of diurnal variability in NO_2 column during MANTRA 2000 and 2002. During MANTRA 2000, the NO_2 diurnal variability was in the range of 0.47-0.67 which is just below the expected value of 0.7 for summer mid-latitude; however during MANTRA 2002, the variability was 0.61-0.74, which is consistent with previous studies (*Senne et al.*, 1996).

5.2.3   Comparison with Other Measurements

To compare our measured O_3 total columns with other observational data sets, data was obtained from the MANTRA Brewer spectrophotometer and from the TOMS and GOME
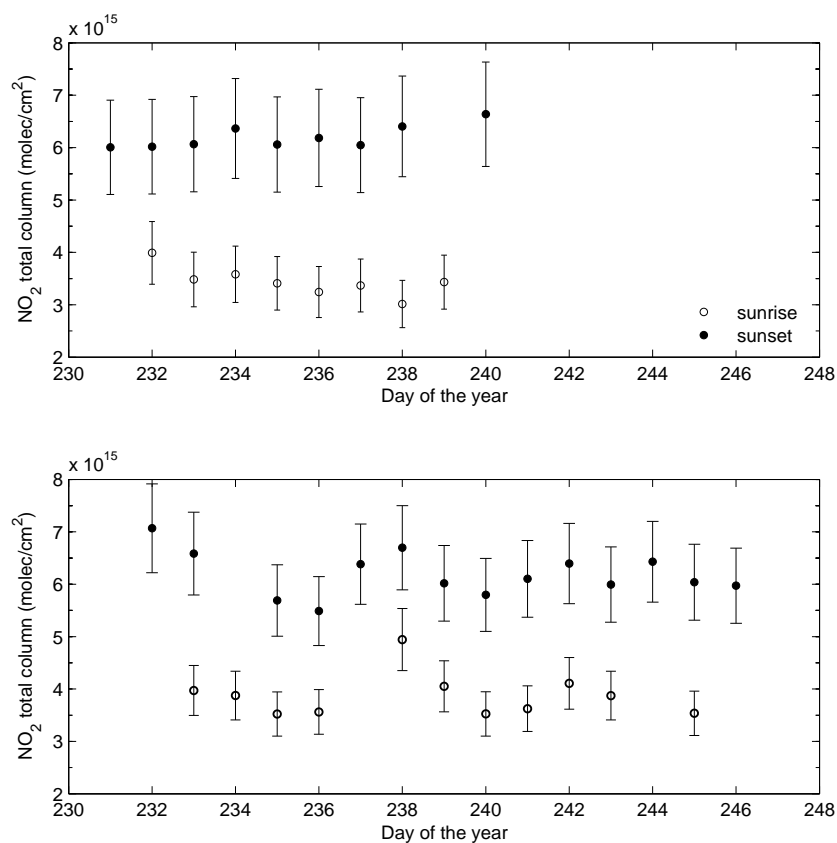
Figure 5.8: Time series of UT GBS NO$_2$ vertical column densities during sunrise and sunset, SZA 90º. The top panel shows the results for MANTRA 2000 and the bottom panel shows MANTRA 2002 results.
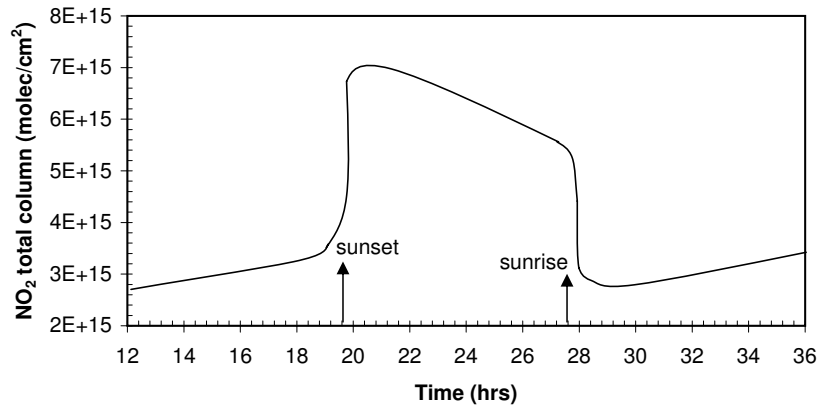
Figure 5.9: The diurnal variation of the NO_2 column based on a typical NO_2 vertical profile for mid-latitude (52°N) in July. Sunset occurs at approximately 19.5 hours and sunrise occurs at appoximately 27.5 hours (*Preston*, 1995).
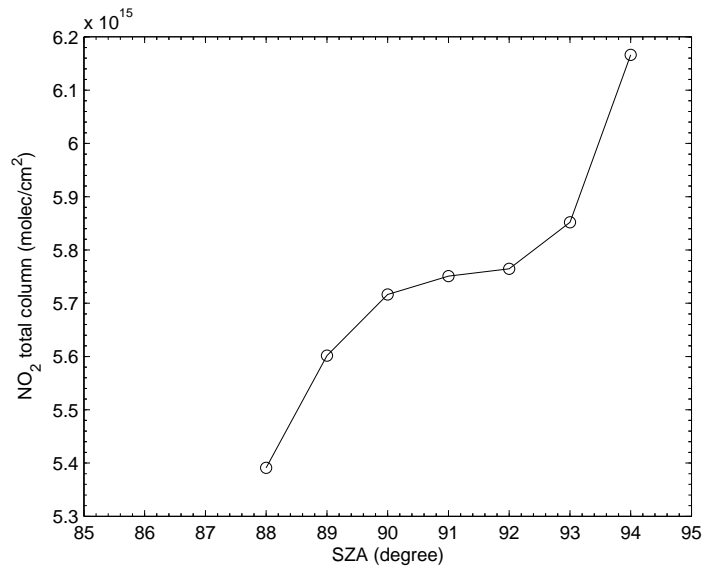
Figure 5.10: The twilight variation of the NO_2 vertical column amount based on MANTRA 2000 measurements during sunset on the day of reference.
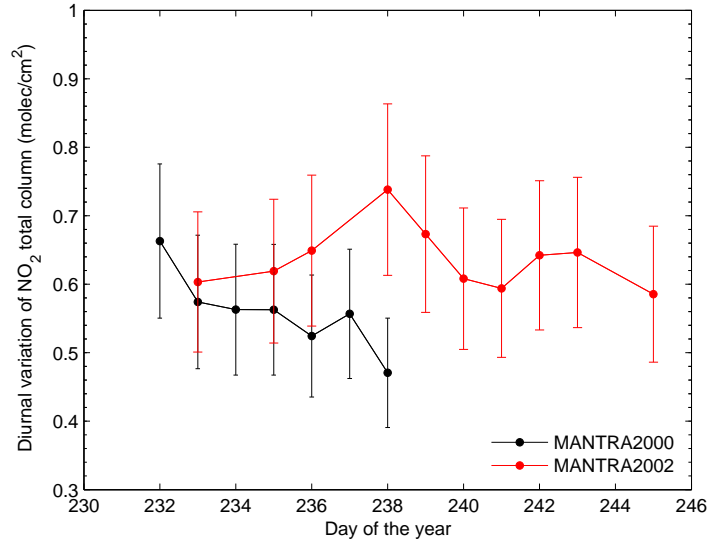
Figure 5.11: The estimate of NO_2 diurnal variability shown as the ratio of NO_2 total column at sunrise SZA 90º to sunset SZA 90º.

satellite instruments. The Brewer O_3 values were available for MANTRA 2000 and they agree with the UT GBS O_3 columns within measurement errors. TOMS is a nadir-looking instument which measures the albedo of the Earth's atmosphere by comparing the radiance of the Earth with the radiance of a calibrated diffuser plate in the UV region. Total ozone is derived from the differential albedo. Data from the Version 8 algorithm for the nearest pixel to Vanscoy is shown in Figure 5.4. It should be noted that there is a latitude-dependent error of -2% to -4% at 50º latitude in this data set (*Bramstedt et al.*, 2002) due to continuing changes in the optical properties of the front scan mirror.

GOME is also a nadir-viewing instrument that measures the solar radiation scattered by the atmosphere in the UV-visible region (240-790 nm) with a resolution of 0.2 to 0.4 nm and a footprint of 40×320 km^2. The emphasis of GOME measurements is on global ozone distributions, also NO_2, BrO, OClO, HCHO, and SO_2 columns can also be retrieved from its dataset. O_3 total columns used for this comparison are from the GDP 4.0 Total Column Algorithm, using the correction for cloud contamination using cloud information inferred from GOME measurements (data obtained from The World Data

Centre for Remote Sensing of the Atmosphere, http://www.wdc.dlr.de:8082/index.html).
In Figure 5.4, the UT GBS O_3 columns agree with both TOMS and GOME within
measurement errors during both MANTRA 2000 except day 232 and 233 when TOMS
reports values $\sim$2% higher than the UT GBS. During MANTRA 2002, the UT GBS
reports O_3 values which are the same with TOMS and GOME measurements within
error bars, however GOME O_3 columns are systematically lower than the UT GBS and
TOMS values.

5.3   Summary

The O_3 VCDs for all measurement days during MANTRA 2000 and 2002 were retrieved
using the DOAS retrieval method and compared with the on-site Brewer spectropho-
tometer data, TOMS and GOME satellite instruments. The comparison resulted in an
agreement of $\sim$6% or better for both the MANTRA 2000 and 2002 field seasons.

The NO_2 total columns during sunrise and sunset were retrieved using the average
NO_2 RCD values determined from NO_2 DSCDs. The expected diurnal variability of the
NO_2 columns was captured by the retrieved total columns. During MANTRA 2000,
the diurnal variability decreased throughout the measurement period from 0.67 to 0.47;
however during MANTRA 2002 the diurnal variability was $\sim$0.6-0.7. The NO_2 DSCDs
retrieved during this work are being used by S.M.L. Melo to derive NO_2 vertical profiles.

Chapter 6

Arctic Measurements

UT GBS O_3 and NO_2 zenith-sky measurements have been made annually at the AStRO facility at Eureka every spring since 1999. This work focuses on data from 1999 to 2003. During spring 2000, elevated OClO slant column densities were also measured by the UT GBS. In addition, data from the Meteorological Service of Canada Fourier transform infrared spectrometer (MSC FTS) and the Denver University high-resolution Atmospheric Emission Radiometric Interferometer (DU AERI-X) are discussed. The MSC FTS has made solar observations during fall and spring at AStRO since 1993, measuring column amounts of HF, CH_4, N_2O, O_3, NO, NO_2, $ClONO_2$, and HNO_3. The DU AERI-X measured CH_4, N_2O, and HNO_3 columns during 1993-2002.

In the first part of this chapter, two different DOAS algorithms which were applied to UT GBS data are compared and the O_3 and NO_2 VCDs resulting from this comparison are presented. Also, for the winter/spring period of 1999, 2000, 2001, and 2003, the UT GBS O_3 VCDs are compared with MSC FTS data, ozonesondes, and TOMS and GOME. UT GBS NO_2 VCDs and MSC FTS NO_2 vertical columns for winter/spring of 1999 and 2000 are presented. The UT GBS measurements of OClO DSCDs for winter/spring 2000 are shown.

(a) Circumpolar map

(b) AStrO building

Figure 6.1: The AStrO observatory located at 80.1ºN, 86.4ºW, at 11.6 km from Environment Canada's Arctic weather station. (www.lib.utexas.edu/maps/polar.html)

6.1 Site Description

AStrO, the Arctic Stratospheric Ozone Observatory at Eureka, shown in Figure 6.1, is located at an altitude of 612 m above sea level at 80.1ºN, 86.4ºW and at a distance of 11.6 km from the Eureka weather station. AStrO is one of the NDSC (Network for the Detection of Stratospheric Change) primary Arctic sites and its location is ideal for stratospheric measurements as it lies directly below the point of maximum stratospheric variability (*Harvey and Hitchman*, 1996). The winter polar vortex regularly passes over AStrO and thus measurements both inside and outside the vortex region can usually be made from this single location.

6.2 UT GBS Measurements

The UT GBS recorded zenith-scattered spectra in the wavelength range ~320 to 620 nm during four Arctic campaigns which took place in winter/spring at AStrO, Eureka from 1999 to 2003 with the exception of winter/spring 2002. The 2002 campaign at Eureka was canceled due to unforseen circumstances. Some measurements were made at Resolute Bay in 2002 but proved to be of poor quality, largely thought to be due to

Observation Period	O_3	NO_2	OClO
Mar.22-Apr.11, 1999	DSCD,VCD	DSCD,VCD,profiles	-
Feb.24-Mar.31, 2000	DSCD,VCD	DSCD,VCD,profiles	DSCD
Mar.01-Mar.23, 2001	DSCD,VCD	-	-
Mar.20-Apr.15, 2003	DSCD,VCD	DSCD,VCD	-

Table 6.1: The UT GBS measurement periods and data products for the 1999, 2000, 2001 and 2003 Arctic campaigns at Eureka.

electromagnetic interference from a nearby radar system. Table 6.1 summarizes the UT GBS measurement periods and data products for each of the four Arctic campaigns.

6.3 Data Analysis

6.3.1 Preprocessing of the Data

To preprocess the UT GBS 1999 and 2000 data sets, a single bias spectrum for each campaign was derived from dark current measurements in the field, and daily dark current spectra were calculated as the average of the 1-s dark currents recorded after every 40 zenith-sky spectra during the day. However during laboratory measurements in 2001, it was recognized that bias is not constant therefore, during 2001 and 2003, daily bias spectra were derived from a set of dark currents recorded each night at different integration times. Corrected spectra were derived by subtracting the bias and dark current.

The corrected twilight spectra for SZA of 80° to ~94° during both sunrise and sunset

Campaign Year	Grating (grooves/mm)	Spectral Range (nm)	CCD Mean T (K)	Ref. Spec. (SZA)
1999	400	270-625	235	Mar.24 (79°)
2000	1800 swapping with 600	315-380 310-550	245	Mar.29 (76°)
2001	600	330-560	232	Apr.16 (72°)
2003	600	340-580	242	Apr.9 (73°)

Table 6.2: Measurement, grating and approximate spectral range for the Arctic campaigns.

were considered for the retrieval of O_3, NO_2 and OClO DSCDs. Using WinDOAS, UT GBS zenith-scattered spectra were calibrated in the wavelength range 360 to 545 nm for year 2000 and 405 to 545 nm for 1999, 2001 and 2003 against a common reference spectrum for each campaign. The reference spectra were recorded at high noon under clear sky conditions and they are reported in Table 6.2, together with the spectral range, the CCD mean temperature and the grating used in each campaign.

As shown in Table 6.2, the default grating for UT GBS measurements has been 600 grooves/mm since it provides the optimum resolution and spectral range for O_3 and NO_2 retrievals. The cross sections of O_3, NO_2, OClO, O_4, BrO and H_2O were smoothed using a wavelength-dependent Gaussian slit function parameter which was determined in the wavelength calibration process by a cubic polynomial fit.

A Ring cross section was calculated using K. Chance's model as described in Chapter 5. It was smoothed using the wavelength-dependent Gaussian slit function parameter. Then the Ring cross section was fitted in the second stage of the wavelength calibration process and a Ring amount was determined. Finally, the spectra were analysed using the DOAS technique (explained in Chapter 2) and WinDOAS which resulted in O_3, NO_2 and OClO DSCDs.

6.3.2 DOAS Retrievals

At the start of this project, the in-house DOAS software described by *Fish* (1994) was used for UT GBS data analysis; however, after the winter/spring 1999 and 2000 data sets were analysed, I switched to WinDOAS software which has been developed at IASB/BIRA (*Fayt and van Roozendael*, 2001). Both retrieval codes use the same spectral fitting technique, DOAS, but WinDOAS has some additional features. There is a more sophisticated wavelength calibration process in WinDOAS, which allows a more precise wavelength calibration. During the wavelength calibration process, the Fraunhofer structures of the high-noon reference spectrum are aligned with those of an accurately calibrated high-resolution solar reference atlas (*Kurucz et al.*, 1984) which is degraded to the resolution of the instrument as part of a fitting procedure. The spectral interval is divided into a number of equally spaced sub-windows in which a non-linear least squares (NLLS) fitting algorithm is applied to fit measured intensities to the solar spectrum. The atmospheric constituents' cross sections can be convolved in real-time with a user-defined variable slit function or with the information obtained during the wavelength calibration process. The latter is used in this work.

In order to evaluate WinDOAS software before applying it to the rest of the Arctic data set, the retrieval of O_3 and NO_2 DSCDs for the winter/spring 2000 was performed in WinDOAS using exactly the same retrieval parameters as were used in our existing DOAS software. In the top panel of Figure 6.2, the measured and fitted differential optical depth of O_3 using the existing DOAS software is shown while the bottom panel shows measured and fitted differential optical depth of O_3 for the same day using WinDOAS (both for SZA 90º on day 88, March 28, 2000). Figure 6.3 presents a comparison of NO_2 measured and fitted optical depths between DOAS and WinDOAS on the same day. As seen in these two figures, the spectral fit quality and the differential optical depths for O_3 and NO_2 improved once WinDOAS was applied to the spectra.

Table 6.3 shows standard deviations for the residuals of measured and fitted differen-
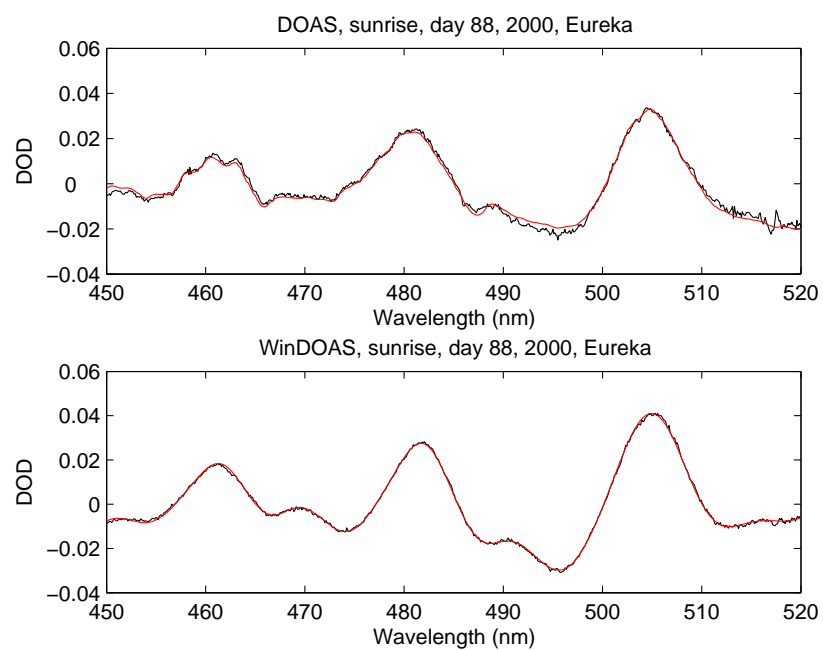
Figure 6.2: DODs for O_3 at SZA 90º for UT GBS zenith-sky measurements made on day 88 (March 28, 2000), sunrise at Eureka (top) using the existing DOAS software and (bottom) using WinDOAS software.

Figure 6.3: DODs for NO$_2$ at SZA 90° for UT GBS zenith-sky measurements made on day 88 (March 28, 2000), sunrise at Eureka (top) using the existing DOAS software and (bottom) using WinDOAS software.

List of species	DOAS (stdev)	WinDOAS (stdev)
O_3 sunrise	8.286×10^{-4}	6.878×10^{-4}
O_3 sunset	7.685×10^{-4}	3.202×10^{-4}
NO_2 sunrise	5.229×10^{-4}	3.943×10^{-4}
NO_2 sunset	5.324×10^{-4}	4.091×10^{-4}

Table 6.3: Average standard deviations of the residuals of the fitted differential optical depths of O_3 and NO_2 on day 88 (March 28, 2000) for the two DOAS algorithms.

Number of Subregions	Standard Deviation
12	5.456×10^{-3}
14	5.187×10^{-3}
16	5.224×10^{-3}

Table 6.4: Comparison of standard deviations of the residuals of the degraded solar spectrum and calibrated reference spectrum on day 88 (March 28, 2000).

tial optical depths of O_3, which are on average decreased by 38% for WinDOAS compared to the existing DOAS code for the day of reference spectrum for recorded spectra in SZA range 85º to ~94º (~80 DOD fits). Standard deviations for the NO_2 residuals are decreased by 24% for the same day.

Another improvement in the results of WinDOAS compared to the existing DOAS software is the capability of dividing the wavelength calibration region into subregions and minimizing the residuals between the degraded solar spectrum and the reference spectrum in the subregions to achieve the best possible wavelength calibration parameters, spectral shift and first order stretch for this work. Shown in Table 6.4 are the number of subregions that can be used in the NO_2 calibration region (405-450 nm); this can be optimized by comparing the standard deviations for the residuals of the solar spectrum and calibrated reference spectrum for the day of common reference.

WinDOAS was initially applied to all measured spectra from the Eureka 2000 field campaign. O_3 and NO_2 DSCDs were retrieved and converted to VCDs using the AMFs calculated by the RT model (Chapter 8). The mean O_3 VCD, shown in Figure 6.4, retrieved by WinDOAS compares with mean O_3 VCD from the existing DOAS retrieval code within the nominal $\pm 5\%$ measurement errors. Another point to mention is that WinDOAS retrieval of O_3 columns was possible for day 55 (February 24, 2000), two days after polar sunrise at Eureka, however the poor quality of the twilight spectra combined with the less accurate wavelength calibration process in the existing DOAS prevented the retrieval of O_3 VCDs for the same day with this code.

Applying the WinDOAS algorithm to spectra in the NO_2 region, 405-450 nm, resulted in the retrieval of 11 more twilight DSCDs during the 2000 field campaign compared to the existing DOAS results because of the more accurate wavelength calibration process and the wavelength-dependent slit function parameter in WinDOAS. Figure 6.5 shows the complete time series of the retrieved NO_2 VCDs from UT GBS measurements during winter/spring 2000 at ASTRO. DOAS-WinDOAS comparisons for NO_2 columns were more challenging for the first part of the campaign, soon after the polar sunrise at Eureka (day 55 to 62). During this period the NO_2 levels are low; thus the less precise wavelength calibration process in the existing DOAS code resulted in poor quality spectral fits, which did not capture the NO_2 DSCDs accurately. In Figure 6.5, the mean NO_2 VCD resulting from the traditional DOAS compare with the WinDOAS mean NO_2 VCD within the nominal $\pm 12\%$ measurement errors.

6.3.3 O_3 and NO_2 Total Columns

O_3 and NO_2 AMF calculations were done using the RT model (described in Chapter 8). O_3 VCDs were derived using Langley plots in the SZA range 80º to 92º. To derive NO_2 VCDs at twilight, an average RCD was estimated for the day of the reference spectrum using pseudo-Langley plots for all days of measurements (refer to Chapter 5). Then using
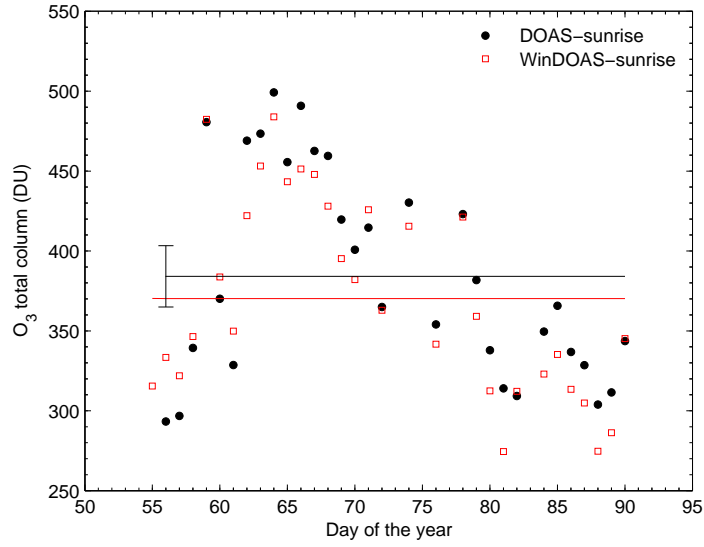
(a)
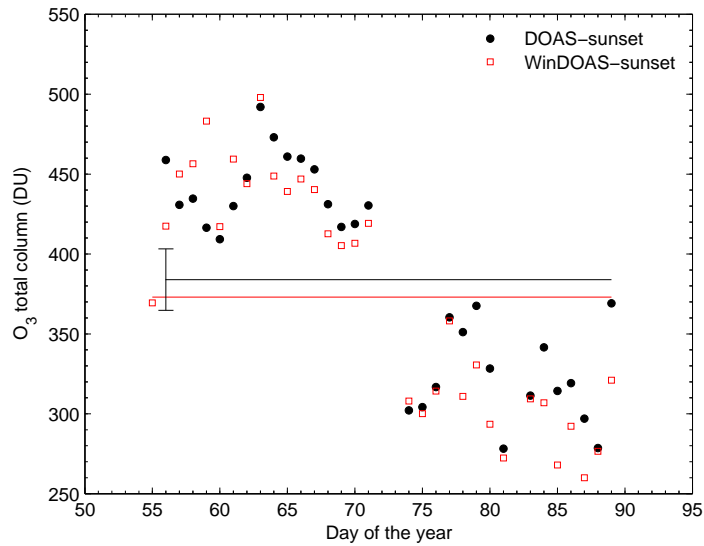
(b)

Figure 6.4: The retrieved O$_3$ VCDs for UT GBS zenith-sky measurements for sunrise (top panel) and sunset (bottom panel) during winter/spring 2000 at Eureka, comparing DOAS and WinDOAS. The black solid lines show the mean O$_3$ VCD from DOAS and the red lines are the WinDOAS mean O$_3$ VCD; the error bar indicates $\pm 5\%$.
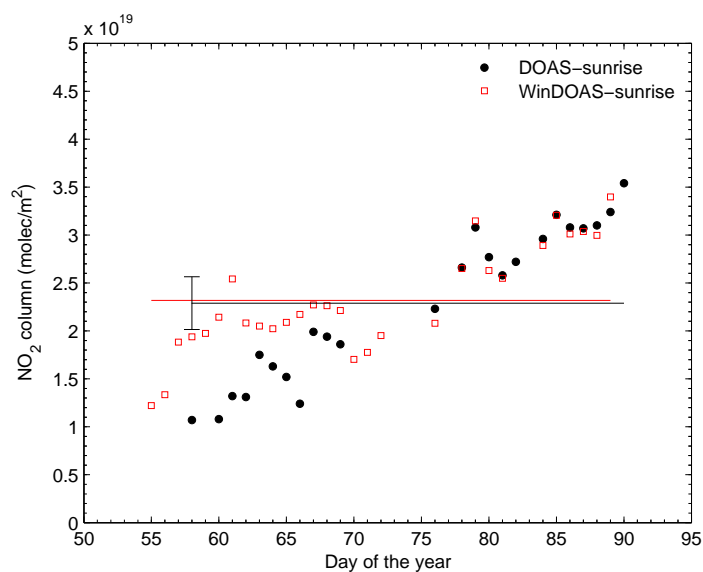
(a)
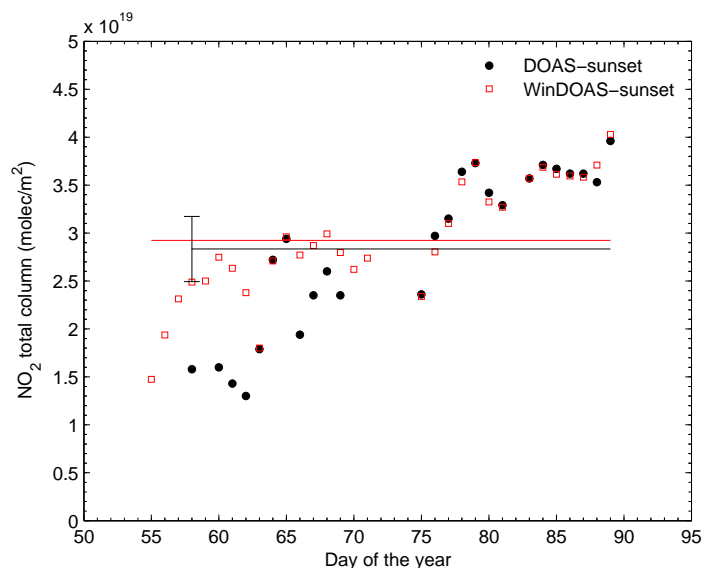
(b)

Figure 6.5: The retrieved NO$_2$ VCDs for UT GBS zenith-sky measurements for sunrise (top panel) and sunset (bottom panel) during winter/spring 2000 at Eureka, comparing DOAS and WinDOAS. The black solid lines show the mean NO$_2$ VCD from DOAS and the red lines are the WinDOAS mean NO$_2$ VCD; the error bar indicates $\pm12\%$.

Equation 2.22, NO_2 VCDs were derived for SZA 90º during both sunrise and sunset.

95 days of O_3 DSCDs and VCDs were derived from UT GBS measurements using Langley plots from March 1999 to April 2003. NO_2 DSCDs and VCDs were retrieved during 1999, 2000 and 2003 resulting in a total of 112 twilight measurements: 50 sunrise and 62 sunset. During 2001, due to a mechanical problem, a slit width smaller than 200 μm could not be used; therefore the spectra quality was poor for the NO_2 retrieval. The total error for UT GBS O_3 and NO_2 measurements was estimated from the root-sum-square of individual errors. These errors are summarized in Table 6.5.

6.3.4 OClO Slant Columns

A novel measurement at AStrO was that of chlorine dioxide (OClO) DSCDs during winter/spring 2000 using UT GBS zenith-scattered twilight spectra. The zenith-sky spectra were recorded using the 1800 grooves/mm grating by swapping between this grating and the 600 grooves/mm grating from day 55 to 89 during the cold winter of 2000. These spectra were used for retrieval of OClO DSCDs in the wavelength region 365 to 390 nm where OClO absorption features are located. Figure 6.6 shows the OClO measured and fitted differential optical depth and its residual for sunrise SZA 90º on day 88 (March 28, 2000). OClO DSCDs were derived at sunrise and sunset for the period of observation and are presented in Figure 6.7. The OClO slant column values are consistent with values reported in the Arctic ($\sim 2.5 \times 10^{14}$ molec/cm^2) by other studies (*Kühl et al.*, 2004).

6.4 Other Measurements

Data from two other ground-based instruments at AStrO, the MSC FTS and DU AERI-X, were provided by H. Fast and P. Fogal, respectively. J. Hannigan and T. Blumenstock provided HNO_3 vertical columns from FTSs located at two other Arctic NDSC sites:

Error	O_3	NO_2	Source
Random noise	1%	2%	Statistically calculated from measurements
Instrument error	3%	3%	Informed estimate
Pseudo-random errors	1-2%	4-6%	Derived from measurements
Absolute cross sections	2.6%	2.3%	*Burrows et al.* (1999a, 1998), respectively
Temperature dependence of the NO_2 cross section	-	$\leq 8\%$	*Pfeilsticker et al.* (1999b)
Uncertainty in NO_2 RCD	-	3-7%	Derived from measurements
AMF error	3%	5-7%	Calculated for the RT model, *Bassford et al.* (2001)
Filling in of absorption by Raman scattering	1%	5%	*Fish and Jones* (1995); *Pfeilsticker et al.* (1999b)
Total RMS error	±5-6%	±12-15%	

Table 6.5: Sources of error and error estimates for the UT GBS O_3 and NO_2 columns.
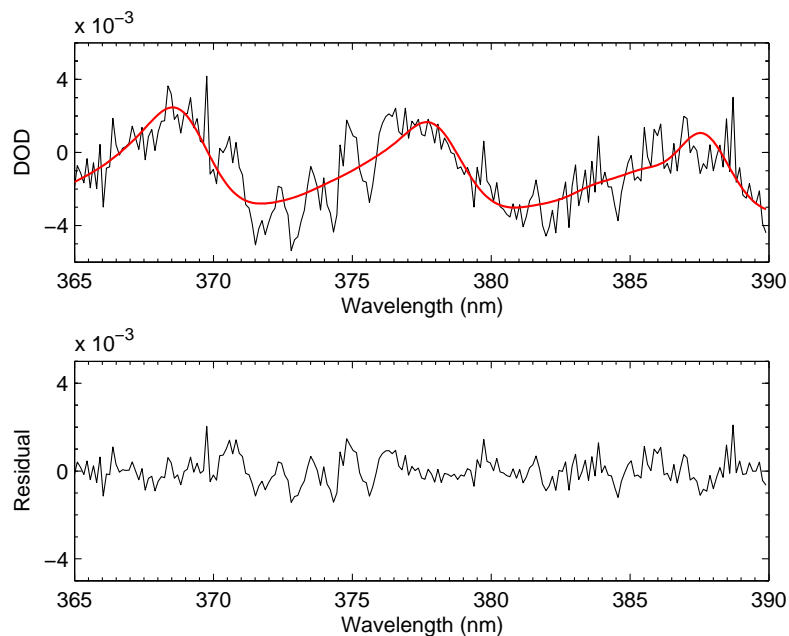
Figure 6.6: DODs for OClO at 90º SZA for UT GBS zenith-sky measurements during 2000 made on day 88 (March 28, 2000), sunrise at Eureka.
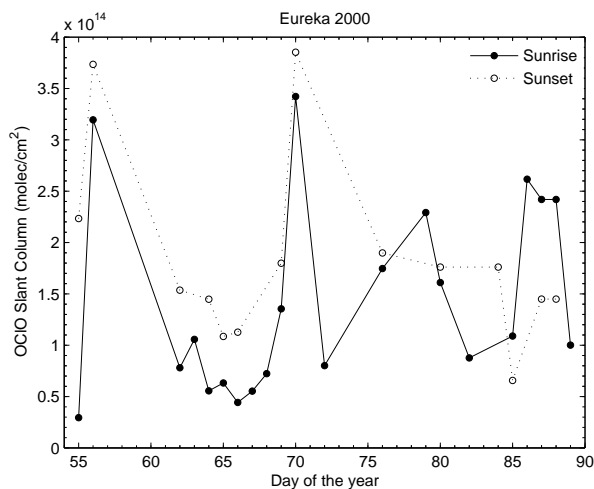
Figure 6.7: The OClO DSCDs during winter/spring 2000.

Thule, Greenland (76.5°N, 68.8°W) and Kiruna, Sweden (67.8°N, 20.4°E), respectively. GOME NO_2 total columns for ASTRO overpasses were provided by A. Richter and ozonesonde data for Eureka was provided by R. Mittermeier. Ozonesonde measurements typically have errors of 3-6% (*Smit*, 1996).

6.4.1 MSC Fourier Transform Spectrometer

The MSC FTS spectrometer at ASTRO is a Bomem DA8 FTS with resolution of 0.004 cm^{-1}, which has been operational since 1993. It records solar absorption spectra in the wavelength range 715 to 4000 cm^{-1} (*Donovan et al.*, 1997). It has MCT and InSb detectors with six interference filters. Each FTS spectrum is a coaddition of four interferograms over 700 s from which total columns of HF, CH_4, N_2O, O_3, HCl, NO, NO_2, $ClONO_2$, HNO_3, CFC-11, ClO, and COF_2 are retrieved using the SFIT1 spectral fitting routine (*Rinsland et al.*, 1982, 1988). A mean daily vertical column was calculated from the individual column measurements for different species at ASTRO from two or more spectra recorded each day or night. Error estimates for the retrieved columns were determined according to the method described by *Murphy et al.* (2001), to account for instrument effects, choice of algorithm, micro-windows, line parameters, a-priori volume mixing ratio profiles, and uncertainty in the temperature profile. Added in quadrature, this resulted in a total of ±9.8% for O_3, ±8.5% for CH_4, ±7.9% for N_2O, ±10.9% for HF, ±13.6% for HNO_3, ±10.3% for NO, ±22.9% for NO_2, and ±36.1% for $ClONO_2$.

6.4.2 The Atmospheric Emission Radiometric Interferometer

The Atmospheric Emission Radiometric Interfrometer (AERI-X) is a Michelson-type interferometer with a maximum path difference of 10 cm which uses a liquid-N_2-cooled MCT detector that covers the spectral region from 650 to 1250 cm^{-1}. Each AERI-X spectrum is a coaddition of 25 interferograms over 1200 s. After spectra were recorded, the University of Denver line-by-line, layer-by-layer spectral modeling code, known as

RADCO, was used to retrieve total columns of CH_4, N_2O, O_3, HNO_3 and CFC-12. RADCO calculates absolute emission spectra based on a model atmosphere which is built using pressure-temperature values from a radiosonde flight done at ASTRO. It includes the species of interest and important interfering species such as CO_2 and H_2O, where the H_2O profile is also derived from the radiosonde. HNO_3 column amounts were retrieved for the period of fall 1994 to spring 1996 (*Olson et al.*, 1996). Error estimates on retrieved HNO_3 total columns are about $\pm 14\%$ which includes the error in the forward model, absolute calibration and the pointing errors (personal communication, P. Fogal).

6.4.3 Thule FTS Measurements

The Thule measurements were obtained from spectra recorded with a 250-cm Optical Path Difference (OPD) Bruker 120M FTS operated by NCAR. The instrument underwent a blind intercomparison with three other FTSs, the NPL Bruker 120M, the Jet Propulsion Laboratory ATMOS (Atmospheric Trace Molecule Spectroscopy experiment) and Mark IV instruments (*Goldman et al.*, 1999), prior to installation at Thule in 1999. Currently the autonomously operated Thule FTS spectrometer records data for $\sim 30\%$ of available days between February 21 and October 20. In the winter of 2001-2002, Thule HNO_3 measurements were carried out from the end of February to the end of April 2002, using only the Sun as light source. The data for the period shown here were analyzed using the SFIT2 v3.82 program which uses a semi-empirical optimal estimation algorithm (*Rodgers*, 1976) to perform a point-by-point fitting of the observed spectra with a 41-layer, line-by-line spectral forward model calculation (*Chang and Shaw*, 1977; *Hase et al.*, 2004). Total column amounts are the integrated retrieved HNO_3 vertical profiles.

6.4.4 Kiruna FTS Measurements

FTS observations have been made at the Swedish Institute of Space Physics in Kiruna since March 1996 within the framework of the NDSC (*Blumenstock et al.*, 2003) in col-

laboration with IMK Karlsruhe, IRF Kiruna and the University of Nagoya. Infrared solar absorption spectra are recorded with a Bruker 120 HR FTS allowing a maximum optical path difference of 360 cm, equivalent to a spectral resolution of up to 0.0025 cm^{-1}. Typically, a spectral resolution of 0.005 cm^{-1} is used. Spectra are coadded for up to 15 minutes during noon and 5 minutes during sunrise and sunset in order to limit the variation of the SZA to 0.2°. An NDSC side-by-side intercomparison was performed in March 1998 (*Meier et al.*, 2005) and the differences were found to be less than 3% for all compared species. For the winter of 2001-2002, Kiruna reported only solar measurements of HNO_3, during October and November in 2001 and again starting from polar sunrise in January 2002 until the end of April. The Kiruna FTS spectra were analyzed with the inversion program PROFFIT (PROFile FIT) (*Hase*, 2000; *Hase et al.*, 2004) using the forward model KOPRA (Karlsruhe Optimized Precise Radiative transfer Algorithm) (*Höpfner et al.*, 1998; *Kuntz et al.*, 1998). The precision error for the Kiruna data is 2.5%.

Chapter 7

Comparison with Atmospheric Models

In this chapter, the first comparisons of the Canadian Middle Atmosphere Model (CMAM) chemical fields with ground-based observations in the polar regions are discussed, together with the first comparisons of SLIMCAT model calculations with trace gas measurements made at ASTRO. As CMAM is a chemistry-climate model, its years do not correspond to any particular year and the comparison must be statistical in nature. CMAM vertical columns for O_3, NO_2 during twilight, HNO_3, NO_x, partial NO_y, N_2O, and CH_4 were calculated from CMAM chemical fields. Both models were compared with DU AERI-X HNO_3 vertical columns for fall 1994 and 1995 as well as spring 1995 and 1996. CMAM and SLIMCAT HNO_3 vertical columns were compared with MSC FTS observations during spring 1999-2003. Also, during 2001-2002, the MSC FTS was used to conduct its first lunar observations, from which HNO_3 vertical columns were retrieved. These lunar observations were combined with solar observations for fall 2001 and spring 2002 at AS-TRO, and were compared with HNO_3 vertical columns measured at Thule and Kiruna. CMAM HNO_3 vertical columns at the closest grid point to Eureka and Kiruna were compared with observations at these two sites, while SLIMCAT HNO_3 vertical columns at

Eureka, Thule and Kiruna were compared with observations made at these three Arctic sites. Comparisons between the vertical columns of atmospheric long-lived tracers HF, CH_4, and N_2O measured by the MSC FTS during 1999-2003 at AStrO and the two models are also discussed.

7.1 Model Descriptions

Two atmospheric models were used for comparison with the Arctic measurements: the Canadian Middle Atmosphere Model (CMAM), which is a General Circulation Model (GCM), and SLIMCAT, which is an off-line Chemical Transport Model (CTM).

7.1.1 Canadian Middle Atmosphere Model

The CMAM is an upward extension of the Canadian Centre for Climate modeling and analysis (CCCma) spectral GCM up to 0.0006 hPa (roughly 100 km altitude), described in detail by *Beagley et al.* (1997). CMAM incorporates radiation, interactive chemistry, gravity wave drag, as well as all the processes in the GCM. CMAM has prognostic variables computed in spectral space using T32 resolution (corresponding to resolution of about 6° in latitude and longitude) and 65 vertical levels (about 2 km vertical resolution in the middle atmosphere). The model has a comprehensive representation of stratospheric chemistry (*de Grandpré et al.*, 2000). A recent comparison of CMAM with other chemistry-climate models is provided in *Austin et al.* (2003).

During this work, I compared chemical fields from two different versions of CMAM with Arctic observations. The first version, a run in climatological mode, is known as the WMO version or version 5. This version also contains a chemical module to account for heterogeneous reactions that occur on supercooled ternary solutions (STS) and water ice PSCs in polar regions, without sedimentation. However during this CMAM run, temperatures at the closest grid point to Eureka were not low enough for the heterogeneous

module to be activated. CMAM WMO vertical profiles of chemical species were provided every 3 days at 0:00 Z, over 20 years at the closest grid point to Eureka (80.3ºN, 84.4ºW). The second version, known as version 7, was also a run in climatological mode. This version does not account for heterogeneous reactions and has no PSCs. The CMAM v.7 vertical profiles of chemical species were provided at every time step (approximately 10 minutes) over 20 years at the closest grid points to Eureka (80.3ºN, 84.4ºW) and Kiruna (69.2ºN, 22.5ºE). To compare the output of both CMAM versions with the measured columns of O_3, NO_2, HNO_3, CH_4, and N_2O as well as active nitrogen (NO_x=NO+NO_2) and partial NO_y (NO_x+HNO_3+$ClONO_2$), mean columns of the species of interest were generated from CMAM profiles at the closest grid point to Eureka and also to Kiruna for HNO_3. CMAM v.7 outputs profiles of chemical species at every timestep, resulting in 144 profiles per day. These profiles were interpolated to a common altitude grid and averaged to obtain daily mean profiles. Daily columns come from integrating these daily mean profiles. Mean columns for a given day resulted from averaging daily columns over 20 years of the CMAM v.7 run, and 1σ represents the inter-annual variability in the model. The inter-annual variability in CMAM v.7 is generally an underestimate of the real variability because there is no quasi-biennial oscillation (QBO), solar variability, or aerosol variability in this run. Also, CMAM v.7 adopts climatological sea-surface temperatures (SSTs) which vary from month-to-month, however they stay the same for each year of the model's run.

7.1.2   SLIMCAT

SLIMCAT is an off-line 3D CTM which has been widely used in previous studies of the stratosphere (*Chipperfield*, 1999). The model has a detailed treatment of stratospheric chemistry. The model temperatures and horizontal winds are specified from analyses and the vertical transport in the stratosphere is diagnosed from radiative heating rates. In the stratosphere, the model uses an isentropic coordinate and this has been extended

down to the surface (*Chipperfield*, 2006).

In the SLIMCAT runs shown here, the model was integrated with a horizontal resolution of 7.5°×7.5°. Run 317 and 323 had 24 levels extending from the surface to about 55 km, run 311 extended from 9 to 55 km. The model was forced by ECMWF analyses and the simulation started on 1/1/1977. Above 350 K, vertical advection was calculated from heating rates diagnosed using the CCMRAD scheme, run 317 was a test run for run 323 to see the effects of using updated heating rates below 350 K (*Chipperfield*, 2006). *Feng et al.* (2005) showed that using this radiation scheme gave a better simulation of vertical transport (i.e. more descent) than the previously used MIDRAD scheme (run 311). This improved the modeled polar O_3 loss. Below 350 K, vertical motion is calculated from the forcing analyses and the troposphere is assumed to be well-mixed.

In the SLIMCAT runs 311, 317 and 323, the model halogen loading was specified from observed tropospheric CH_3Br and halon loadings (*WMO*, 2003) with an additional 6 pptv contribution assumed from short-lived bromine sources. Accordingly, the stratospheric bromine loading around 2000 was around 21 pptv. In run 336, two extra tracers for bromine source gases were included and the bromine was split between the three gases (personal communication with M. Chipperfield). Photochemical data was generally taken from *Sander et al.* (2003), except for some details related to polar Cl_2O_2 chemistry (*Feng et al.*, 2005). Output from the run was saved every 2 days at 00:00 Z at the locations of Eureka, Thule and Kiruna.

7.2 Model-Measurements Comparisons

Total columns of O_3, NO_2, HNO_3, HF (only from SLIMCAT), CH_4, N_2O, active nitrogen ($NO_x = NO + NO_2$), and partial NO_y ($NO_x + HNO_3 + ClONO_2$) in two CMAM runs, WMO and v.7, and four SLIMCAT runs, 311, 317, 323 and 336, were compared with observed total columns measured by the UT GBS, MSC FTS and DU AERI-X (only for HNO_3

columns during 1994 to 1996) at AStrO. In this section, the final comparisons with CMAM v.7 and SLIMCAT 323 are presented. Also, specific issues in other runs that were further investigated are discussed. Northern Hemisphere PV maps on 475 and 550 K isentropic surfaces were used to provide more information on the dynamical conditions over different Arctic NDSC sites and/or interesting observational periods where O_3 columns deviated from the climatological mean. PV maps presented in this work are from ECMWF analyses. For the period from 1999 to 2003, analysis maps of PV from the ECMWF daily analyses are used. ECMWF uses a 3D variational analysis at the T106 resolution and 60 levels in the vertical. A description of the data is given in *Fahre Vik* (2003).

7.2.1   Ozone Total Columns

Figure 7.1 shows UT GBS O_3 vertical columns compared with Eureka ozonesonde data, MSC FTS observations, SLIMCAT 323 and CMAM v.7 model calculations. This is the first comparison of CMAM chemical fields with ground-based observations in the polar regions.

During spring 1999, UT GBS O_3 vertical columns compare well with MSC FTS observations, agreeing within the combined measurement errors for all but two days. During the same period, SLIMCAT 323 O_3 columns agree with observations for four days (81-86); however after day 86 (March 27, 1999) SLIMCAT reports higher O_3 columns by as much as 17% although it follows the variability pattern seen in the observations. Generally, CMAM v.7 lacks cold winters and it does not include heterogeneous chemistry, thus warm winters such as 1998-1999 with little PSC formation provide an excellent opportunity to compare CMAM v.7 chemical fields with observations (*Manney et al.*, 1999). Looking at Figure 7.1, it is clear that CMAM v.7 O_3 columns compare well with observed columns from day 91 to 101 (April 1 to 11, 1999). Figure 7.2 shows that the polar vortex is weak thus the higher O_3 columns observed prior to day 91 may originate
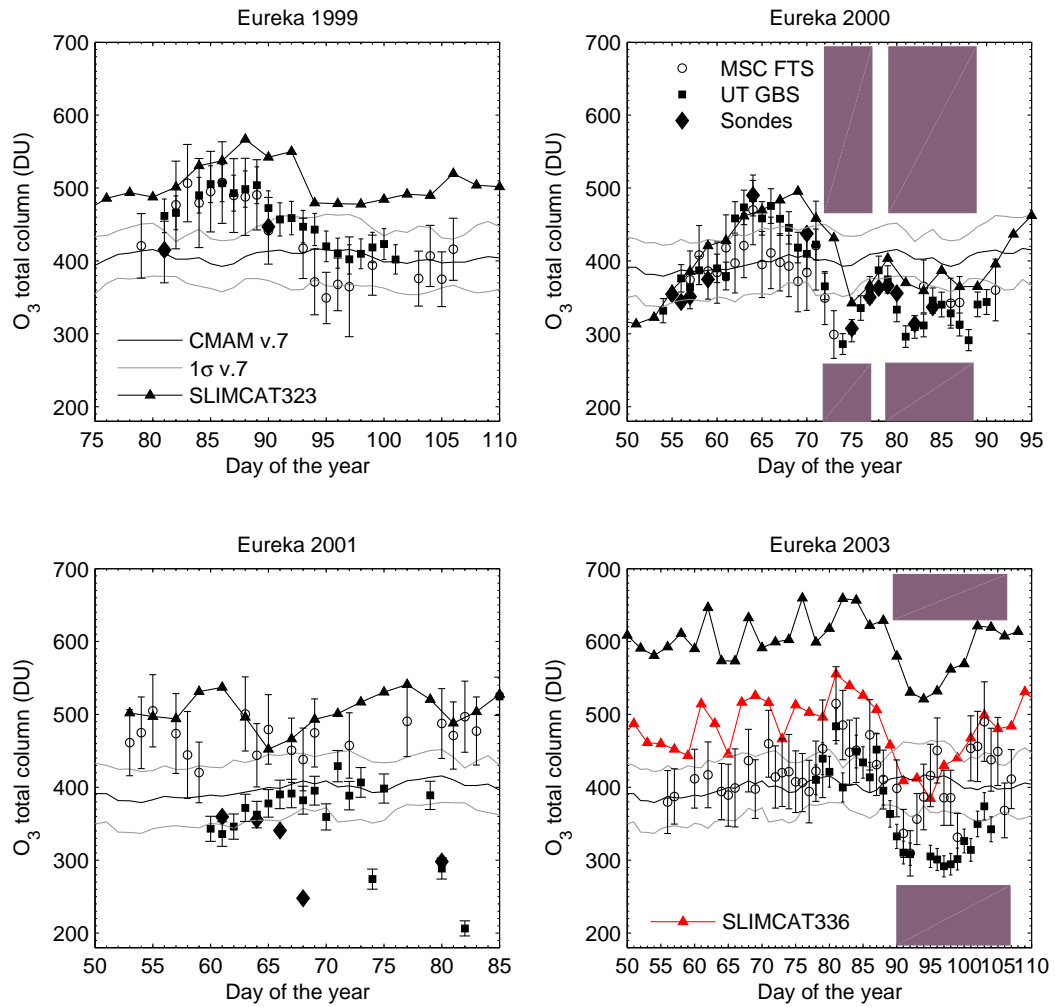
Figure 7.1: O$_3$ total columns during winter/spring 1999, 2000, 2001 and 2003. SLIMCAT 336 O$_3$ columns are only shown for the 2003 field season as SLIMCAT 336 reported similar values to SLIMCAT 323 for other measurement periods. The periods that Eureka was inside the vortex are marked by purple blocks.

(a) 990322-d81 (b) 990323-d82 (c) 990324-d83 (d) 990325-d84

(e) 990326-d85 (f) 990327-d86 (g) 990328-d87 (h) 990329-d88
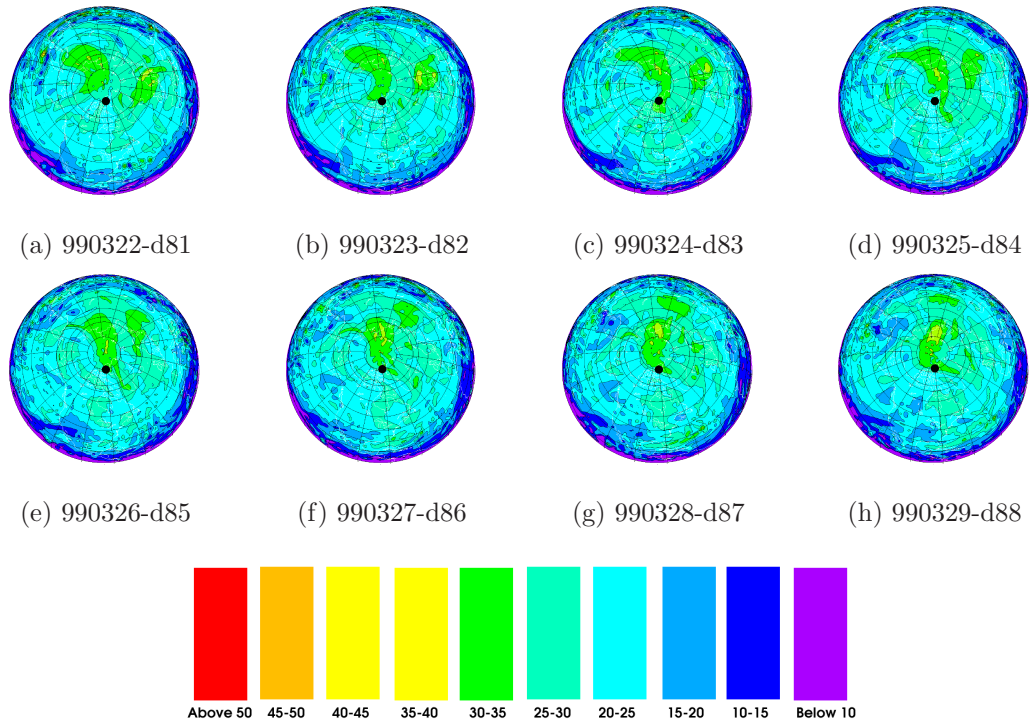
Figure 7.2: ECMWF PV ($\times 10^{-5}$ Km^{2}kg^{-1}s^{-1}) maps of the Northern Hemisphere at 475 K during March 1999. The location of Eureka is marked with a black dot. The polar vortex during 1999 was weak and not much variation is seen in the above PV maps.

from the O$_3$-rich air mass of northern mid-latitudes.

During winter/spring 2000, UT GBS O$_3$ vertical columns again agree with integrated O$_3$ columns from Eureka ozonesondes and MSC FTS observations within measurement errors. The Eureka 2000 field season was the only cold winter among the four winters observed in this work, although there were several exceptionally cold and strong spring-time vortices in the mid-1990s as shown in Figure 7.3 (*Manney et al.*, 2005). ECMWF potential PSC areas at 475 K shown in Figure 7.4 indicate potential for PSC formation at Eureka during February 11-22, 2000 (day 42-53). If we look at integrated sonde and UT GBS values for days 54-57, O$_3$ columns are $\sim$350 DU which is 13% lower than the CMAM climatological mean. Unfortunately, HNO$_3$ observations did not start until day 57 due to the solar illumination and after that day there is no evidence of denitrification
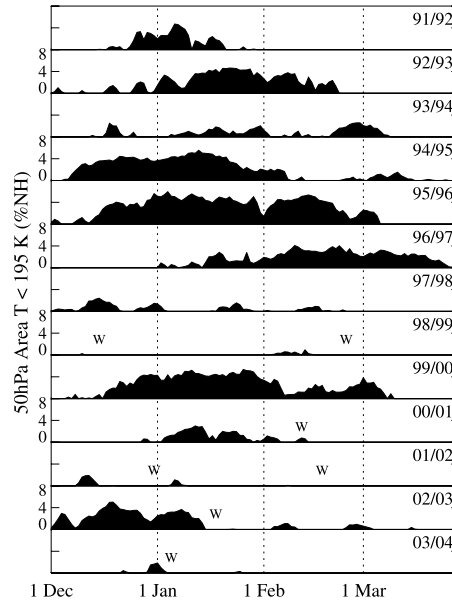
Figure 7.3: Time series of area at 50 hPa with temperatures less than T_{NAT} for 1 December through 31 March in 1991-1992 through 2003-2004 from NCEP/CPC analyses. Dates of major warmings (first day of wind reversal at 60°N) are marked with W's (*Manney et al.*, 2005).

in HNO_3 observations. However measured NO_x columns remained lower than the CMAM climatological mean for much of the season in 2000, which can imply the presence of high amounts of active chlorine.

SLlMCAT 323 O_3 columns are the same as the observations within measurement errors until day 69 (March 9, 2000). After day 72, based on ECMWF PV maps shown in Figure 7.5, the polar vortex is located over Eureka as seen on the 475 K isentropic surface and stays in place until day 77 (March 17, 2000); during this period SLIMCAT 323 does not capture the observed O_3 values, although after day 77, SLIMCAT O_3 columns again agree well with observations temporarily. Based on Figure 7.5, Eureka passes the edge of the vortex and goes inside on day 79 (March 19, 2000) and remains there until day 89 (March 29, 2000). During this period, the observed O_3 columns fall below 300 DU while during the same period, the lowest SLIMCAT 323 O_3 value is ~340 DU. The

differences between SLIMCAT and observed O_3 values while Eureka is experiencing the cold conditions inside the vortex imply unresolved issues with the model's heterogeneous chemistry scheme. As expected, CMAM v.7 does not capture the low O_3 values measured when Eureka was inside the vortex because it does not include PSCs and heterogeneous chemistry.

During winter/spring 2001, MSC FTS O_3 vertical columns on average are ~20% higher than UT GBS measurements, although integrated O_3 columns from ozonesonde data are closer to UT GBS measurements. For the same period, SLIMCAT 323 reports O_3 columns which are on average 20% higher than UT GBS observations, but generally in agreement with MSC FTS measurements within the measurement errors. The 2001 winter/spring was relatively warm, thus the agreement of the CMAM v.7 mean O_3 columns with the UT GBS measured columns shows CMAM v.7 simulates the O_3 column under PSC-free condition well (*Manney et al.*, 2005).

During March 2003, UT GBS O_3 columns are in agreement with MSC FTS columns within measurement errors until April when MSC FTS reports O_3 columns which are ~20% higher than UT GBS measurements. Differences between the MSC FTS O_3 columns and those measured by a number of other instruments have also been observed in several recent Eureka campaigns (*Kerzenmacher et al.*, 2005) and work is in progress to identify the causes of those discrepancies. In Figure 7.1, SLIMCAT O_3 columns from runs 323 and 336 show that both runs capture the observed day-to-day variability. However SLIMCAT 323 O_3 columns are 20-60% higher than the observed values, while SLIMCAT 336 O_3 columns mostly agree with the MSC FTS observed values. Comparison of SLIMCAT 336 O_3 columns with other measurement periods, 1999, 2000 and 2001, produced the same results as SLIMCAT 323. CMAM climatological O_3 columns are in agreement with the UT GBS and MSC FTS measurements during February and March 2003 before the O_3-depleted air typical of the isolated cold vortex air masses moves over Eureka as is shown in Figure 7.6. Eureka was located first at the edge of the vortex on day 91 (April

(a) 000211-day 42

(b) 000212-d43

(c) 000213-d44

(d) 000214-d45

(e) 000215-d46

(f) 000216-d47

(g) 000217-d48

(h) 000218-d49

(i) 000219-d50

(j) 000220-d51

(k) 000221-d52

(l) 000222-d53
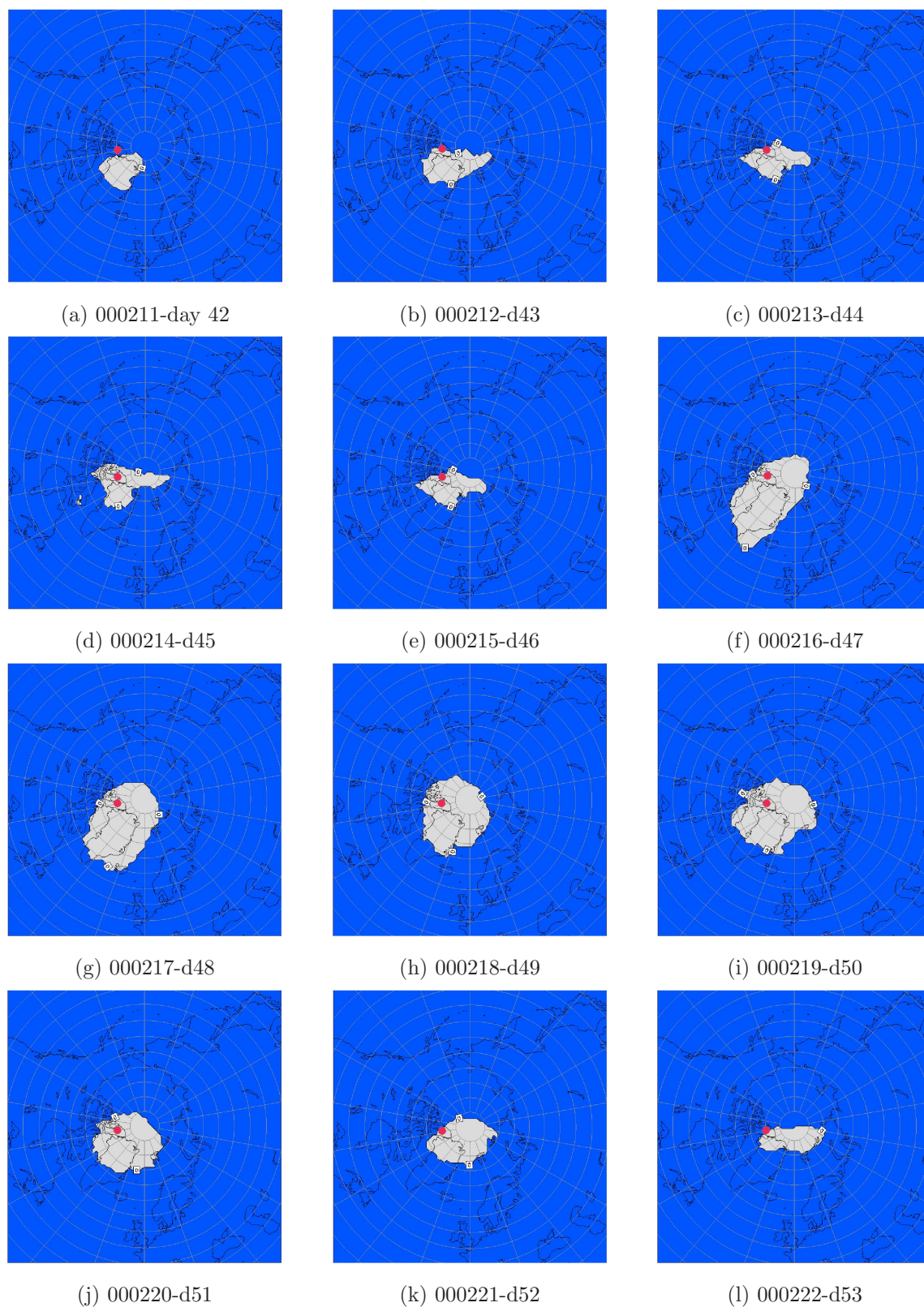
Figure 7.4: ECMWF maps of potential PSC areas in the Northern Hemisphere at 475 K during February 2000. The location of Eureka is marked with a red dot.

(a) 000312-d72   (b) 000313-d73   (c) 000314-d74   (d) 000315-d75

(e) 000316-d76   (f) 000317-d77   (g) 000319-d79   (h) 000320-d80

(i) 000321-d81   (j) 000322-d82   (k) 000323-d83   (l) 000324-d84

(m) 000325-d85   (n) 000326-d86   (o) 000327-d87   (p) 000328-d88

(q) 000329-d89
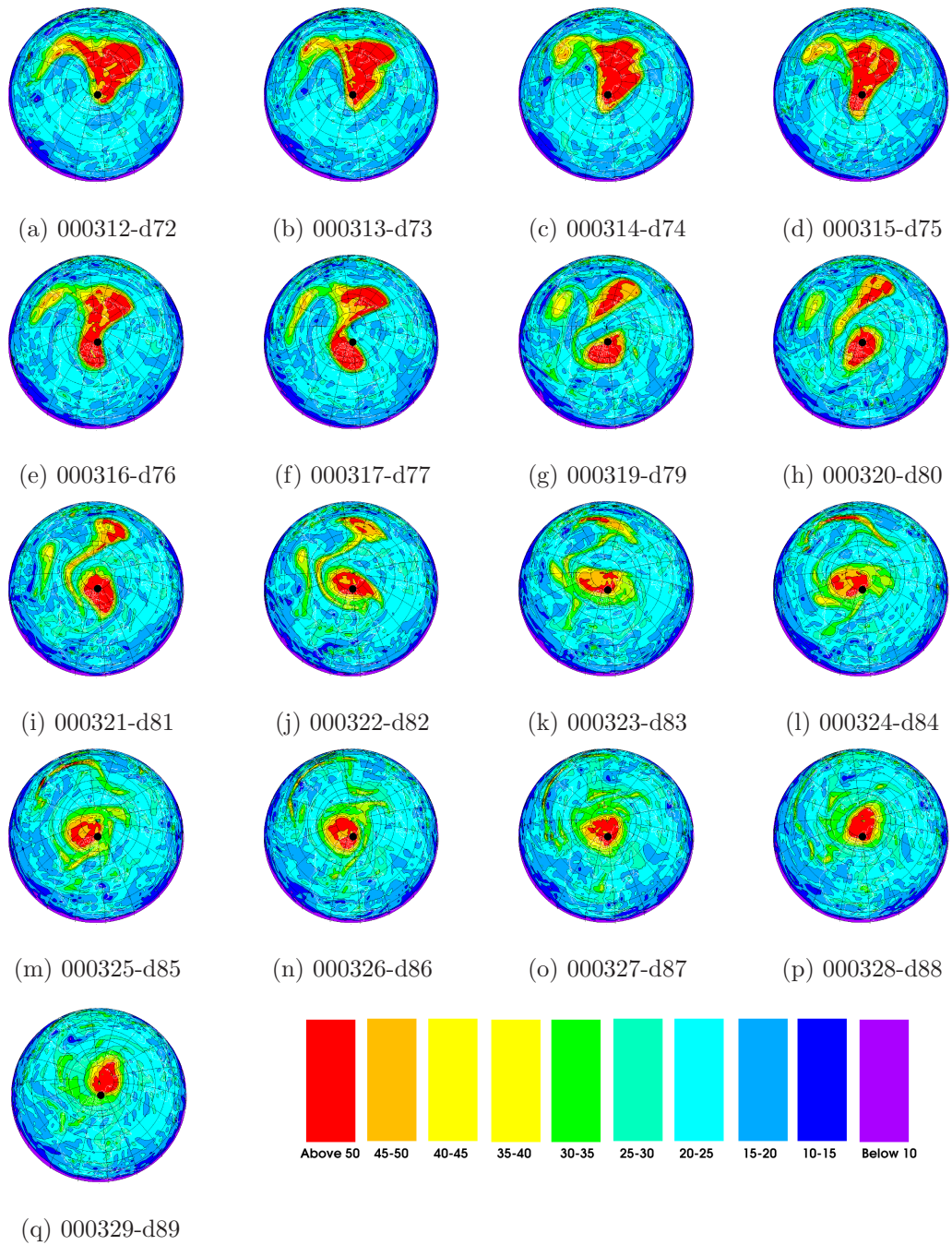
Figure 7.5: ECMWF PV ($\times 10^{-5}$ Km^{2}kg^{-1}s^{-1}) maps of the Northern Hemisphere at 475 K during March 2000. The location of Eureka is marked with a black dot.

1, 2003) and then inside the vortex until day 107 (April 18, 2003) when the final warming caused the breakdown of the vortex shown in Figure 7.6.

Ozone Vertical Profiles

SLIMCAT 311 O_3 columns were too high ($\geq$700 DU) compared to UT GBS observations during winter/spring 2000, which led to comparison of SLIMCAT O_3 vertical profiles with coincident ozonesonde profiles. Figures 7.7 and 7.8 show comparison with 18 coincident days of sonde measurements in January, February and March 2000.

Comparing SLIMCAT 311 O_3 profiles with sondes in the altitude range of 5-10 km, the upper troposphere-lower stratosphere region revealed an excess O_3 value up to 1 ppmv in SLIMCAT for all 18 days of comparison. In the following run, SLIMCAT 317, this issue was solved and comparison with the same sonde profiles resulted in excellent agreement in the upper troposphere-lower stratosphere. The issue in SLIMCAT 311 was the way the model treated the lowermost stratosphere. The SLIMCAT 311 heating rates from MIDRAD were too high in the lowermost stratosphere, the levels between the tropopause and the 380 K isentropic surface; thus O_3 values near 380 K were transported downward too quickly.

CMAM v.7 O_3 profiles with 1σ interannual variability are also shown in Figures 7.7 and 7.8, which indicate that CMAM v.7 O_3 peaks at a lower altitude and the peak itself is broader in altitude compared to SLIMCAT and what is suggested by observations, although during this period the sondes did not get high enough to capture the O_3 peak. Generally, the CMAM v.7 O_3 vertical profiles compares with sonde profiles within 1σ CMAM variability.

Another set of O_3 vertical profile comparison was conducted for January, February and March 2000, using sonde data during testing SLIMCAT runs using different heating rates. Figures 7.9 and 7.10 show the comparison between SLIMCAT 323, which had an offset of 1 day compared to previous runs and used the CCMRAD scheme for heating

(a) 030401-d91   (b) 030402-d92   (c) 030403-d93   (d) 030404-d94

(e) 030405-d95   (f) 030406-d96   (g) 030410-d100   (h) 030411-d101

(i) 030412-d102   (j) 030413-d103   (k) 030414-d104   (l) 030415-d105

(m) 030416-d106   (n) 030417-d107   (o) 030418-d108
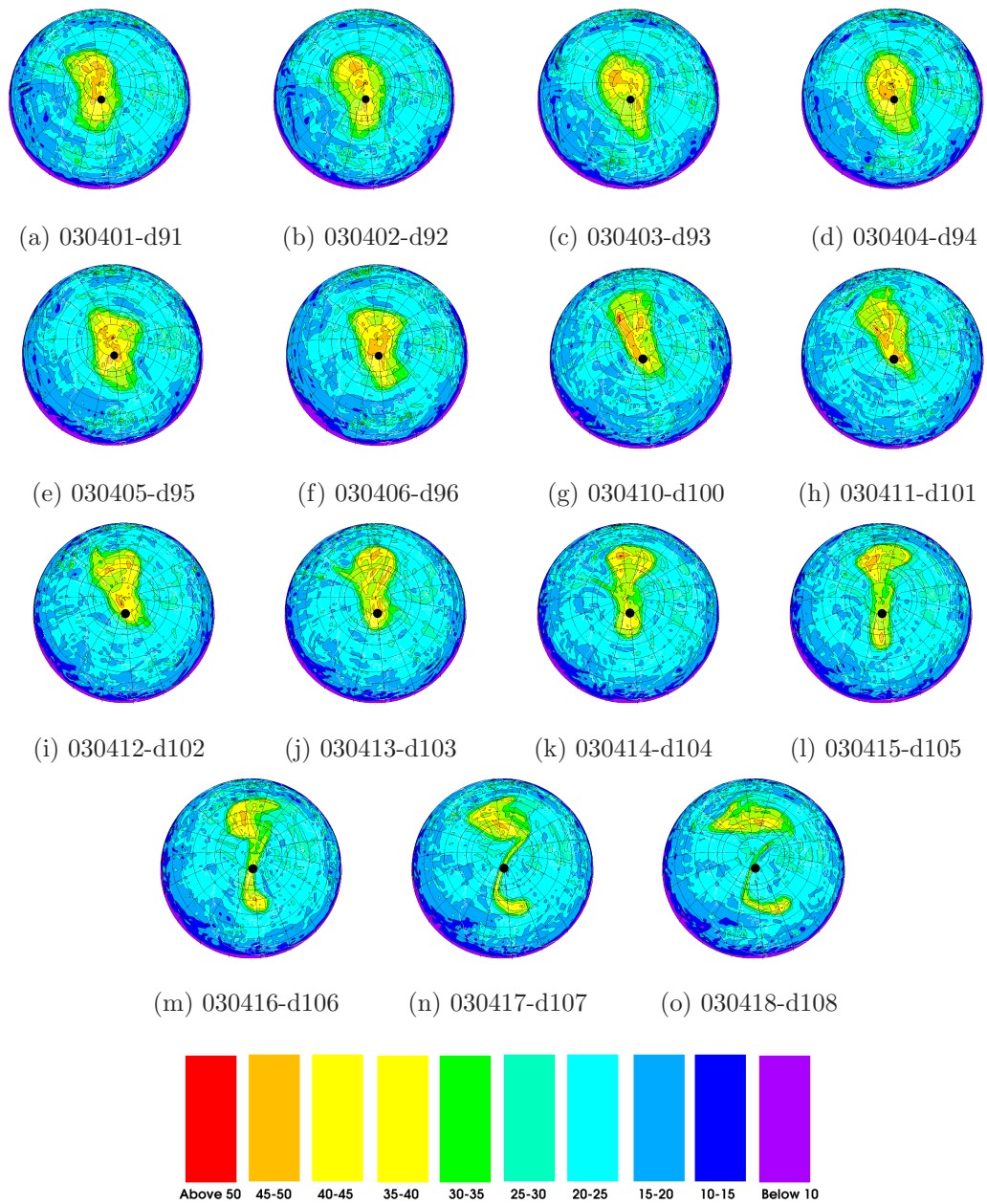
Figure 7.6: ECMWF PV ($\times 10^{-5}$ Km^{2}kg^{-1}s^{-1}) maps of the Northern Hemisphere at 475 K during April 2003. The location of Eureka is marked with a black dot.
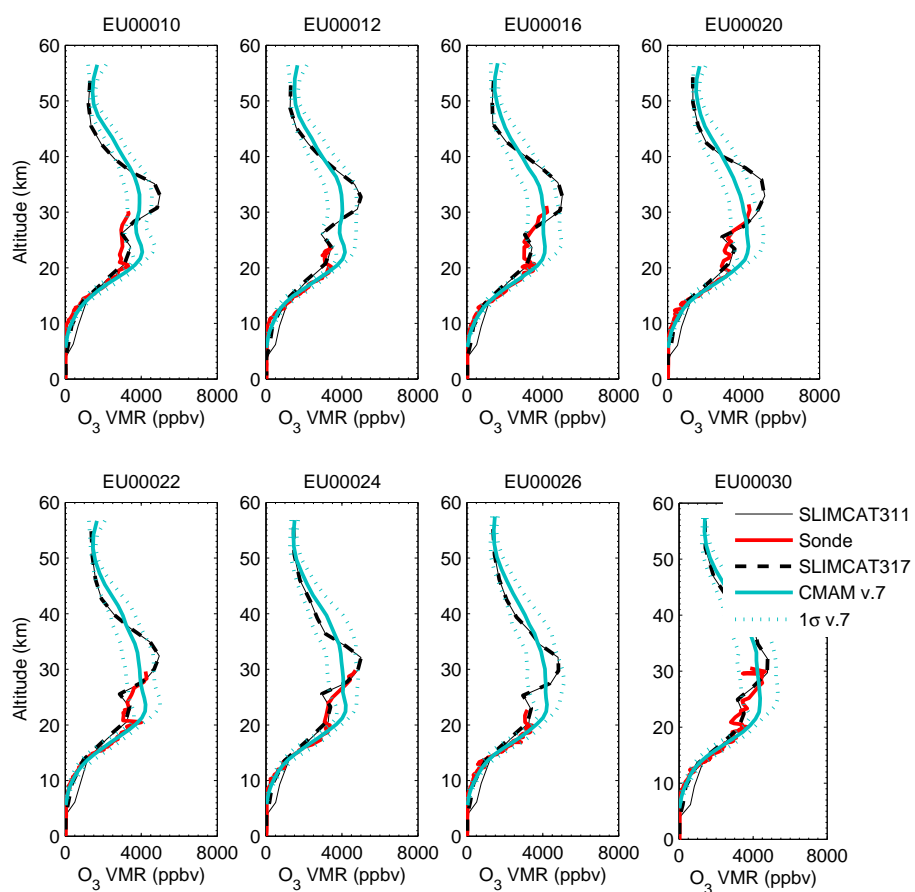
Figure 7.7: O₃ vertical profiles from SLIMCAT 311, 317 and ozonesondes at Eureka during January 2000.
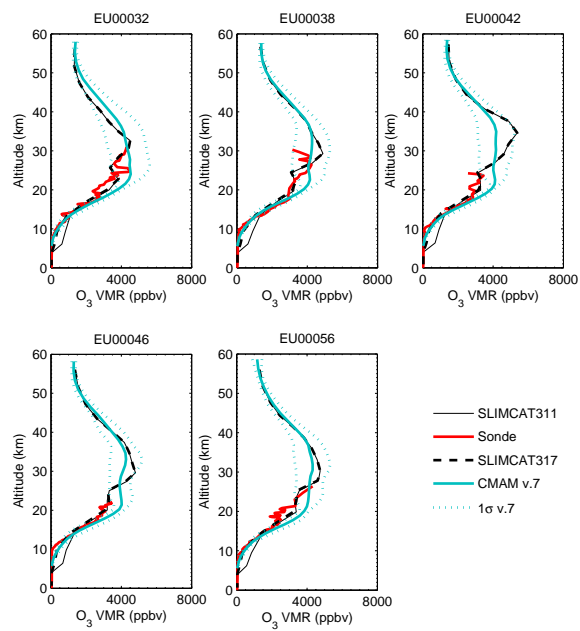
(a) February 2000
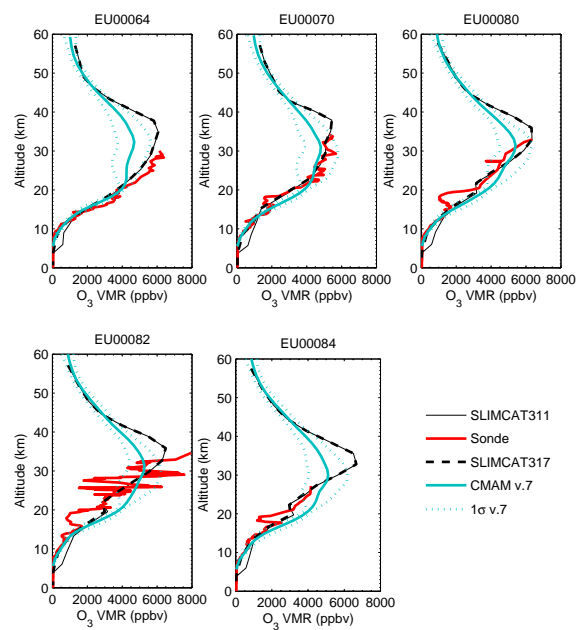
(b) March 2000

Figure 7.8: O₃ vertical profiles from SLIMCAT 311, 317 and ozonesondes at Eureka during February and March 2000.

rate diagnostics, and 17 coincident sonde profiles during winter/spring 2000. For this period, SLIMCAT 323 O_3 profiles are within 25% of the sonde values at the peak of O_3 volume mixing ratio. This improvement in transport affected O_3 vertical profiles as well as other chemical profiles, depending on their vertical gradient in this region.

7.2.2 Nitrogen Species

NO_2 and NO_x Columns

Figure 7.11 shows UT GBS NO_2 columns for 1999 and 2000 for sunrise and sunset along with NO_2 columns from MSC FTS and GOME. The MSC FTS measured daily NO_2 columns by averaging over two or more measured values during the day. Comparison with the MSC FTS was possible during February and at the beginning of March as MSC FTS measurements were done in the SZA range of 85º to 89º, which was close in time to the UT GBS twilight measurements. However later in the season, the MSC FTS measured at higher SZA. As expected, the daytime NO_2 columns measured by the MSC FTS are smaller than the twilight values, consistent with the diurnal cycle shown in Figure 5.9.

GOME columns in Figure 7.11 are from the GOME overpasses within 200 km of Eureka resulted from PGlobal V6.8 (personal communication with A. Richter). Retrieved NO_2 DSCDs for GOME were done using a reference spectrum taken for each equatorial crossing. A constant slant column of 4.0×10^{15} molec/cm^2 was added to the retrieved SCDs. Then the VCDs were determined with AMFs calculated using climatology (Richter, 2003). The ERS-2 satellite overpasses Eureka at 10:30 a.m. local time, with SZAs in the range 72º-89º. The comparison was not straightforward due to the fact that the columns retrieved from ground-based measurements are at lower SZA than the GOME columns. The comparison with GOME was further complicated by NO_2 twilight chemistry as GOME measured at a different SZA each day. Another complicating issue
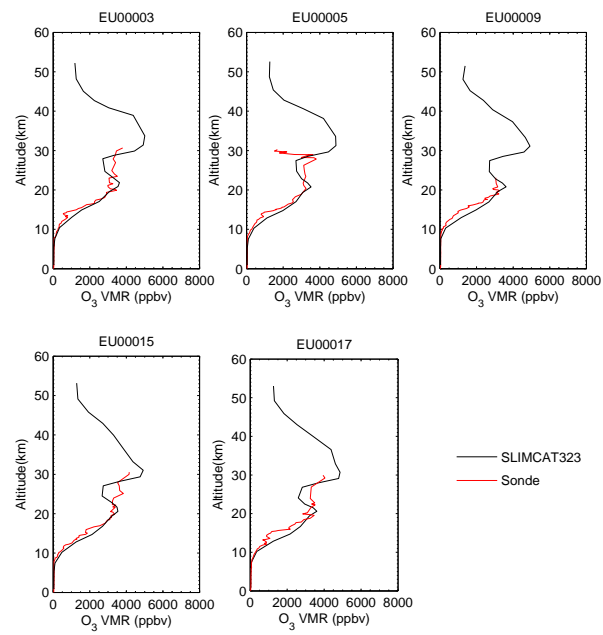
(a) January 2000
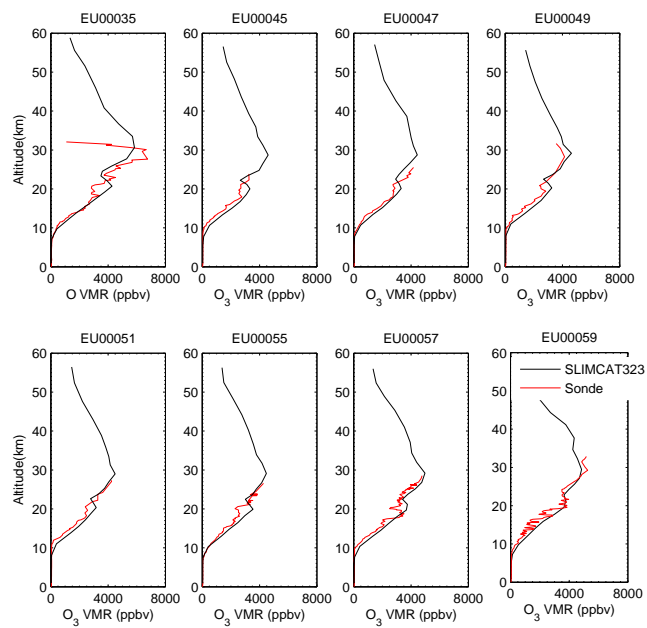
(b) February 2000

Figure 7.9: O$_3$ vertical profiles from SLIMCAT 323 and ozonesondes at Eureka during January and February 2000.
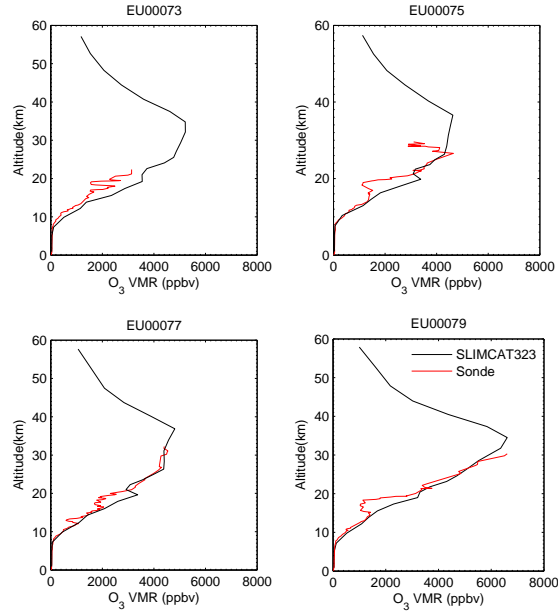
Figure 7.10: O$_3$ vertical profiles from SLIMCAT 323 and ozonesondes at Eureka during March 2000.

was that the stratospheric column changed as the polar vortex passed over Eureka twice during 2000.

To compare UT GBS NO$_2$ VCDs during twilight with CMAM v.7, modeled NO$_2$ profiles were interpolated to SZA 90° during sunrise and sunset then integrated and averaged over 20 years of CMAM v.7, which resulted in the modeled NO$_2$ twilight columns shown in Figure 7.11. CMAM v.7 climatological NO$_2$ columns at twilight agree with observed UT GBS twilight columns within CMAM v.7 1σ variability during 1999; however during the cold year of 2000, the UT GBS twilight columns are mostly higher than CMAM v.7 up to the last week of March ($\sim$day 80).

There were 42 coincident days of SLIMCAT 323 NO$_2$ twilight columns (columns at closest SZA to 90° during both sunrise and sunset) which were compared with UT GBS twilight columns during winter/spring 1999 and 2000. The SLIMCAT 323 NO$_2$ and UT GBS twilight columns are in excellent agreement during spring 1999. During
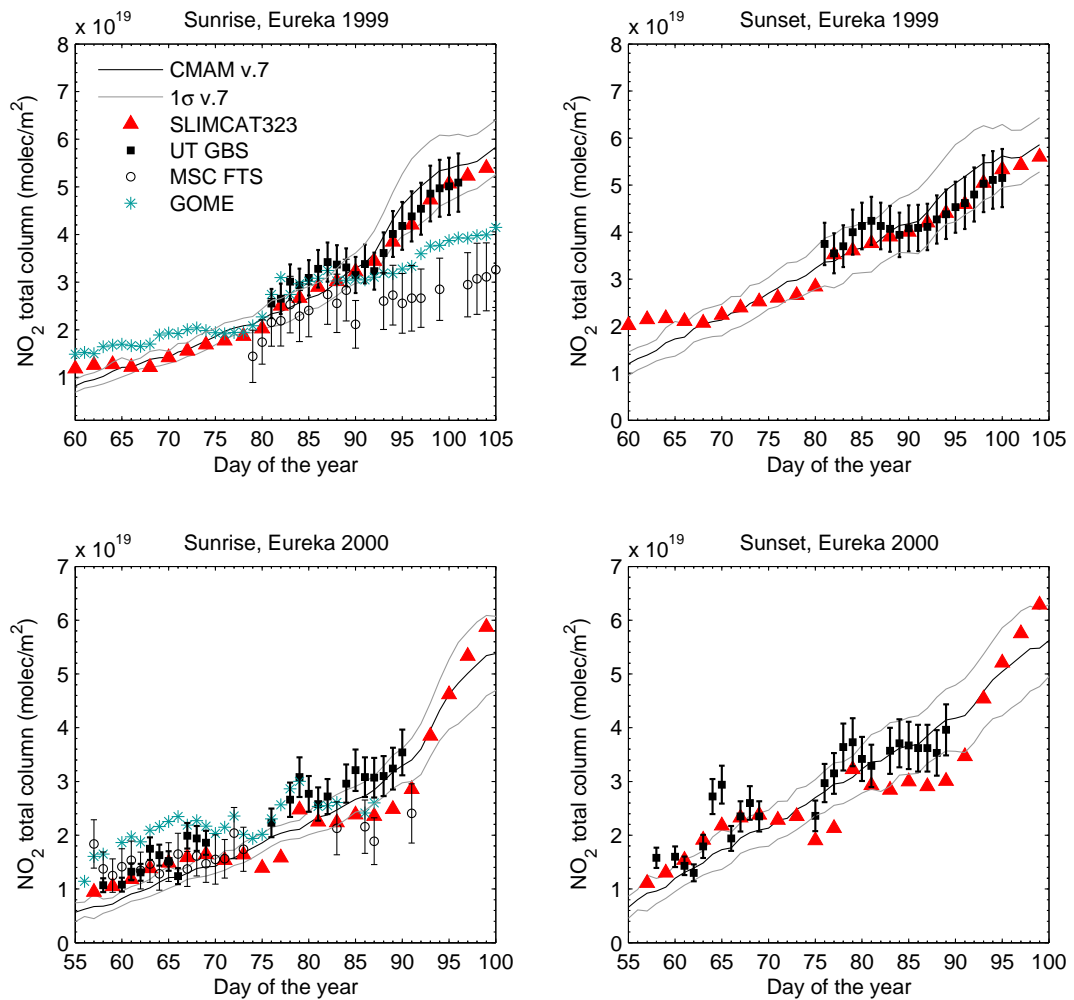
Figure 7.11: NO₂ total columns during sunrise and sunset for winter/spring 1999 and 2000 at Eureka. GOME and MSC FTS measurements are plotted with UT GBS sunrise measurements as they are closer in time to these measurements.

winter/spring 2000, SLIMCAT 323 agrees with UT GBS measured columns within the measurement errors to day 70 (except sunset column on day 66); however after this period SLIMCAT reports lower NO_2 twilight columns. Eureka was experiencing the extreme cold stratospheric temperatures and chemical conditions typical of inside the vortex from day 72 to 89 which further complicates the comparison.

The sum of NO and NO_2 columns, NO_x, is expected to remain constant during the day, allowing comparison of climatological NO_x from CMAM v.7 with observed NO_x from the MSC FTS. Figure 7.12 shows the comparison of total daily NO_x for four years of measurements in the Arctic with CMAM v.7. Looking early in the season, at the end of February and beginning of March, modeled NO_x was lower than the observed values by as much as 40%; however by mid-March for years with warm winters (1999, 2001 and 2003) modeled NO_x generally agrees with the observed columns within CMAM 1σ variability. They agree until mid-April when the observed values reached an equilibrium but modeled NO_x continued to increase. During the cold year of 2000, the measured NO_x columns remained low until the beginning of April, possibly indicating denitrifcation.

Partial NO_y Columns

Partial NO_y can be calculated as the sum of $NO+NO_2+HNO_3+ClONO_2$ using MSC FTS measurements during winter/spring 2000, 2001 and 2003. This could not be done for winter/spring 1999 as there was no measurement of $ClONO_2$. These columns were compared with calculated partial NO_y columns from CMAM v.7 shown in Figure 7.13. Generally, CMAM v.7 partial NO_y columns compare with measured values within CMAM 1σ variability.

7.2.3 HNO_3 Vertical Columns

Here, comparison of HNO_3 columns from CMAM v.7 and SLIMCAT 323 with DU AERI-X, are presented for fall to spring 1994-1995 and 1995-1996. In Figure 7.14, it can be seen
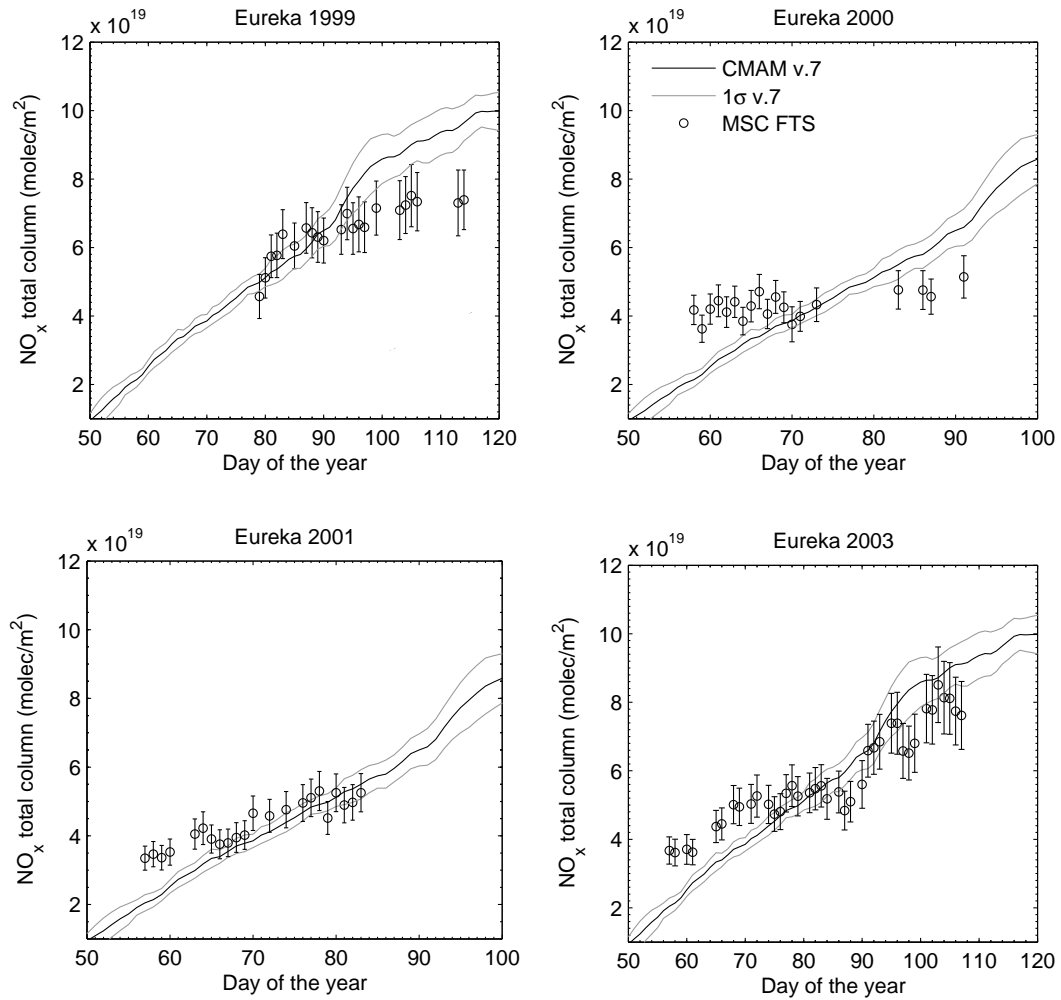
Figure 7.12: NO$_x$ total columns from MSC FTS during winter/spring 1999, 2000, 2001 and 2003 at Eureka compared with CMAM v.7 NO$_x$ columns.
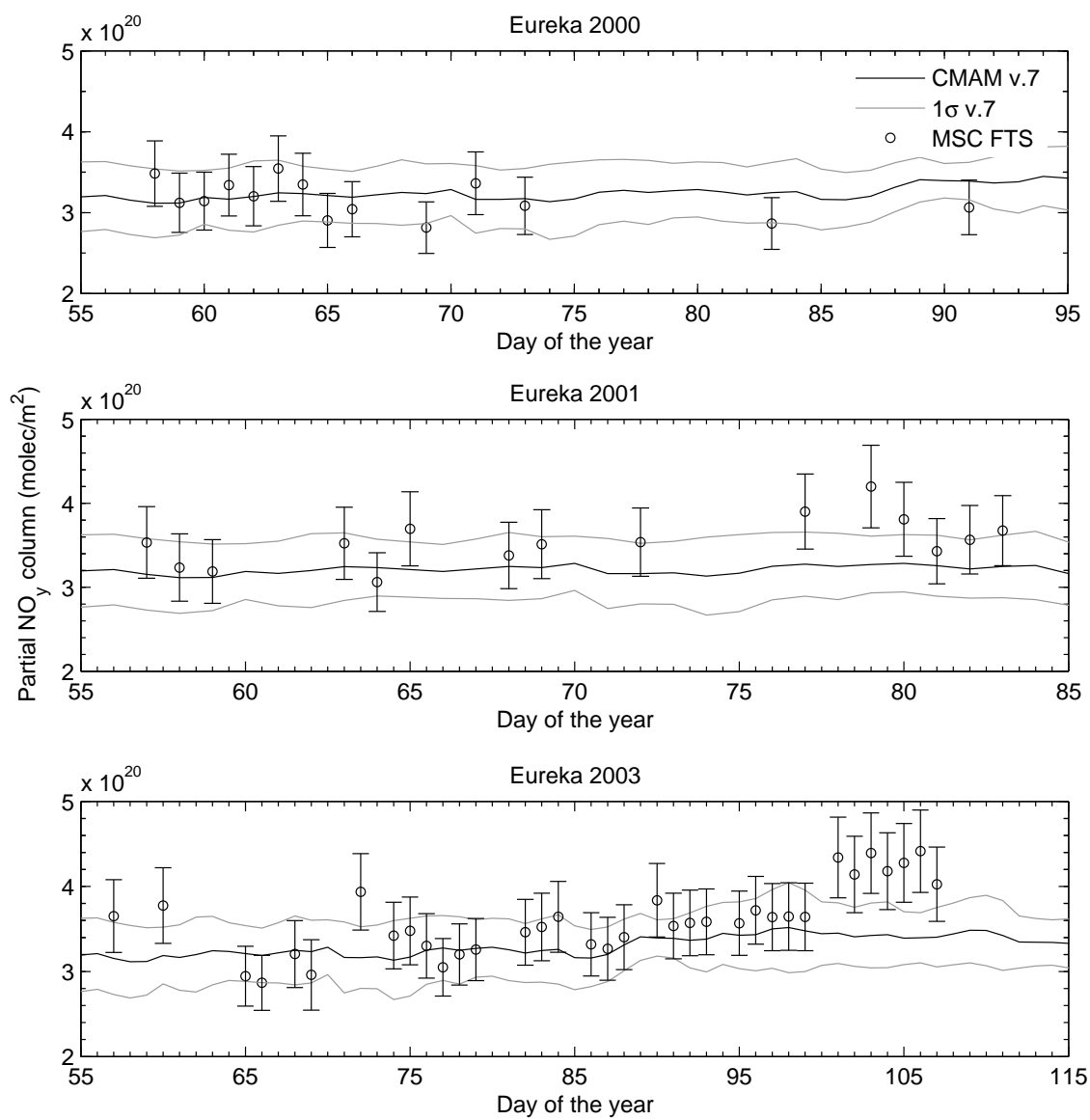
Figure 7.13: Partial NO$_y$ columns during winter/spring 2000, 2001 and 2003 at Eureka compared with CMAM v.7 partial NO$_y$ columns.

that AERI-X observations do not show the seasonal build up of HNO_3, neither in 1994-1995 nor in 1995-1996, possibly indicating PSC formation followed by denitrification. As noted by *Manney et al.* (2005), 1994-1995 and 1995-1996 stand out as unusually cold winters. The average potential for PSC formation in these two winters was very high, as highlighted in Figure 7.3. Therefore the partial agreement with CMAM v.7 is not for the right reason. During both measurement periods SLIMCAT reports significantly lower values than DU AERI-X.

In Figure 7.15, CMAM v.7 mean climatological HNO_3 columns are in agreement with the FTS solar columns during winter/spring 1999, 2001 and 2003; while SLIMCAT 323 HNO_3 columns agree with the observations to better than 12% during winter/spring 1999, 2000 and 2001. During 2003, SLIMCAT 323 HNO_3 is ∼25% higher than the MSC FTS columns. The SLIMCAT comparison for winter/spring 2003 was improved by 12% using the SLIMCAT 336 HNO_3 columns; however the results of comparison using SLIMCAT 336 for other years did not improve the results compared to SLIMCAT 323.

Lunar HNO_3 Observations

Nitric acid (HNO_3) observations during polar night provide valuable information on the processes which condition the polar stratosphere for springtime O_3 depletion. The first FTS measurements of HNO_3 during polar night, using the Moon as the light source, were carried out by Notholt in December 1992 and in February 1993 at the Ny-Alesund Arctic NDSC station (79ºN, 12ºE) (*Notholt et al.*, 1993; *Notholt*, 1994a,b; *Notholt et al.*, 1995, 1997). At Kiruna, lunar FTS spectra have been recorded since the winter of 1994/1995 (*Schreiber et al.*, 1997). In this work, the first measurements of HNO_3 vertical columns at Eureka throughout the polar night using the FTS system with the Moon as the light source are reported. Also, this is the first time that HNO_3 columns measured at the three NDSC Arctic sites, Eureka, Thule and Kiruna, have been intercompared.

These measurements were made in the winter of 2001-2002. The 2001-2002 winter
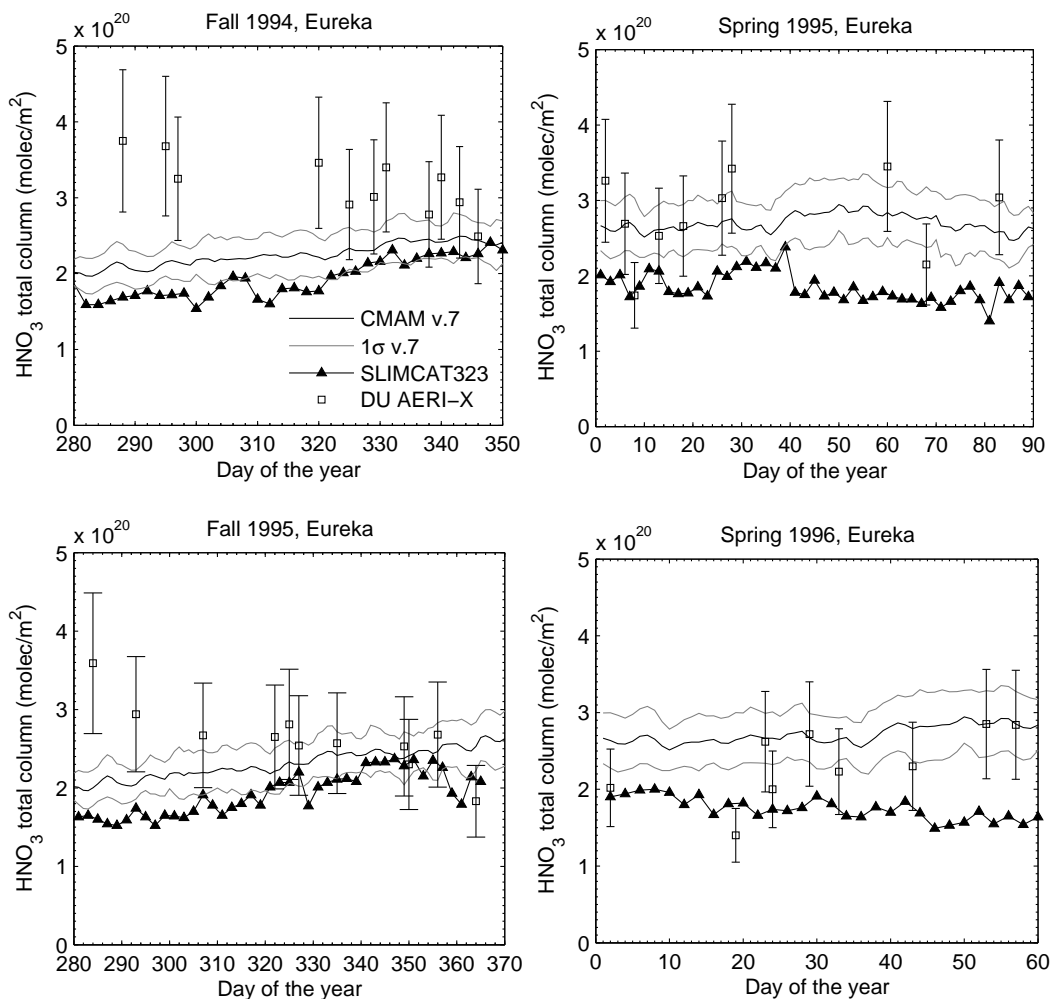
Figure 7.14: The AERI-X HNO$_3$ columns during fall to spring 1994-1995 and 1995-1996 at Eureka compared with CMAM v.7 and SLIMCAT 323.
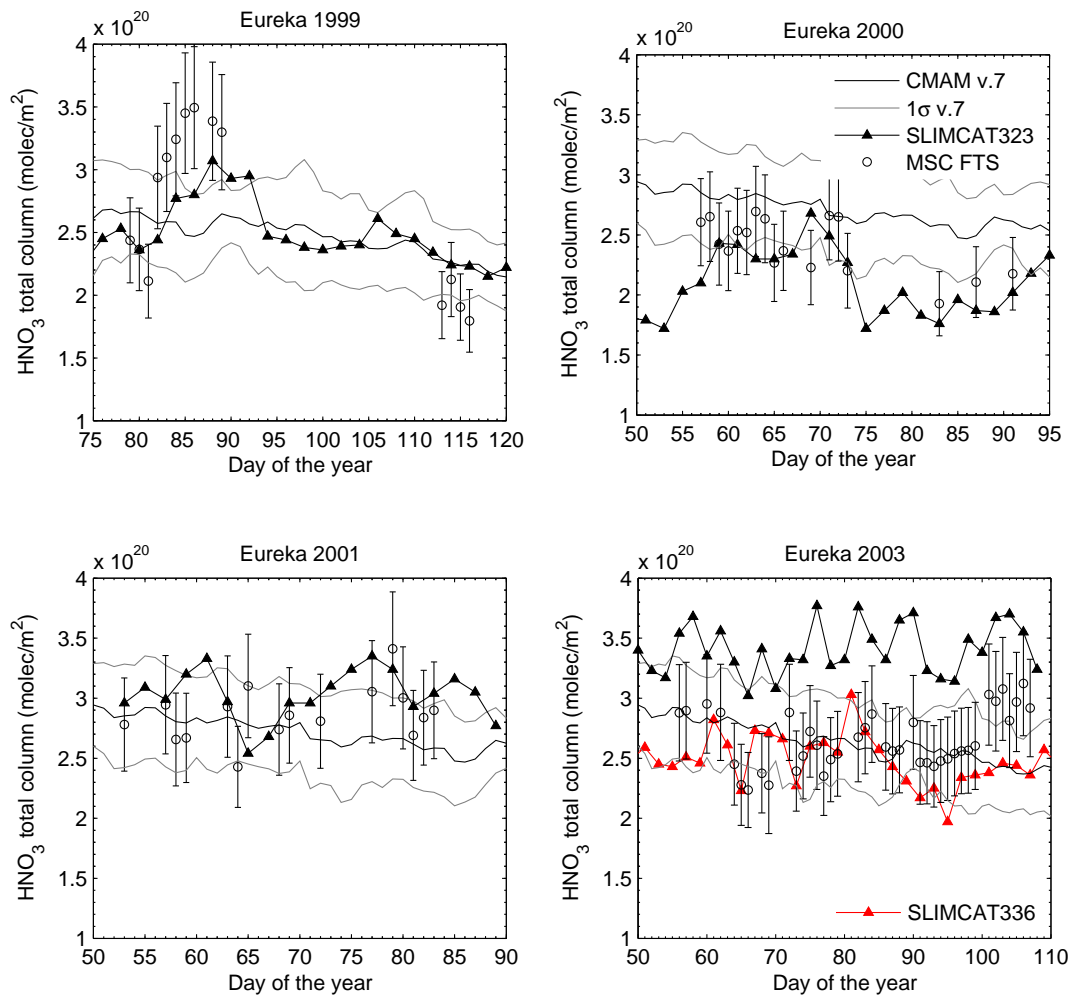
Figure 7.15: HNO₃ columns during winter/spring 1999, 2000, 2001 and 2003 at Eureka compared with CMAM v.7 and SLIMCAT 323.

was relatively warm, with two major stratospheric warmings occurring in December 2001 and February 2002 and with the daily average area for PSCs of near zero throughout the winter as shown in Figure 7.3 (*Manney et al.*, 2005). Thus the meteorological conditions that winter provided an excellent opportunity to compare and test the CMAM v.7 warm climate with observations to see the seasonal build-up of HNO_3 under PSC-free conditions.

The daily mean HNO_3 vertical columns for the three Arctic sites are plotted in Figure 7.16 as a time series from October 2001 to April 2002, while Figure 7.17 shows the close-up view of the spring period. The combined systematic and random error bars for Eureka represent $\pm13.6\%$ of the daily or nightly mean HNO_3 vertical columns added in quadrature to the standard deviation of the individual measurements from the daily or nightly mean. The combined error bars are shown only for Eureka to indicate the total error typical of such FTS measurements. For clarity, the error bars shown for Thule are just the random component of the total error, and the error bars for Kiruna are the 2.5% precision error. In Figure 7.16, it is evident that the HNO_3 columns over Eureka steadily increased from October through to about March 15. Thereafter the HNO_3 columns fluctuated rapidly and were generally decreasing. This is consistent with the HNO_3 winter maximum due to the reduction in HNO_3 photolysis by sunlight and the conversion of NO_x back to N_2O_5 and HNO_3 during periods of darkness, which tends to produce more HNO_3 in winter than in summer (*Wood et al.*, 2004). Also Eureka reports HNO_3 columns between $\sim1.8\times10^{20}$ and $\sim3.5\times10^{20}$ molec/m^2 that are consistent with the winter build up of HNO_3 columns reported by *Notholt et al.* (1997) over Ny-Alesund during the winters of 1992-1995 (also obtained using lunar FTIR spectroscopy).

The March 2002 solar and lunar HNO_3 vertical columns at Eureka generally agree with the Thule solar measurements. This is consistent with ECMWF PV values at 475 K for the same period, shown in Figure 7.16 and Figure 7.17, which indicate that similar dynamical conditions were experienced at these two sites. The observed larger differences
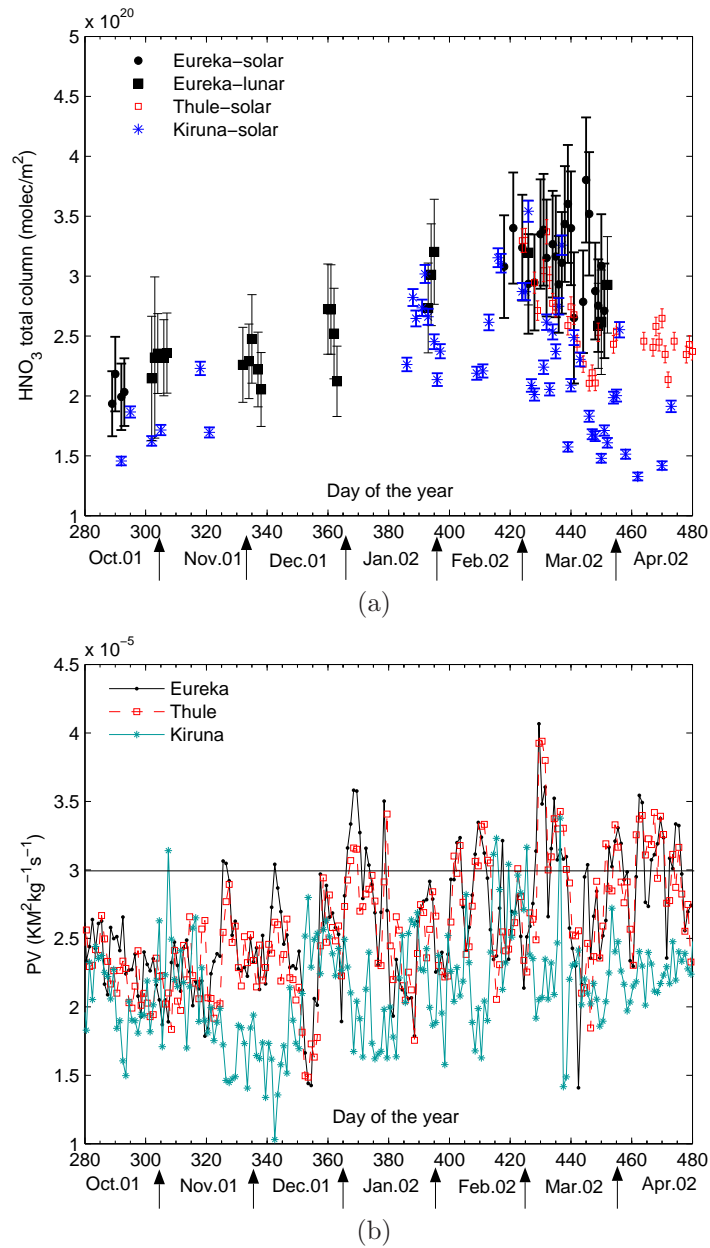
Figure 7.16: Time series of HNO_3 columns (top panel) and ECMWF PV values at 475 K (bottom panel) at three Arctic sites, Eureka, Thule, and Kiruna, from October 2001 to April 2002. The solid line on the bottom plot is at PV=3.0×10^{-5} $Km^2kg^{-1}s^{-1}$ which is an indication of the edge of the vortex (*Nash et al.*, 1996).
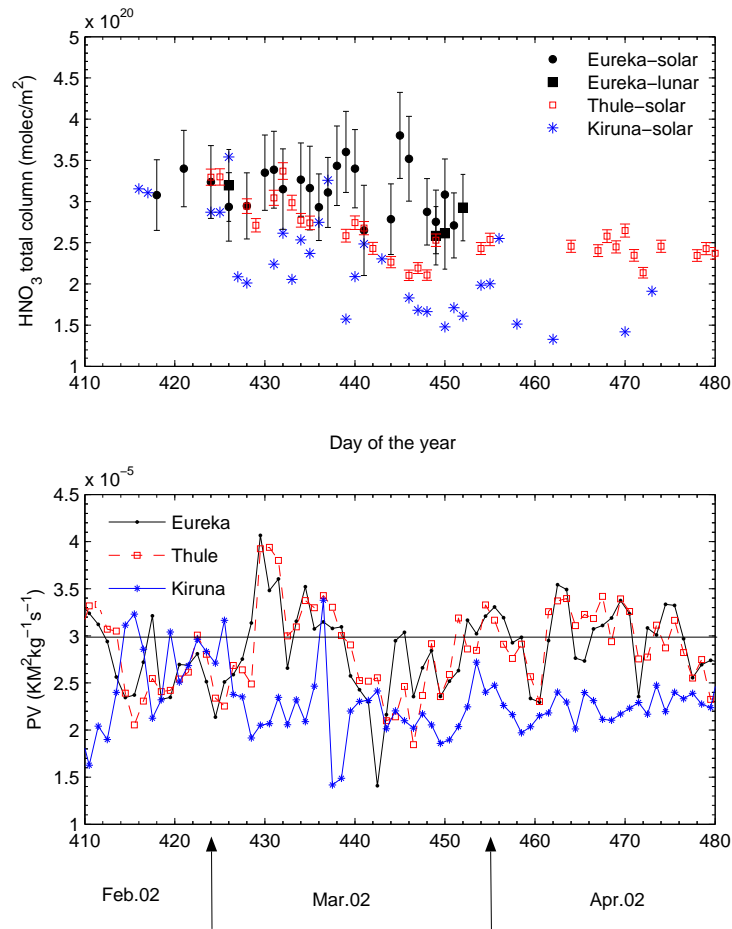
Figure 7.17: Time series of HNO$_3$ columns (top panel) and ECMWF PV values at 475 K (bottom panel) at the three Arctic sites: Eureka, Thule, and Kiruna from February to April 2002.

between Eureka and Thule columns on day 439 (March 15) and day 446 (March 22) 2002, are due to the relative position of the polar vortex based on ECMWF Northern Hemisphere PV maps at 550 K. For example in Figure 7.18, on day 446 (March 22, 2002) Eureka is inside the polar vortex while Thule is at the edge of the vortex so as shown in Figure 7.17, Eureka reports higher PV and higher HNO$_3$ values typical of the HNO$_3$-rich airmass inside the vortex. In contrast, on day 449 (March 25, 2002) both Eureka and Thule are at the edge of the polar vortex, as seen in Figure 7.18, and report similar values for PV and for HNO$_3$.
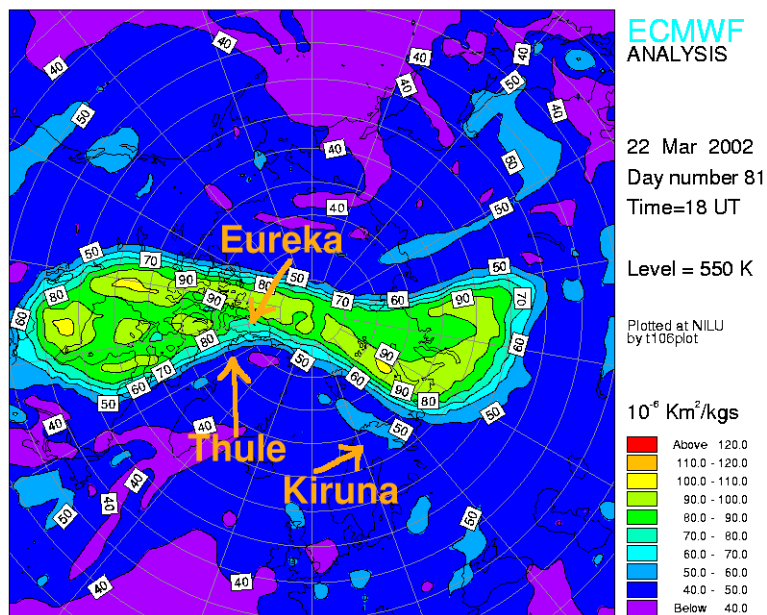
(a) 020322-day 446
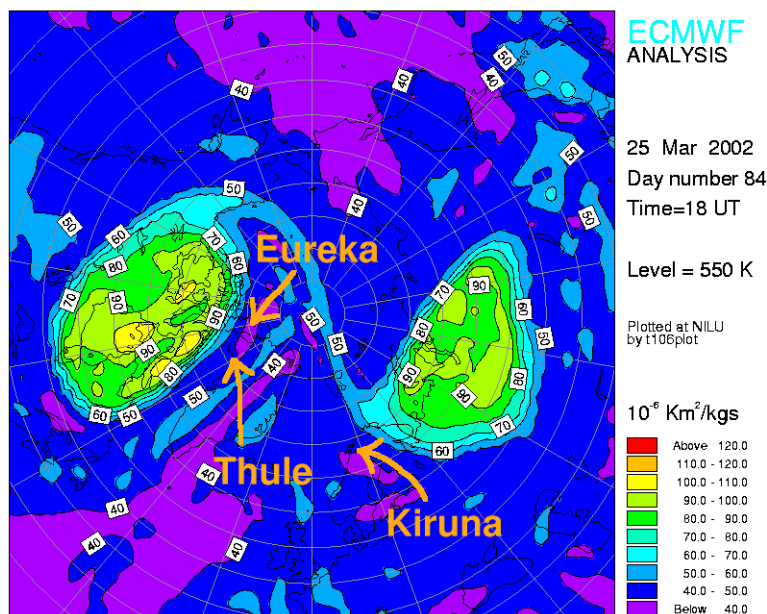
(b) 020325-day 449

Figure 7.18: ECMWF PV maps for Northern Hemisphere at 550 K close to the maximum HNO_3 for March 22 and 25, 2002.

The Kiruna solar HNO_3 vertical columns from October to November 2001 and again from January to April 2002 are consistently lower than those measured at Eureka and Thule. This can be attributed to different dynamical conditions experienced at Kiruna compared to the other two sites and to the greater exposure to sunlight at Kiruna's latitude, which results in more rapid photolysis of HNO_3 to NO_x species.

Figure 7.19 presents CMAM v.7 HNO_3 columns at Eureka and Kiruna. The CMAM climatological HNO_3 columns at the closest grid point to Eureka show excellent agreement with the Eureka lunar measurements through the winter; also the CMAM climatological HNO_3 columns are in agreement with the Eureka solar measurements during fall 2001 and spring 2002 within the inter-annual variability of CMAM. In Figure 7.16, the ECMWF PV time series shows that Eureka and Thule did not stay inside the polar vortex for any extended period while Kiruna rarely experienced vortex conditions during the observation period. Because 2001-2002 was a particularly warm winter, comparisons between the measurements and CMAM allow us to assess how well the model captures the chemistry under PSC-free conditions. The agreement of CMAM v.7 with the observations is consistent with the lack of cold winters in this version of the model and shows the seasonal build up of HNO_3 in the absence of PSCs and denitrification. In Figure 7.19, the SLIMCAT 323 output is also compared with the measured HNO_3 vertical columns at Eureka. Day-to-day comparison of SLIMCAT 323 HNO_3 columns with the lunar and solar columns results in an average difference of 10% for 19 coincident days for Eureka, 20% for 15 coincident days for Thule, and 7% for 30 coincident days for Kiruna. SLIMCAT 323 generally reports higher columns than the CMAM climatological mean.

The CMAM climatological HNO_3 columns at the closest grid point to Kiruna were compared with solar HNO_3 values measured at Kiruna, also shown in Figure 7.19. The CMAM climatological HNO_3 columns are consistent with the measured values at Kiruna: 33 out of 51 days are within 1σ variability, even allowing or the fact that the Kiruna measurements do not include systematic errors.
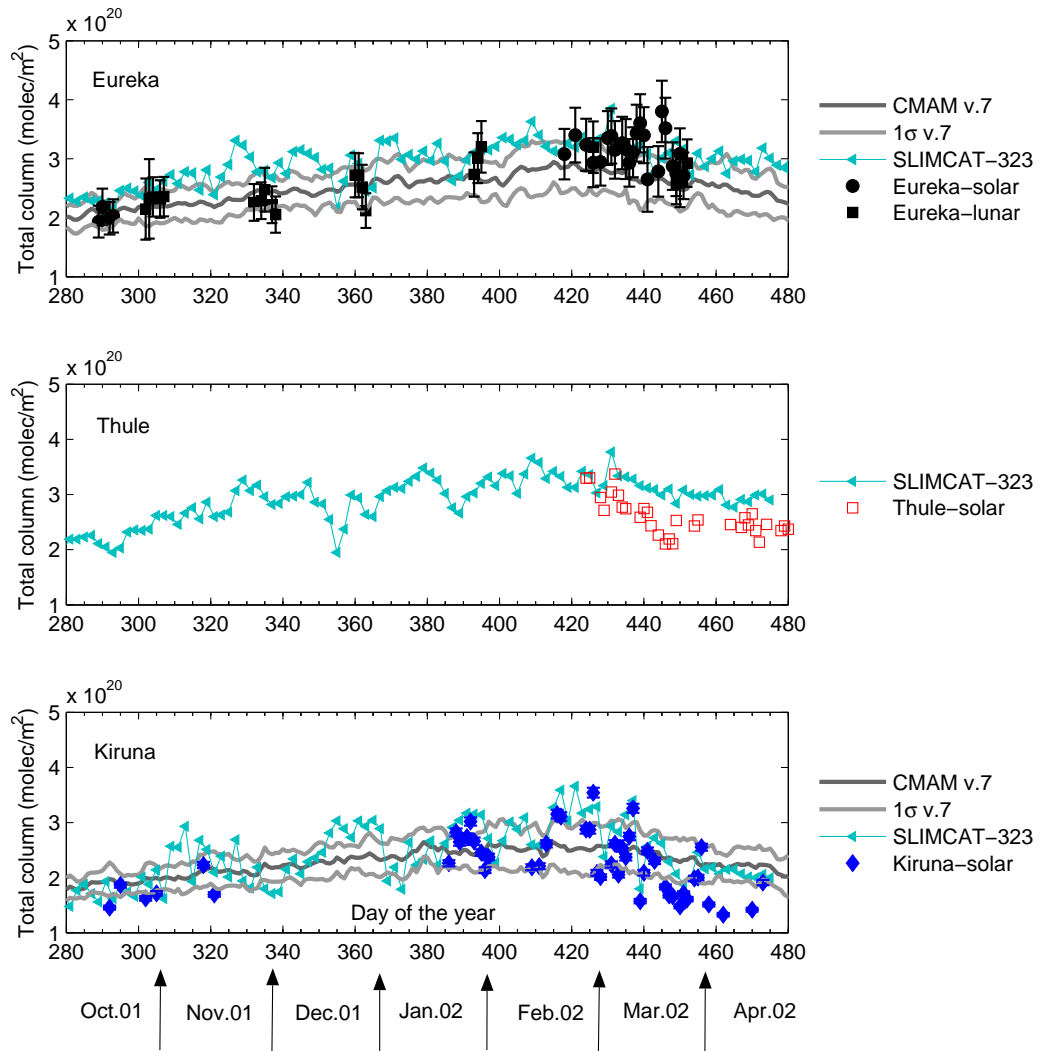
Figure 7.19: The top panel shows HNO_3 columns measured at Eureka compared with CMAM v.7 chemical fields at the closest grid point to Eureka and SLIMCAT 323 at Eureka. The middle panel shows HNO_3 columns measured at Thule compared with SLIMCAT 323 at Thule. The bottom panel shows HNO_3 columns measured at Kiruna compared with CMAM v.7 chemical fields at the closest grid point to Kiruna and with SLIMCAT 323 at Kiruna. The CMAM variability range is 1σ.

7.3 Tracer Comparisons

Nitrus oxide (N_2O), methane (CH_4) and hydrogen fluoride (HF) are three tracers with relatively long chemical lifetimes that can be used as passive tracers of motion, particularly in the lower stratosphere (*Solomon et al.*, 1986).

7.3.1 N_2O Columns

Comparison of N_2O total columns from the CMAM WMO run (v.5) with N_2O columns measured by the MSC FTS during the warm year of 1999 showed modeled N_2O columns $\sim$10% higher than the observed values, as shown in Figure 7.20 (top panel). Comparison of CMAM WMO N_2O with mid-latitude MANTRA profiles confirmed the results obtained in the Arctic (personal communication with S.M.L. Melo). CMAM v.7 N_2O columns were improved, yielding much better agreement with MSC FTS observations in 1999 as seen in Figure 7.20 and for the similar warm years of 2001 and 2003, shown in Figure 7.21.

During winter/spring 2000, the mean CMAM v.7 N_2O column is $\sim$10% higher than the observed columns. This can be explained considering the different meteorological conditions in CMAM v.7 and the atmosphere. Winter/spring 2000 was extremely cold as mentioned before, thus air parcels inside the vortex are isolated and cold thus, subside significantly more than those outside, leading to lower N_2O and CH_4 mixing ratio values inside the vortex on the same isentropic surface (*Gao et al.*, 2002).

SLIMCAT was also unable to simulate the conditions inside the vortex in winter/spring 2000 and reported N_2O columns as much as 17% larger than the measured values. For the other three years, the SLIMCAT columns agree with the MSC-FTS columns within the measurement errors.
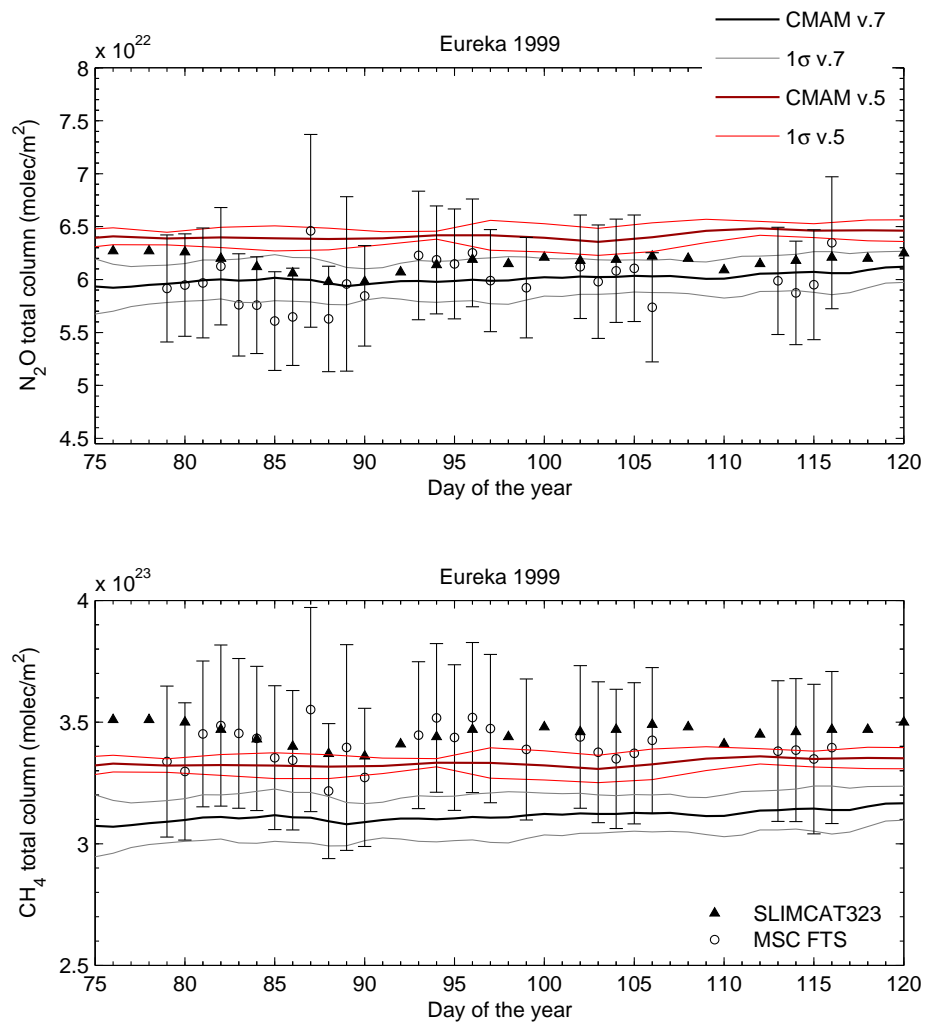
Figure 7.20: N$_2$O (top panel) and CH$_4$ (bottom panel) columns at Eureka during winter/spring 1999 compared with CMAM WMO (v.5), CMAM v.7 and SLIMCAT 323.
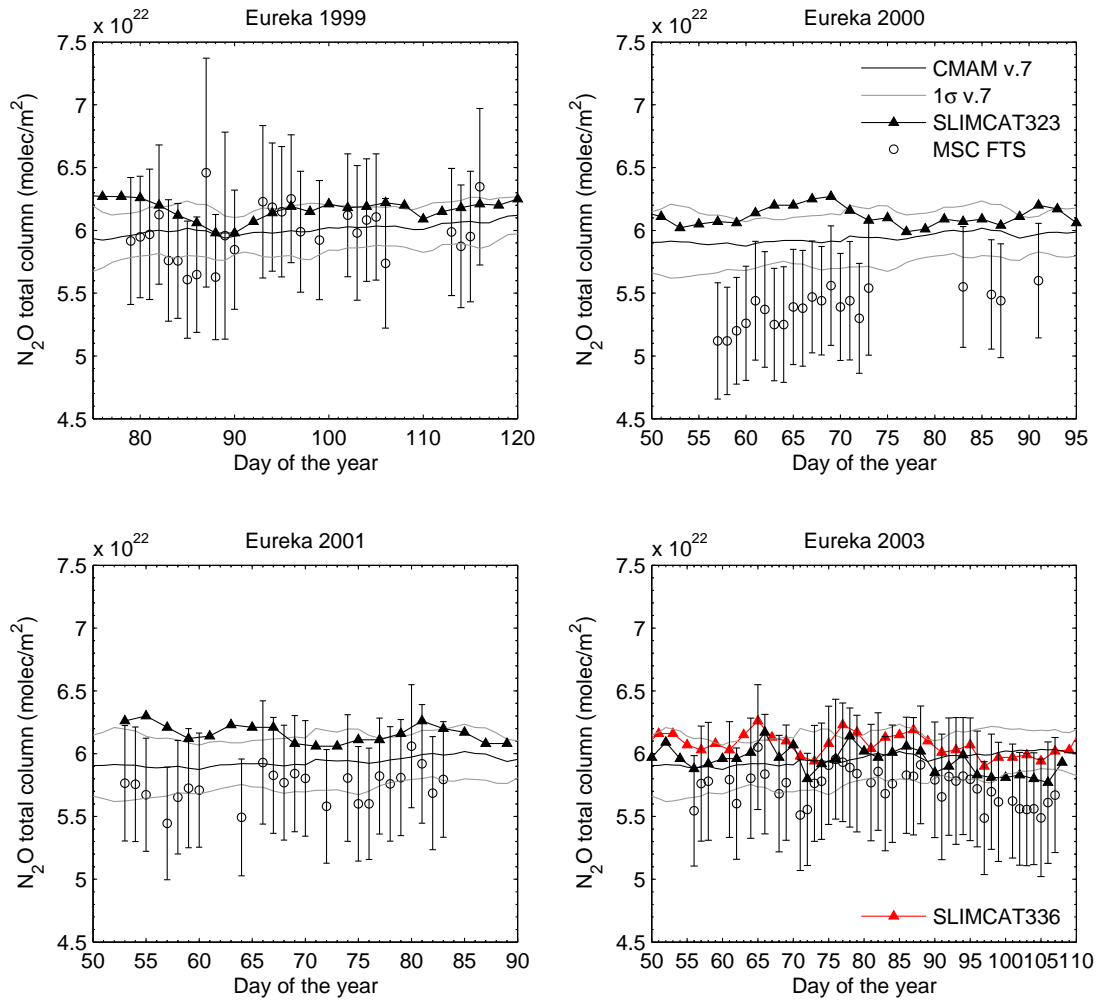
Figure 7.21: N₂O columns during winter/spring 1999, 2000, 2001 and 2003 at Eureka compared with CMAM v.7 and SLIMCAT 323.

7.3.2   CH$_4$ Columns

Figures 7.20 (bottom panel) and 7.22 shows the comparison of modeled and observed CH$_4$ columns. While CMAM WMO mean CH$_4$ columns represent the measured CH$_4$ columns well during warm years such as 1999 (Figure 7.20, bottom panel), CMAM v.7 CH$_4$ columns were only in agreement with reduced CH$_4$ columns in winter/spring 2000. This excellent agreement with the cold winter is not for the right reasons due to the CMAM v.7 warm climate. From CMAM v.7 comparison with observed values in the relatively warm winter/spring of 1999, 2001 and 2003, it is apparent that CMAM v.7 columns are consistently ∼10% lower than the observed columns.

SLIMCAT 323 CH$_4$ columns for three warm years of 1999, 2001 and 2003 agree well with MSC FTS observations. SLIMCAT mean CH$_4$ values for 2000 are systematically higher than measured values although just in agreement with observations within the measurement error.

7.3.3   HF Columns

In Figure 7.23, SLIMCAT 323 HF columns are compared with HF columns measured by the MSC FTS during winter/spring 1999, 2000, 2001 and 2003. SLIMCAT 323 reports, on average, 20% higher HF values than the MSC FTS for April 1999 and February and March 2000 and 2001; however, SLIMCAT day-to-day variability is similar to the observed variability. During 2003, SLIMCAT 323 HF columns are high by as much as 60% for February and March and ∼20% for April compared to the observed columns. The difference between modeled and observed HF columns was extensively reduced in the SLIMCAT 336 comparison for 2003. For February-March 2003, SLIMCAT 336 HF columns are ∼20% higher than observed columns while SLIMCAT 336 columns during April 2003 agree well with MSC FTS HF columns. SLIMCAT 336 HF columns for other years are the same as SLIMCAT 323.
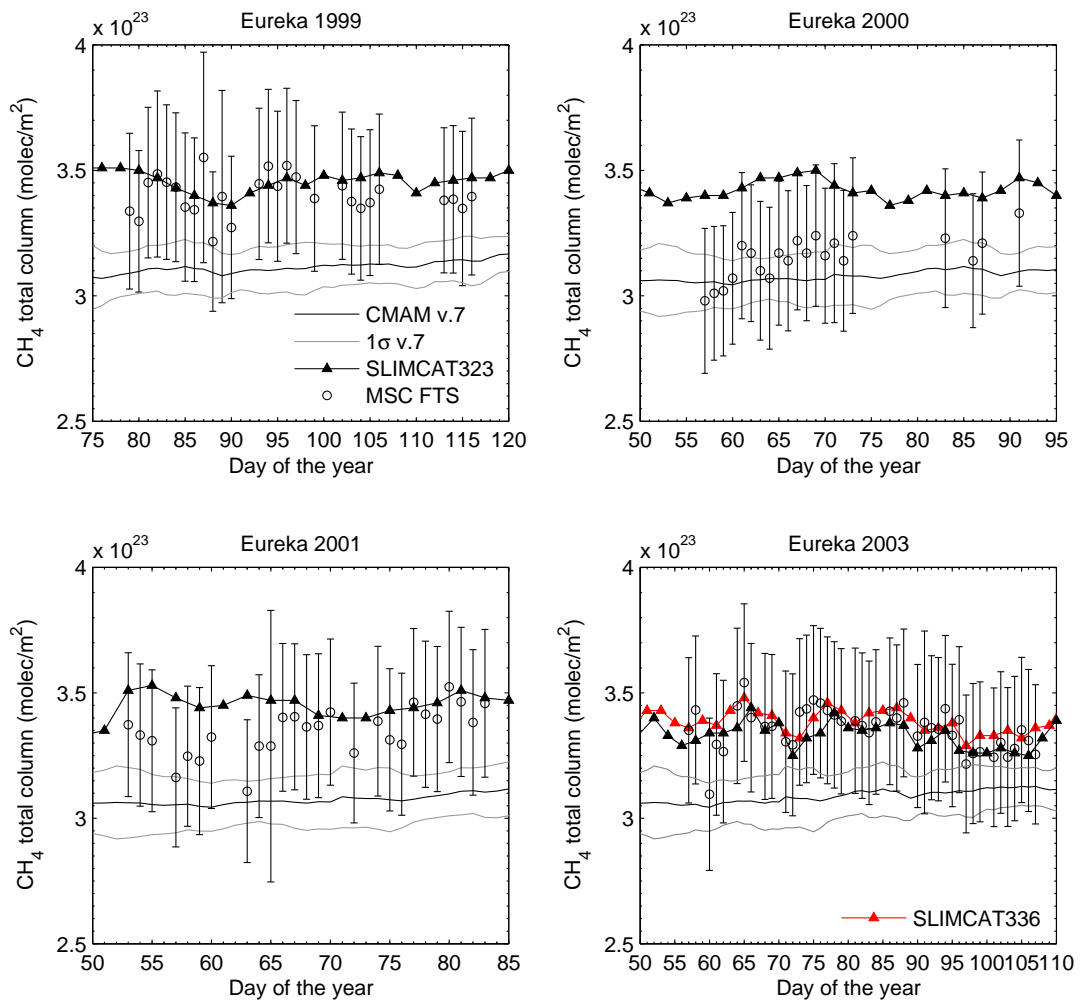
Figure 7.22: CH$_4$ columns during winter/spring 1999, 2000, 2001 and 2003 at Eureka compared with CMAM v.7 and SLIMCAT 323.
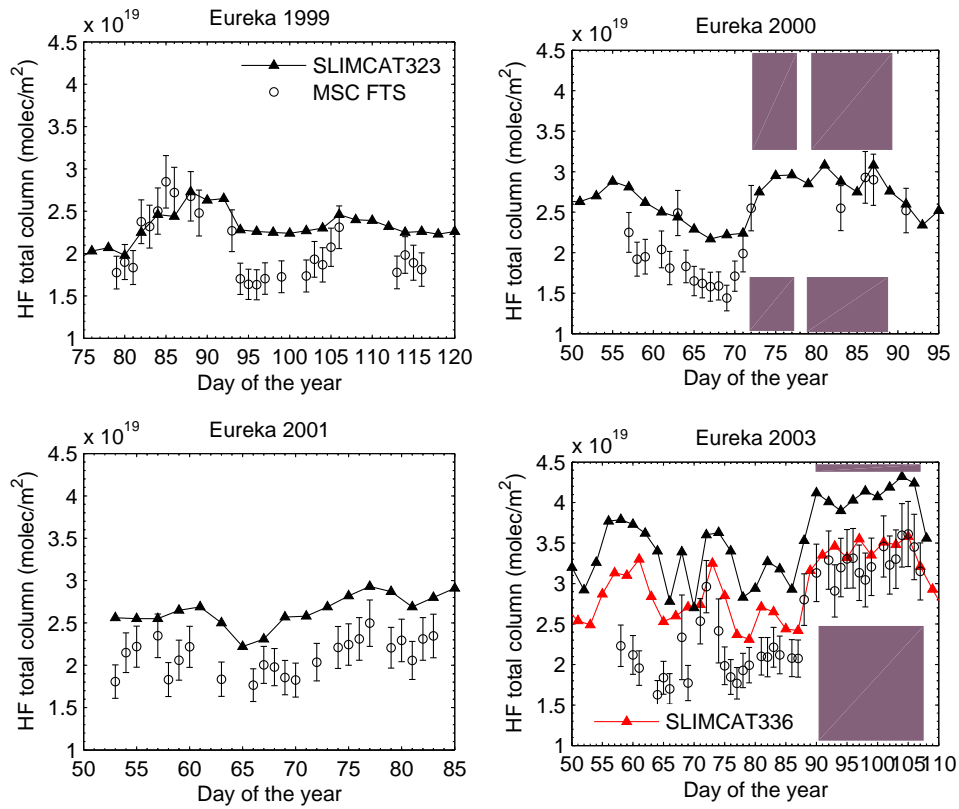
Figure 7.23: HF columns during winter/spring 1999, 2000, 2001 and 2003 at Eureka compared with SLIMCAT 323. The periods that Eureka was inside the vortex are marked by purple blocks.

7.4   Summary

For the first time, chemical fields from CMAM were compared with ground-based observations in the polar regions. Also, SLIMCAT vertical columns of O_3, NO_2, HNO_3, CH_4, N_2O, and HF were compared with observed values at Eureka for the first time.

In summary, the UT GBS total O_3 columns agreed with sonde measurements and coincident TOMS and GOME satellite measurements. CMAM climatological O_3 columns agree with UT GBS observed columns during the warm years of 1999, 2001 and 2003. Comparison of O_3 profiles from sonde data and different SLIMCAT runs helped evaluate the model's transport scheme. Deviations in O_3 vertical columns from climatological mean values were investigated using ECMWF PV maps. Low O_3 total columns during the cold winter/spring of 2000 were explained using ECMWF PV and temperature data. UT GBS NO_2 vertical columns agree with CMAM climatological NO_2 vertical columns during twilight for spring 1999 as well as with SLIMCAT vertical columns. CMAM NO_x columns compared well with the observed columns during the warm Arctic winters. CMAM-calculated partial NO_y was evaluated using the observed values.

Vertical columns of HNO_3 were measured for the first time at Eureka using the Moon as a light source. These lunar measurements were in good agreement with the solar values also obtained at Eureka just before and after polar night. The HNO_3 time series from fall to spring throughout the polar night was presented. CMAM v.7 climatological HNO_3 values compared well with Arctic HNO_3 measurements at Eureka and Kiruna, considering CMAM's inter-annual variability. The comparison revealed that CMAM simulates well the winter build-up and early-spring maximum of HNO_3 in the high Arctic. SLIMCAT 323 captured the magnitude of lunar and solar HNO_3 measurements at Eureka as well as the day-to-day variability at Eureka and Kiruna; however, SLIMCAT HNO_3 columns were higher than Thule and Kiruna measurements.

Recent CMAM and SLIMCAT model calculations of N_2O agreed with MSC FTS columns within measurement errors, while a comparison between SLIMCAT HF columns

and the observed values showed higher SLIMCAT values with similar day-to-day variability.

Generally, the inter-annual variability in CMAM v.7 was underestimated; therefore CMAM inter-annual variability does not fully cover the range of the observed variability, particularly for O_3 and for HNO_3 columns. Also this version of CMAM did not exhibit extremely cold winters and did not include heterogenous chemistry which meant no PSC formation nor sequestration of HNO_3 in PSCs. However, Arctic measurements show additional features that are specific to conditions inside the Arctic polar vortex.

Chapter 8

Applications of a Radiative Transfer Model

This chapter presents air mass factor (AMF) calculations for converting UT GBS O_3 and NO_2 DSCDs to VCDs using a multiple scattering radiative transfer (RT) model developed by C. McLinden. It includes a sensitivity study of the effects of NO_2 reference column density (RCD) uncertainties on the retrieval of NO_2 vertical profiles from NO_2 DSCDs calculated by the RT model. The NO_2 vertical profile retrieval method is also evaluated using climatological profiles.

8.1   Model Description

The radiative transfer model used here is described in detail by *McLinden* (1998). This model solves the RTE using successive orders of scattering in an inhomogeneous atmosphere. The radiance of photons which are scattered once, twice, three times and so on is calculated iteratively, with the total radiance taken as the sum over all scattering orders (*Hansen and Travis*, 1974). The direct solar beam and all scattering orders are calculated in a spherical atmosphere. The RT model geophysical inputs are vertical profiles of air number density, temperature, absorber number density, aerosol number density, aerosol

size distributions, refractive indices and surface albedo.

8.1.1   Air Mass Factor Calculation

O_3 and NO_2 AMFs were calculated by applying a 5% perturbation to the entire profile using:

$$AMF = \frac{ln\left(\frac{I(\lambda)}{I'(\lambda)}\right)}{k \times \Delta(VCD)}. \tag{8.1}$$

Here, $I'(\lambda)$ is the radiance incident on the instrument for a given atmosphere, $I(\lambda)$ is the radiance for the same atmosphere after perturbing the absorber profile, k is the absorption cross section of the species of interest and Δ(VCD) is the change in absorber column density. AMF calculations were done at the wavelength corresponding to the center of each spectral fitting window as the central wavelength is optimal for DOAS retrieval in the visible region (*Burrows et al.*, 1999a). O_3 AMFs, shown in Fig. 8.1 for the four Arctic campaigns, were calculated at 505 nm and as a function of SZA in 0.1º-0.5º increments while air number density, O_3 number density and temperature were input from ozonesonde data, and SAGE II aerosol data was used as the background stratospheric sulphate aerosol. The albedo value was taken to be 0.7 for Eureka and 0.2 for Vanscoy, typical of snow and prairie, respectively.

For the NO_2 AMF calculation at 425 nm, a modified version of the model was used which also allows the atmosphere to vary with SZA, as NO_2 is a diurnally varying absorber. Fig. 8.2 compares NO_2 AMFs calculated using the default version with those from the modified version of the RT model for February, March and April at Eureka. The same NO_2 AMFs were used for all four years, for a given month.

O_3 and NO_2 AMFs at the observed SZA for any given twilight spectrum were determined through linear interpolation. Interpolation, as opposed to direct calculation at specified SZAs, was found to have a negligible impact on AMF values (*Bassford et al.*, 2001).
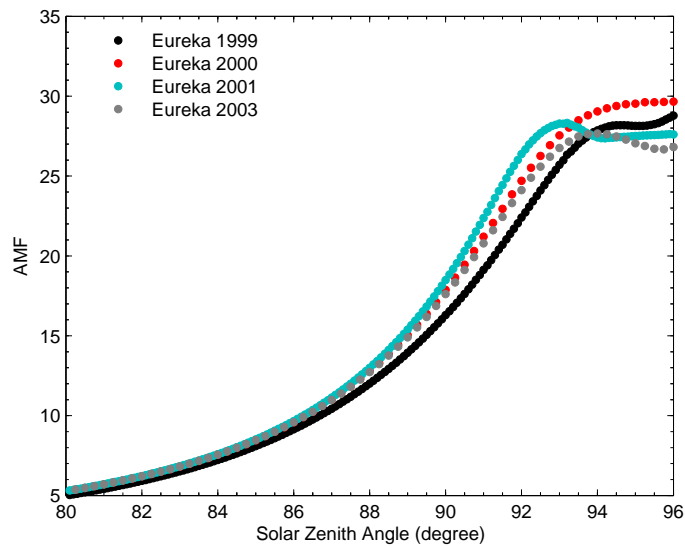
Figure 8.1: O_3 air mass factors for the four Arctic campaigns. Air number density, O_3 number density and temperature were input from the average ozonesonde data during each campaign.
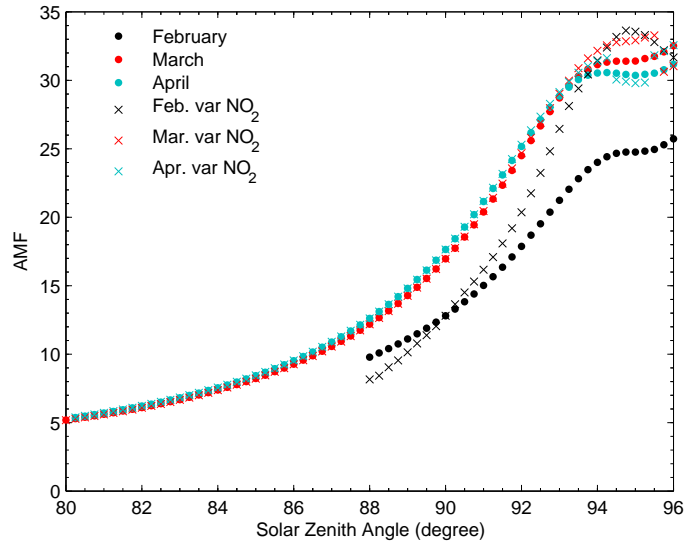
Figure 8.2: NO_2 air mass factors for February, March, and April. These were used for all four Arctic campaigns. The output of the modified version of the RT model which allows the atmosphere to vary with SZA is compared with the default version output.

8.1.2 NO$_2$ Reference Column Sensitivity Study

As explained in Chapter 2, the vertical distribution of stratospheric NO$_2$ can be retrieved from ground-based twilight zenith-scattered measurements. During twilight, the mean scattering altitude scans the stratosphere rapidly, which results in height-resolved information on the stratospheric NO$_2$ absorption. One of the parameters which complicates the retrieval and adds uncertainty to the retrieved vertical profile, as well as the retrieved vertical column, is the NO$_2$ RCD, which is the amount of NO$_2$ in the reference spectrum. As described in Chapter 5, the NO$_2$ RCD can be either calculated using a combination of a chemical box model and a RT model or derived from NO$_2$ DSCD measurements in the SZA range 80º to 85º, where the change in NO$_2$ amount is almost linear as a function of AMF, using pseudo-Langley plots. To quantify the effect of NO$_2$ RCD uncertainty on the retrieved NO$_2$ vertical profile, I used the RT model and a set of NO$_2$ profiles at SZA 90º for twilight conditions from the reference atmosphere of *Lambert et al.* (1999) to calculate climatological NO$_2$ slant column densities at the location of ASTRO.

The Lambert climatology provides stratospheric NO$_2$ as a function of latitude, altitude, and time of the year, for sunrise and sunset conditions. This climatology consists of measurements from space, balloons, and the ground, complemented by modeling results. It relies on sunrise and sunset profiles measured from 1995 through 1998 by the UARS Halogen Occultation Experiment (HALOE), and includes climatological characteristics determined from long-term observations of total stratospheric NO$_2$ from a network of ground-based UV-visible spectrometers, and NO$_2$ profiles measured by the SAOZ-balloon experiment at middle and northern high latitudes in various seasons. The climatological characteristics determine the type of function to be used for the least-square fitting of low-pass filtered HALOE NO$_2$ profile time series.

NO$_2$ slant column densities were calculated in the RT model using one set of NO$_2$ climatological twilight profiles from day 88 (March 29) at the location of ASTRO. A fixed RCD value of $1.29{\times}10^{16}$ molec/cm^2, the same as the UT GBS NO$_2$ RCD for Eureka
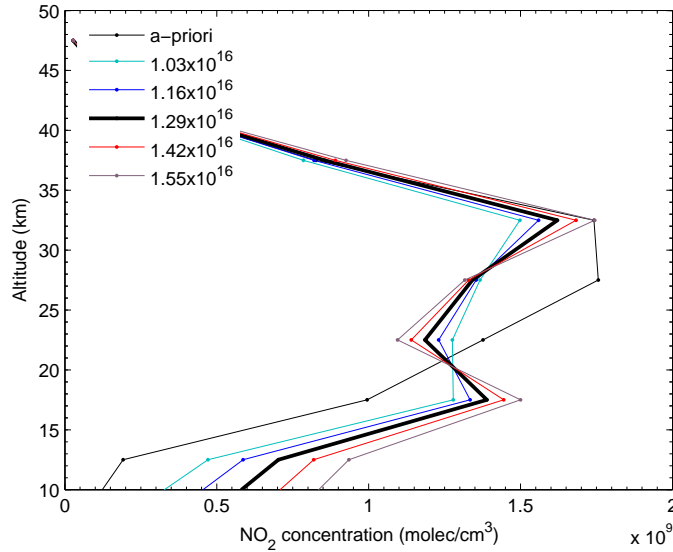
Figure 8.3: NO$_2$ vertical profiles retrieved using the true NO$_2$ RCD (thick black line) at SZA 90° as well as alternative RCDs perturbed by ±10% to 20%.

2000, was considered and subtracted from the calculated NO$_2$ slant column densities. The NO$_2$ vertical profile was retrieved back using the calculated slant columns and the fixed RCD (called true), using the Optimal Estimation Method described in Chapter 2. To determine the effect of RCD uncertainty on the retrieved profile, alternative RCDs were calculated by adding/subtracting 10% to 20% of the true RCD each time, obtaining RCDs ranging from 1.03×10^{16} molec/cm^2 to 1.55×10^{16} molec/cm^2. The NO$_2$ vertical profiles were retrieved using these alternative RCDs. As seen in Fig. 8.3, if the estimated RCD is higher than the true RCD, we overestimate tropospheric NO$_2$ in the retrieved profile, while for RCDs smaller than the true RCD, the retrieval assigns more NO$_2$ to the lower stratosphere. This result is consistent with the definition of NO$_2$ RCD as the amount of NO$_2$ in the high noon reference spectrum for which there is a significant contribution from the troposphere.

Fig. 8.4 shows that a 10% uncertainty in NO$_2$ RCD estimate, which is realistic based on the standard deviation of the derived RCDs from pseudo-Langley plots for Arctic measurements, results in an overall 5-10% change in the retrieved NO$_2$ vertical profile in
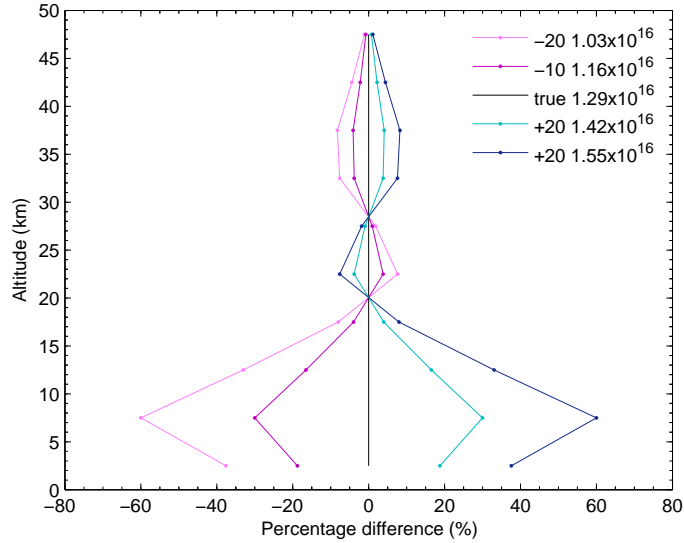
Figure 8.4: Percentage differences between NO_2 profiles retrieved using alternative RCDs and profile retrieved using the true RCD value.

the altitude range of 17 to 37 km where the retrieval is meaningful.

8.1.3   Evaluation of NO_2 Vertical Profile Retrieval

To evaluate how well the NO_2 profile retrieved from ground-based measurements represents the true state of the atmosphere, the method of *Rodgers and Connor* (2003) was applied to several sets of climatological profiles.

The Lambert climatological profiles of NO_2 at the location of ASTRO were used to generate NO_2 slant column densities as a function of SZA using the RT model. Applying the NO_2 profile retrieval code of *Preston* (1995) to these slant column densities, the NO_2 vertical distribution at 90º SZA was retrieved. Both the forward model and the box model used in the retrieval were independent of the Lambert climatological fields and the RT model. Here the a-priori profile is a NO_2 profile derived from the photochemical model and the SZA range is from 85º to 95º.

The retrieved profile $\hat{\mathbf{x}}$ is related to the true profile $\mathbf{x}$ and to the a-priori profile $\mathbf{x}_a$:

$$\hat{\mathbf{x}} - \mathbf{x}_a = A(\mathbf{x} - \mathbf{x}_a) + \epsilon_{\mathbf{x}} \tag{8.2}$$

where A is the averaging kernel matrix, and the error $\epsilon_{\mathbf{x}}$ in $\hat{\mathbf{x}}$ is due to random errors in the measurement and in the forward model (*Rodgers*, 2000). If $\mathbf{x}$ describes the altitude distribution of some quantity such as NO_2, the ith row of A can be considered as a smoothing function for the altitude corresponding to i with the width of this peak qualitatively indicating the vertical resolution of the retrieval.

Equation 8.2 can be used as the basis for comparing the retrieved vertical distribution of NO_2 with the Lambert high-resolution NO_2 climatological vertical profile which is considered the true state here. Substituting the climatological profile, $\mathbf{x}_t$, for $\mathbf{x}$ in Equation 8.2 and dropping the error term, gives:

$$\mathbf{x}_s = \mathbf{x}_a + A(\mathbf{x}_t - \mathbf{x}_a) \tag{8.3}$$

where $\mathbf{x}_s$ is the smoothed version of the climatological profile, which can be directly compared to the retrieved profile, $\hat{\mathbf{x}}$. Figures 8.5 and 8.6 show the result of the above exercise on day 78 (March 19) and 88 (March 29). The true profile from the climatological field for day 88 shows apparent signs of denitrification in the lower stratosphere, however the profile retrieved using the RT model calculation of DSCDs from the same true profile does not report the event and there are obvious discrepancies between the retrieved and true profiles. However, when the true profile was smoothed using Equation 8.3, the retrieved profiles are seen to agree with it within the error bars for both cases. The error in the retrieved profile includes the error in the forward model and the smoothing error. The exercise was performed on seven days during February, March and April, all of which gave similar results.
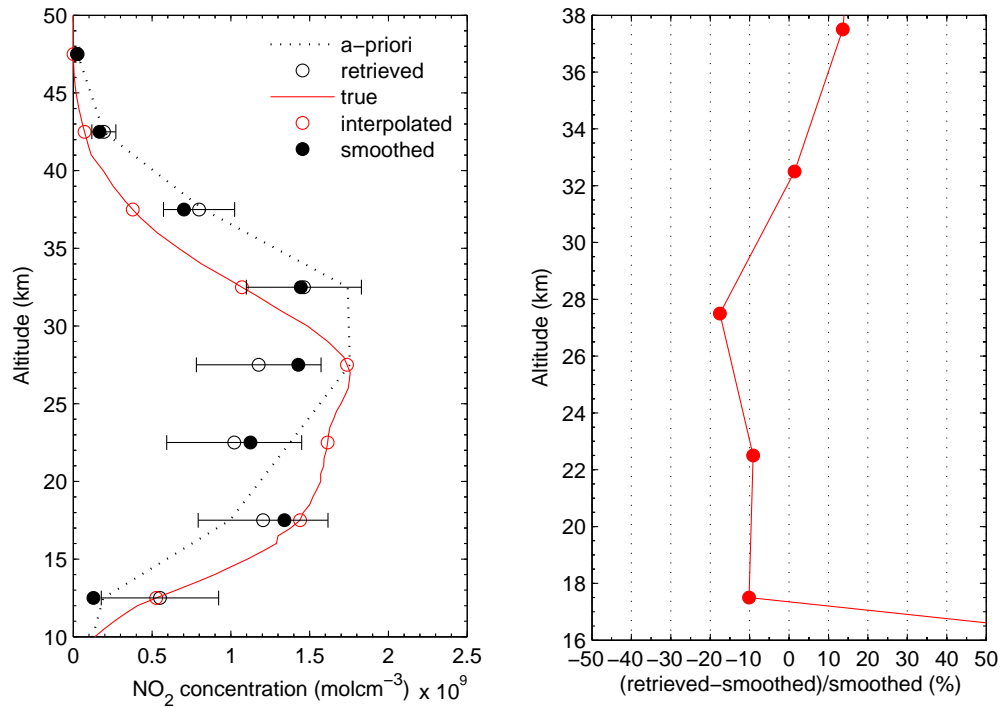
Figure 8.5: (left panel) The retrieved and true NO_2 profiles on day 78 (March 19) are seen to agree within the error bars once the smoothing effect is considered properly. (right panel) Percentage difference between retrieved and smoothed profile for the altitude range where the retrievals are meaningful.
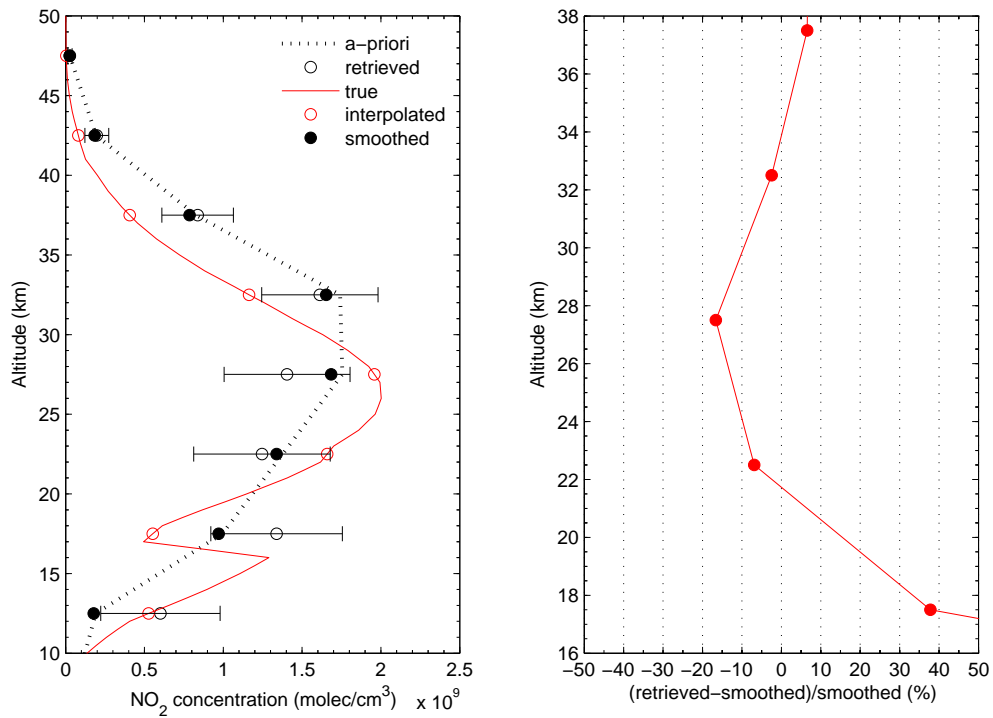
Figure 8.6: (left panel) The retrieved and true NO_2 profiles on day 88 (March 29) are seen to agree within the error bars once the smoothing effect is considered properly. (right panel) Percentage difference between retrieved and smoothed profile for the altitude range where the retrievals are meaningful.

8.2   Summary

AMFs for O_3 were calculated for each campaign using the RT model and information from ozonesondes. NO_2 AMFs were calculated using two different versions of the RT model for February, March and April at Eureka and the more realistic version of the model which changes the NO_2 profiles with SZA and along the path was used for final NO_2 AMF calculations. O_3 and NO_2 AMFs at observed SZAs for any given twilight spectrum were determined through linear interpolation.

A sensitivity study on the contributions of NO_2 RCD uncertainty to the retrieval of NO_2 vertical profiles was performed. An overestimate of the RCD relative to the true RCD results in an overestimation of tropospheric NO_2 in the retrieved profile, while a smaller RCD relative to the true RCD results in more NO_2 in the lower stratosphere. A 10% uncertainty in NO_2 RCD estimate translates to an overall 5-10% change in the retrieved NO_2 vertical profile in the altitude range from 17 to 37 km where the retrieval is meaningful.

A true profile taken from climatological fields shows denitrification in the lower stratosphere, while the resolution of the profile retrieved using the RT model calculation of DSCDs from the same true profile is unable to capture this event. However, smoothing the true profile with the averaging kernels of the retrieval results in agreement between the retrieved profile and smoothed climatological profile.

Chapter 9

Conclusions

9.1 Summary of Thesis

Ground-based UV-visible zenith-sky spectroscopic measurements of O_3, NO_2 and OClO columns were made using a triple-grating spectrometer deployed in the Canadian High Arctic during springtime of 1999-2003. The instrument was characterized using laboratory measurements and was deployed four times in the Arctic and twice as part of the MANTRA project. The use of two different algorithms for DSCD retrieval allowed the fitting procedure to be optimized and increased the possibility of retrieving DSCDs during the period right after polar sunrise. For the first time, OClO DSCDs were retrieved from UV-visible measurements in the Canadian High Arctic during winter/spring 2000.

The UT GBS O_3 total columns for MANTRA 2000 and 2002 were compared with the on-site Brewer spectrometer data, and with the TOMS and GOME satellite instruments. The comparison resulted in an agreement of 6% or better for both MANTRA 2000 and 2002 field seasons. The NO_2 total columns during sunrise and sunset were retrieved during both campaigns. The diurnal variability of NO_2 columns was captured by the retrieved total columns.

The UV-visible O_3 and NO_2 measurements in the Arctic were combined with the co-

located infrared measurements made during the same period using the MSC FTS. This combined data set was compared with the chemical fields of two atmospheric models, the Canadian Middle Atmosphere Model and SLIMCAT. The comparison of the four-year UV-visible-IR data set with the chemical fields of CMAM and SLIMCAT helped with the assessment of their chemical fields, e.g. it was recognized that N_2O values were high in the CMAM WMO version (v.5) and the O_3 was mixed too fast in the lower stratosphere in the SLIMCAT 311 run. Discrepancies between observed and modeled values were addressed which resulted in improved modeling of the atmosphere. For the first time, CMAM chemical fields were compared with observations in the Arctic to evaluate the chemical fields of this GCM, particularly with regard to their close representation of the mean state of the atmosphere and their estimates of inter-annual variability for O_3 and the nitrogen family.

CMAM chemical fields of O_3, NO_2, NO_x, HNO_3, partial NO_y, N_2O, and CH_4 were evaluated using the combined UV-visible-IR total column measurements. The comparison of CMAM with the warm Arctic winters of 1999, 2001 and 2003 provided an opportunity to test the model simulations under PSC-free conditions. These comparisons resulted in an agreement of better than 5% between the observed and the CMAM climatological O_3 columns, while the CMAM NO_2 twilight columns were the same as UT GBS NO_2 columns both within measurement errors which are $\pm 5\%$ for O_3 columns and $\pm 12\%$ for NO_2 columns. CMAM and MSC FTS NO_x columns agreed within 2σ uncertainties except for the cold year of 2000. Partial NO_y columns agreed well within measurement errors. CMAM and MSC FTS N_2O columns were the same within uncertainties apart from 2000. The same conclusions were made for CH_4; however the CMAM mean CH_4 column was $\sim 10\%$ lower than the mean measured column during the warm years of 1999, 2001 and 2003. Generally, CMAM HNO_3 columns agreed within 1σ variability with the MSC FTS observations. The inter-annual variability in CMAM v.7 is smaller than the true variability, particularly for O_3 and HNO_3 columns. Also, CMAM v.7 did not exhibit

extremely cold winters and did not include heterogeneous chemistry which meant neither PSC formation nor sequestration of HNO_3 in PSCs.

The first lunar measurements of HNO_3 at Eureka were in good agreement with the solar values also obtained at Eureka as well as with HNO_3 measurements at Thule. The HNO_3 time-series from fall to spring throughout the polar night captured the seasonal behaviour of HNO_3 in this region. CMAM v.7 climatological HNO_3 values compared well with HNO_3 measurements at Eureka and Kiruna, considering CMAM's inter-annual variability. The comparison revealed that CMAM simulates well the winter build-up and early-spring maximum of HNO_3 in the high Arctic under warm conditions.

SLIMCAT O_3 columns were generally higher than the observed values. Comparison of O_3 profiles from sonde data indicated the fast O_3 mixing in the upper troposphere-lower stratosphere. The profile comparison helped assess the model's transport scheme. Day-to-day variability in O_3 vertical columns was explained using ECMWF PV and temperature data. SLIMCAT twilight NO_2 vertical columns agree well with UT GBS NO_2 vertical columns during twilight for spring 1999. SLIMCAT captured the magnitude of the measured HNO_3 values as well as the day-to-day variability at Eureka and Kiruna; however SLIMCAT HNO_3 columns were higher than Thule and Kiruna measurements. The SLIMCAT total columns of CH_4 were the same as MSC FTS observations within measurement errors for warm winters; although during 2000 SLIMCAT reported CH_4 columns $\sim$19% higher than the mean measured column. Apart from SLIMCAT N_2O columns during 2000, which are $\sim$13% higher than the observed values, SLIMCAT N_2O columns agreed with the observed values within measurement errors. Comparison between SLIMCAT HF columns and the observed values showed higher SLIMCAT values by as much as $\sim$60% with similar day-to-day variability.

Two different versions of McLinden's RT model were used, along with information from ozonesondes, to calculate AMFs for O_3 for 1999, 2000, 2001, and 2003 and NO_2 for February, March and April at Eureka. Using the same RT model, a sensitivity study

on the contributions of NO_2 RCD uncertainty to the retrieval of NO_2 vertical profile was performed. A 10% uncertainty in NO_2 RCD estimate translates into an overall 5-10% change in the retrieved NO_2 vertical profile in the altitude range of 17 to 37 km where the retrieval is meaningful. The NO_2 vertical profile retrieval method was tested using climatological profiles; when the limitations in the retrieval process were taken into account and the climatological profile was smoothed to the resolution of the measurements, the retrieved profile agreed with the climatological profile within retrieval uncertainty throughout February, March and April.

This work extended the temporal and geographical range of polar stratospheric observations. In addition, it strengthened Canadian capabilities in monitoring the Arctic stratosphere during the crucial period of late winter-early spring when O_3 depletion occurs. This project is part of an ongoing research program which will provide a long-term data set in the Canadian High Arctic.

9.2 Outlook

In future, several improvements can be made to the instrument, viewing geometry, retrieval algorithms, measurements and modeling components of this project to reduce uncertainties of the measurements, accomodate new types of measurements and enhance our understanding of atmospheric processes.

An improvement in the CCD detector and an increase in the light throughput of the instrument would facilitate measurements at SZAs greater than 94º and of other species such as BrO. Updating the OClO and BrO cross sections to cross sections measured at representative stratospheric temperatures, such as *Kromminga et al.* (2003) for OClO, would also improve the quality of the retrieval. The error analysis can be done for OClO slant columns once more measurements are made.

Combining two different ground-based viewing geometries, zenith-sky and direct-sun,

would achieve stratospheric and tropospheric sensitivity for isolating tropospheric BrO from its stratospheric component. Using multi-axis measurements would also increase the sensitivity to the troposphere at noon. Stellar observations of NO_3 during polar night using the UT GBS combined with Atmospheric Emission Radiometric Interferometer (AERI) and FTS infrared measurements of other species such as HNO_3 and N_2O would provide insight into chemical processes during the Arctic dark season.

Applying the SFIT2 algorithm to the MSC FTS data set would provide partial columns and altitude information for different tropospheric and stratospheric species, which would be advantageous in understanding the polar processes in more detail. Incorporating a more up-to-date chemical box model into the NO_2 profile retrieval software would improve the retrieval of NO_2 profiles from UT GBS DSCDs. The chemical box model can also be applied to NO_2 observations at different times of day, which would enable us to compare different measurements more closely. Having vertical information for different species would provide the opportunity for chemical correlation studies in the Arctic to discriminate chemical change in O_3 from large variations due to dynamical processes (*Proffitt et al.*, 1993; *Sankey and Shepherd*, 2003).

The Canadian Network for the Detection of Atmospheric Change (CANDAC) initiative will maintain the possibility of having a full suite of measurements year-round at the Eureka location. In particular, infrared emission measurements during polar winter would complement the data set and provide the means for evaluating the seasonality and inter-annual variability of the stratosphere over Eureka. Combining the Eureka data set with data sets from other NDSC Arctic sites (such as Thule and Kiruna) would improve our knowledge of atmospheric processes over a wider geographical area.

Having CMAM-assimilated fields would help with more direct comparison with observations and improve the modeling of the atmosphere. Also, CMAM and SLIMCAT vertical profiles of different species combined with measured profiles can be used to investigate the chemical correlations in the Arctic.

Appendix A

Terminology

A.1 Astigmatism

Astigmatism is a phenomenon that occurs when a spherical optical element is used off-axis. Light rays lying in different planes tend to be focused on different curved surfaces, which results in the formation of a blurred image that is oval in shape. The details of astigmatism and spherical aberrations can be found in most general optics texts, e.g. (*Hecht*, 1998; *Longhurst*, 1973).

A.2 Blaze Wavelength

To increase the efficiency of a grating for a particular non-zero order at a particular wavelength, the surfaces of gratings are cut in a triangular shape at a particular angle, the blaze angle, relative to the grating original surface as shown in Fig. A.1. The blaze angle is a function of the wavelength, determined by considering the grating in the Littrow position, which is the position in which light departing the grating returns along the path taken to arrive at the grating. If we consider the grating equation:

$$m\lambda = d(sin\alpha + cos\beta) \tag{A.1}$$

159
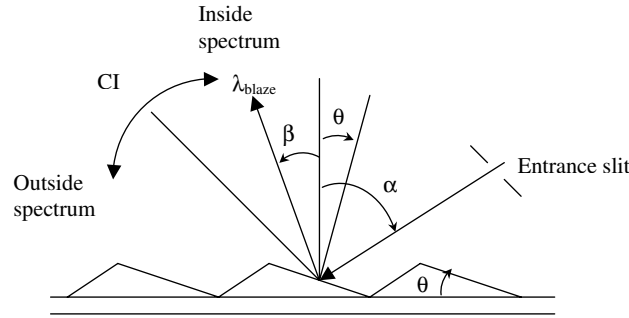
Figure A.1: Cross section of a blazed grating; θ is the blaze angle.

where α and β are the angles of incidence and diffraction, respectively, d is the spacing between the grating lines, m is the order of spectrum, and λ is the wavelength. The blazed wavelength is given by

$$m\lambda = 2dsin\theta + cos(\alpha - \theta). \tag{A.2}$$

A.3 Back-Illuminated CCD

In back-illuminated CCDs the light arrives from the silicon side, not from the electrode side; thus the quantum efficiency of this type of CCD is higher while the silicon layer is thinner, as shown in Fig. A.2.

A.4 Charge-Coupled Device

The basis of CCD operation is a unit cell of a MOS (Metal Oxide Semiconductor) capacitor with a silicon substrate. A positive voltage applied to the top metal electrode causes the underlying silicon to be in depletion thus attracting negatively charged electrons. These potential wells under the electrodes are called channels and in between channels inactive material appropriately doped forms channel stops. In each exposure time, electrons accumulate in the wells and are transported to an output gate and amplifier using
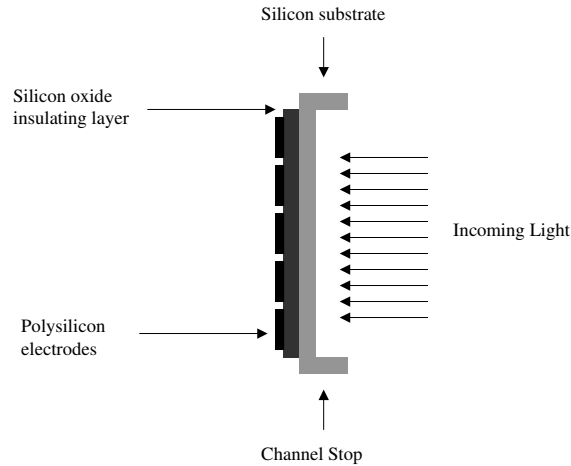
Figure A.2: Back-illuminated CCD.

clock potentials. There are separate clocks for each gate and all of the gates in a block, such as a readout register are connected in parallel; thus charge packets shift through each gate in with respect to the cycling of each clock line (*Shepherd*, 2002).

A.5   Czerny-Turner Design

The Czerny-Turner spectrometer design eliminates spherical aberrations and related effects. In this design, spherical mirrors with large diameters are used in such a way as to cancel the spherical aberrations (*Williams*, 1976).

A.6   Dark Current

Thermal electrons that are spontaneously generated in the CCD detector generate dark current. It is apparent that dark current strongly depends on the CCD's temperature, its intensity decreases by about a factor of two each time the CCD temperature is lowered by 7° C. Dark current is also quasi-proportional to the integration time. Thus a long enough exposure time or high enough temperature can consume a CCD's dynamic range and cause saturation. Dark current also varies with CCD pixel size and it is summed up

as pixels are binned.

The dark current is usually measured as the number of thermal electrons per pixel per unit time and is reproducible with a narrow statistical dispersion, having the same CCD detector and the identical temperature conditions. The dark current generates a noise called dark noise that obeys the square root of the signal.

A.7 Dynamic Range

Dynamic range is defined as the ratio of the largest measurable useful signal to the smallest detectable useful signal. The readout noise of the detector sets a limit to the smallest readable signal and the charge storage capacity of the readout registers set a limit to the maximum signal intensity.

A.8 Field-of-View (FOV)

The field-of-view is the area in the focal or image plane of the spectrometer that is visible through the optical elements under consideration. Angular FOV is defined as the angle for which a cone, with its apex at the lens or mirror, represents the FOV.

A.9 Flat Field Output

When all points of the output image are located on the focal plane and there is no distortion of the image, the output is considered flat field.

A.10 f-number

The f-number is a measure of the speed of an optical system. It is defined as the ratio of the focal length to the aperture diameter for a circular aperture.

$$f - number = \frac{f}{D} \tag{A.3}$$

For a rectangular aperture, as is the case for most grating spectrometers, the effective f-number can be calculated as the ratio of the focal length to the diameter of a circle whose area is equal to the area of the rectangular aperture.

$$f - number_{eff} = \frac{f}{\acute{D}} \tag{A.4}$$

where

$$\acute{D} = 2\sqrt{\frac{width \times height}{\pi}} \tag{A.5}$$

The concept of f-number is also useful to position the baffle at the entrance of the spectrometer since it restricts the spatial extent of the beam of light passing through an optical aperture.

A.11 Focal Plane

A plane normal to the symmetry axis of an optical element that is passing through the image focus is called focal plane.

A.12 Optical Filters

Optical filters are used to restrict the spectral bandwidth that enters the spectrometer. They thus exclude unwanted wavelengths, which in turn reduces the amount of stray light inside the spectrometer. Stray light is the scattered light inside the spectrometers that illuminates the detector but has traveled along a path other than the designed path through the system.

A.13   Plane Holographic Diffraction Gratings

A simple plane holographic grating is made by projecting a laser-generated interference pattern onto a high-resolution film. A few advantages of holographic gratings compared to ruled ones are the lack of ruling ghosts, the capability of reducing astigmatism and the small intensity of the stray light (*Williams*, 1976).

A.14   Quantum Efficiency

Quantum efficiency is a measure of the CCD spectral response at particular wavelength. It is expressed as the number of photoelectrons produced per incident photon and it is wavelength dependent in general.

A.15   Spectral Resolution

Below is the equation for the position of the peaks for each wavelength that is driven from the irradiance expression:

$$n\lambda = d(sin\theta_i - sin\theta_d) \tag{A.6}$$

where d is the separation of the grating lines, θ_i is the angle of incidence, θ_d is the diffraction angle, n is the order of interference and λ is the wavelength. Then differentiating the above relationship where the only variable is the diffraction angle, the resolution can be written as:

$$\Delta\lambda = \frac{dcos\theta_i d\theta_i}{n} \tag{A.7}$$

Better (higher) spectral resolution is obtained at smaller separation of the grating lines, higher orders of interference and the diffraction angle closer to 90º. The wavelength resolution of a grating is a function of angle in the image plane.

A.16   Sampling Ratio

Sampling ratio is the ratio of the width of the resolution function to the pixel spacing. It is commonly defined as the number of pixels per FWHM, the full width of spectral lines at their half maximum.

A.17   Signal-to-Noise Ratio (SNR)

The ratio of the light intensity to noise, the sum of random fluctuations caused by spurious electronic signals produced by the source or the detector, thermally generated or generated in amplifying equipment, is called the signal-to-noise ratio. The SNR defines a lower limit on observable signals.

A.18   Spectral Bandwidth

Spectral bandwidth is defined as the range of wavelengths that the detector measures for a given optical configuration and grating. It can be expressed as total average about a central wavelength or as a range of wavelengths from a minimum to a maximum of the CCD center wavelength.

A.19   Spherical Aberration

Spherical aberration, shown in Fig. A.3, in general, refers to blurring of the image due to departures from Gaussian Optics. When rays are passing through different parts of the spherical optical elements, e.g. rays passing through the center of a lens compared to rays passing through the edge of the lens, they will be focused at slightly different places on the focal plane and this results in a blurred image.
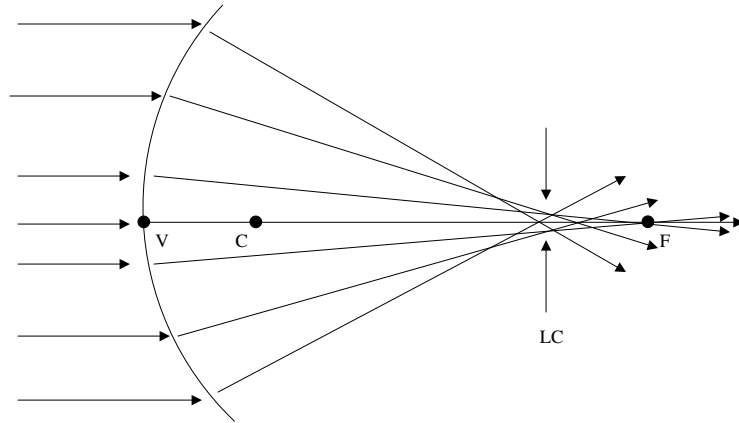
Figure A.3: Example of spherical aberration using a lens surface. Rays crossing nearer to the vertex focus at the paraxial focus. Rays further from the vertex focus closer to the lens surface. The circle of least confusion is indicated at position at LC.

A.20   Undersampling

Undersampling occurs when the information content of the spectrum, as smoothed by the instrument, is not fully Nyquist sampled, that is, not sampled to twice the highest spatial frequency spread out over the detector array. Depending on the precise instrument transfer function, undersampling can be substantial even when the sampling is at 3 or 4 times the spectrometer resolution, given as the FWHM. A Gaussian, for example is significantly undersampled at 3 samples per FWHM but not at 4 samples per FWHM (*Chance et al.*, 2005). *Roscoe et al.* (1996) show that sampling ratios should be 4.5 to 6.5 pixels/FWHM to avoid interpolation errors when ratioing one UV-visible spectrum to another.

Appendix B

LabVIEW Software for Automated Operation

Laboratory Virtual Instrument Engineering Workbench (LabVIEW) is a graphical software package with block diagrams and flow charts developed by National Instruments. In 1999, David Rogerson in the Physics Electronic Resource Centre (PERC) and undergraduate student Neilank Jha used LabVIEW to create software which automated the control of the UT GBS. The code basically works based on a series of short snapshots between 0.01 and 5.00 s to optimize the integration time. The final snapshot exposure time is determined through a cascade of predetermined times for snapshots to optimise the received signal. Sanpshots are recorded for a user-defined time until a signal is obtained which is greater than the user-defined number of counts. If the user-defined number of counts is not achieved after the longest snapshot time, it means the light levels are insufficient for recording zenith-scattered spectra; thus the system starts to record dark current based on user-defined number of accumulations. Figure B.1 is a flowchart showing the LabVIEW software for UT GBS automation.
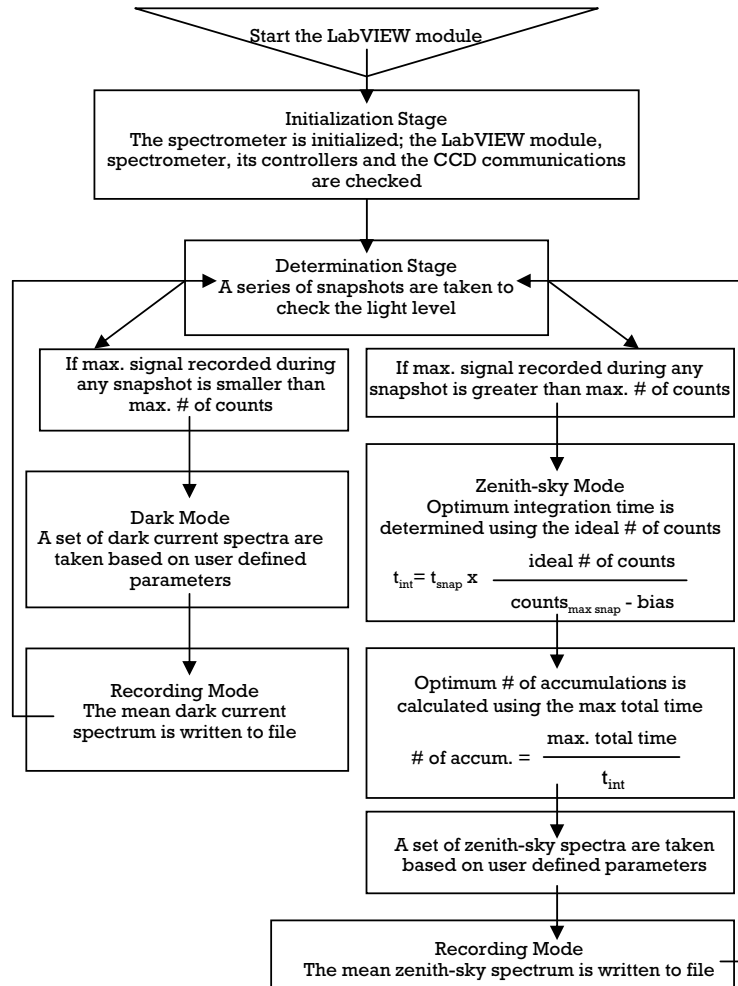
Figure B.1: LabVIEW software flowchart to automate the UT GBS control.

Appendix C

WinDOAS Software

WinDOAS software has been developed at BIRA (*Fayt and van Roozendael*, 2001) and below are the flowcharts explaining the overall process of retrieving DSCDs as well as the wavelength calibration process.
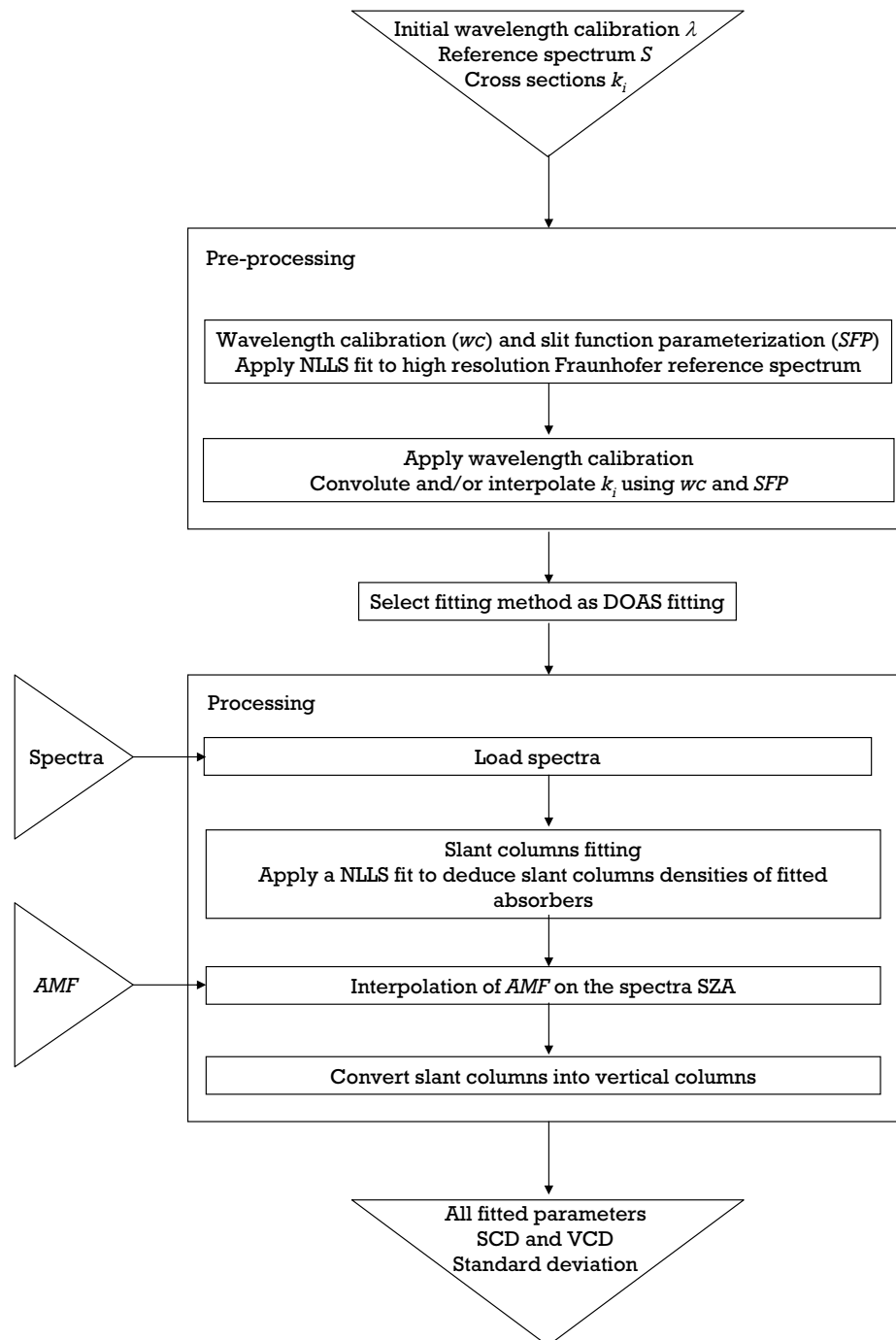
Figure C.1: Overall WinDOAS retrieval procedure.

Initial wavelength calibration λ
Reference spectrum S
High-resolution solar spectrum
Cross sections k_i

Select calibration interval and split into N sub-windows

Select Fitting method (DOAS)

Slant columns fitting

Derive in each interval n:

- The shift between $solar_n$ and S_n;
- Fitted slit function parameters SFP_n;
- SCD of correcting absorbers (e.g. Ring, O_3)

Determine the new wavelength calibration (wc) by polynomial fitting
through the N individual shift values

Determine wavelength dependency of fitted slit function
parameters ($SFP_n(\lambda)$) by polynomial fitting through
the N individual SFP_n values

Display calibration results (optional)

$wc,$
$SFP(\lambda)$

Figure C.2: Wavelength calibration procedure in WinDOAS.

Bibliography

ACIA (2005), *Arctic Climate Impact Assessment 2005 – Chapter 5: Ozone and ultraviolet radiation*, Cambridge University Press, New York, NY, USA.

Akiyoshi, H., T. Sugita, H. Kanzawa, and N. Kawamoto (2004), Ozone perturbations in the Arctic summer lower stratosphere as a reflection of NO_x chemistry and planetary scale wave activity, *J. Geophys. Res.*, *109*, doi:10.1029/2003JD003632.

Allen, D. R., R. M. Bevilacqua, G. E. Nedoluha, C. E. Randall, and G. L. Manney (2003), Unusual stratospheric transport and mixing during the 2002 Antarctic winter, *Geophys. Res. Lett.*, *30*, doi:10.1029/2003GL017117.

Andersen, S. B., and B. M. Knudsen (2002), The influence of vortex ozone depletion on Arctic ozone trends, *Geophys. Res. Lett.*, *29*, doi:10.1029/2001GL014595.

Anderson, J. G., and O. B. Toon (1993), Airborne Arctic Stratospheric Expedition - An overview, *Geophys. Res. Lett.*, *20*, 2499–2502.

Anderson, J. G., D. W. Toohey, and W. H. Brune (1991), Free radicals within the Antarctic vortex: The role of CFCs in Antarctic ozone loss, *Science*, *251*, 30–45.

Andrews, D. G. (2000), *An Introduction to Atmospheric Physics*, Cambridge University Press, Cambridge, UK.

Austin, J., D. Shindell, S. R. Beagley, C. Brühl, M. Dameris, E. Manzini, T. Nagashima, P. Newman, S. Pawson, G. Pitari, E. Rozanov, C. Schnadt, and T. G. Shepherd (2003),

Uncertainties and assessments of chemistry-climate models of the stratosphere, *Atmos. Chem. Phys.*, *3*, 1–27.

Banwell, C. N., and E. M. McCash (1994), *Fundamentals of Molecular Spectroscopy*, McGraw-Hill Book Company, London, UK, fourth edition.

Bassford, M. R., C. A. McLinden, and K. Strong (2001), Zenith-sky observations of stratospheric gases: The sensitivity of air mass factors to geophysical parameters and the influence of tropospheric clouds, *J. Quant. Spectros. Radiat. Transfer*, *68*, 657–677.

Bassford, M. R., K. Strong, C. A. McLinden, and C. T. McElroy (2005), Ground-based measurements of ozone and NO_2 during MANTRA 1998 using a new zenith-sky spectrometer, *Atmos.-Ocean*, *43*, 325–338.

Beagley, S. R., J. de Grandpré, J. N. Koshyk, N. A. McFarlane, and T. G. Shepherd (1997), Radiative-dynamical climatology of the first-generation Canadian Middle Atmosphere Model, *Atmos.-Ocean*, *35*, 293–331.

Becker, G., R. Müller, D. S. McKenna, M. Rex, K. S. Carslaw, and H. Oelhaf (2000), Ozone loss rates in the Arctic stratosphere in the winter 1994/1995: Model simulations underestimate results of the Match analysis, *J. Geophys. Res.*, *105*, 15,175–15,184.

Bernath, P. F., C. T. McElroy, M. C. Abrams, C. D. Boone, M. Butler, C. Camy-Peyret, M. Carleer, C. Clerbaux, P. F. Coheur, R. Colin, P. de Cola, M. de Maziere, J. R. Drummond, D. Dufour, W. F. J. Evans, H. Fast, D. Fussen, K. Gilbert, D. E. Jennings, E. J. Llewellyn, R. P. Lowe, E. Mahieu, J. C. McConnell, M. McHugh, S. D. McLeod, R. Michaud, C. Midwinter, R. Nassar, F. Nichitiu, C. Nowlan, C. P. Rinsland, Y. J. Rochon, N. Rowlands, K. Semeniuk, P. Simon, R. Skelton, J. J. Sloan, M. A. Soucy, K. Strong, P. Tremblay, D. Turnbull, K. A. Walker, I. Walkty, D. A. Wardle, V. Wehrle, R. Zander, and J. Zou (2005), Atmospheric Chemistry Experiment (ACE): Mission overview, *Geophys. Res. Lett.*, *35*, doi:10.1029/2004JD005559.

Beyerle, G., B. P. Luo, R. Neuber, T. Peter, and I. S. McDermid (1997), Temperature dependence of ternary solution particle volumes as observed by lidar in the Arctic stratosphere during winter 1992/1993, *J. Geophys. Res.*, *102*, 3603–3609.

Blumenstock, T., F. Hase, A. Griesfeller, R. Ruhnke, H. Fischer, U. Raffalski, and Y. Kondo (2003), Chlorine activation, ozone loss and sequestration of nitric acid in PSCs as observed by ground-based FTIR measurements during winter at Kiruna (Sweden) since winter 1993/94, in *EWP03–European Commission - Air pollution research report 79*, pp. 51–54, European Commission.

Bramstedt, K., J. Gleason, D. Loyola, W. Thomas, A. Bracher, M. Weber, and J. Burrows (2002), Comparison of total ozone from the satellite instruments GOME and TOMS with measurements from the Dobson network 1996-2000, *Atmos. Chem. Phys. Discuss.*, *2*, 1131–1157.

Brasseur, G., and S. Solomon (1984), *Aeronomy of the Middle Atmosphere*, D. Reidel Publishing Company, Holland.

Brasseur, G. P., J. J. Orlando, and G. S. Tyndall (Eds.) (1999), *Atmospheric Chemistry and Global Change*, Oxford University Press, New York, NY, USA.

Brewer, A. W., C. T. McElroy, and J. B. Kerr (1973), Nitrogen dioxide concentrations in the atmosphere, *Nature*, *246*, 129–133.

Burrows, J. P., A. Dehn, B. Deters, S. Himmelmann, A. Richter, S. Voigt, and J. Orphal (1998), Atmospheric remote-sensing reference data from GOME: Part 1- Temperature dependent absorption cross-sections of NO_2 in the 231–794 nm range, *J. Quant. Spectrosc. Radiat. Transfer*, *60*, 1025–1031.

Burrows, J. P., A. Richter, A. Dehn, B. Deters, S. Himmelmann, S. Voigt, and J. Orphal (1999a), Atmospheric remote-sensing reference data from GOME: Part 2- Tempera-

ture dependent absorption cross-sections of O_3 in the 231–794 nm range, *J. Quant. Spectrosc. Radiat. Transfer*, *61*, 509–517.

Burrows, J. P., M. Weber, M. Buchwitz, V. Rozanov, A. Ladstätter-Weißenmayer, A. Richter, R. de Beek, R. Hoogen, K. Bramstedt, K. U. Eichmann, M. Eisinge, and D. Perner (1999b), The global ozone monitoring experiment (GOME): Mission concept and first scientific results, *J. Atmos. Sci.*, *56*, 151–175.

Canty, T., E. D. Reviére, R. J. Salawitch, G. Berthet, J. B. Renard, K. Pfeilsticker, M. Dorf, A. Butz, H. Bösch, R. M. Stimpfle, D. M. Wilmouth, E. C. Richard, D. W. Fahey, P. J. Popp, M. R. Schoeberl, L. R. Lait, and T. P. Bui (2005), Nighttime OClO in the winter Arctic vortex, *J. Geophys. Res.*, *110*, doi:101029/2004JD005035.

Carslaw, K. S., B. P. Luo, S. L. Clegg, T. Peter, P. Brimblecombe, and P. J. Crutzen (1994), Stratospheric aerosol growth and HNO_3 gas phase depletion from coupled HNO_3 and water uptake by liquid particles, *Geophys. Res. Lett.*, *21*, 2479–2482.

Chance, K., T. P. Kurosu, and C. E. Sioris (2005), Undersampling correction for array detector-based satellite spectrometers, *Appl. Opt.*, *44*, 1296–1304.

Chance, K. V., and R. J. D. Spurr (1997), Ring effect studies: Rayleigh scattering, including molecular parameters for rotational Raman scattering, and the Fraunhofer spectrum, *Appl. Opt.*, *36*, 5224–5230.

Chang, Y. S., and J. H. Shaw (1977), A nonlinear least squares method of determining line intensities and half-widths, *Appl. Spec.*, *31*, 213–220.

Chapman, S. (1930), On ozone and atomic oxygen in the upper atmosphere, *Phil. Mag.*, *10*, 369.

Chipperfield, M. P. (1999), Multiannual simulations with a three-dimensional chemical transport model, *J. Geophys. Res.*, *34*, 1781–1805.

Chipperfield, M. P. (2006), New version of the TOMCAT/SLIMCAT Off-Line Chemical Transport Model, in press.

Chipperfield, M. P., and J. A. Pyle (1998), Model sensitivity studies of Arctic ozone depletion, *J. Geophys. Res.*, *103*, 28,389–28,403.

Christensen, T., B. M. Knudsen, M. Streibel, S. B. Andersen, A. Benesova, G. Braathen, H. Claude, J. Davies, H. de Backer, H. Dier, V. Dorokhov, M. Gerding, M. Gil, B. Henchoz, H. Kelder, R. Kivi, E. Kyrö, Z. Litynska, D. Moore, G. Peters, P. Skrivankova, R. Stübi, T. Turunen, G. Vaughan, P. Viatte, A. F. Vik, P. von der Gathen, and I. Zaitcev (2005), Vortex-averaged Arctic ozone depletion in the winter 2002/2003, *Atmos. Chem. Phys.*, *5*, 131–138.

Christiansen, B. (2003), Evidence for nonlinear climate change: Two stratospheric regimes and a regime shift, *J. Clim.*, *16*, 3681–3690.

Cicerone, R. J., R. S. Stolarski, and S. Walters (1974), Stratospheric ozone destruction by man-made chlorofluoromethanes, *Science*, *185*, 1165–1167.

Collins, R. L., K. P. Bowman, and C. S. Gardner (1993), Polar stratospheric clouds at the South Pole in 1990: Lidar observations and analysis, *J. Geophys. Res.*, *98*, 1001–1010.

Crutzen, P. J. (1970), The influence of nitrogen oxide on the atmospheric ozone content, *Q. J. Roy. Met. Soc.*, *96*, 320–327.

Crutzen, P. J., and C. Brühl (2001), Catalysis by NO_x as the main cause of the spring to fall stratospheric ozone decline in the Northern Hemisphere, *J. Phys. Chem.*, *105*, 1579–1582.

Cunnold, D. M., E. S. Yang, M. J. Newchurch, G. C. Reinsel, J. M. Zawodny, and J. M. Russell-III (2004), Comment on Enhanced upper stratospheric ozone: Sign of

recovery or solar cycle effect? by W. Steinbrecht et al., *J. Geophy. Res.*, *109*, doi: 10.1029/2004JD004826.

de Valk, J. P., A. P. Goede, A. R. W. de Jonge, J. Mees, B. Franke, S. Crewell, H. Kullmann, J. Urban, J. Wohlgemuth, M. P. Chipperfield, and A. M. Lee (1997), Airborne heterodyne measurements of stratospheric ClO, HCl, O_3, and N_2O during SESAME 1 over Northern Europe, *J. Geophys. Res.*, *2*, 1391–1398.

de Grandpré, J., S. R. Beagley, V. I. Fomichev, E. Griffioen, J. C. McConnell, A. S. Medvedev, and T. G. Shepherd (2000), Ozone climatology using interactive chemistry: Results from the Canadian Middle Atmosphere Model, *J. Geophys. Res.*, *105*, 385–431.

Deshler, T., A. Adriani, G. P. Gobbi, D. J. Hoffman, G. D. Donfrancesco, and B. J. Johnson (1992), Volcanic aerosol and ozone depletion within the Antarctic polar vortex during the austral spring of 1991, *Geophys. Res. Lett.*, *19*, 1819–1822.

Dessler, A. E. (2000), *The Chemistry and Physics of Stratospheric Ozone*, Academic Press, San Diego, California, USA.

Dessler, A. E., M. D. Burrage, J. U. Grooß, J. R. Holton, J. L. Lean, S. T. Massie, M. R. Schoeberl, A. R. Douglass, and C. H. Hackman (1998), Selected science highlights from the first 5 years of the Upper Atmosphere Research Satellite (UARS) program, *Rev. Geophys.*, *36*, 183–210.

Donovan, D. P., H. Fast, Y. Makino, J. C. Bird, A. I. Carswell, J. Davies, T. J. Duck, J. W. Kaminski, C. T. McElroy, R. L. Mittermeier, S. R. Pal, V. Savastiouk, D. Velkov, and J. A. Whiteway (1997), Ozone, column ClO, and PSC measurements made at the NDSC Eureka observatory (80ºN, 86ºW) during the spring of 1997, *Geophys. Res. Lett.*, *24*, 2709–2712.

Douglas, A. E., and K. P. Huber (1965), The absorption spectrum of NO_2 in 3700-4600 Aº region, *Can. J. Phys.*, *43*, 74–81.

Fahey, D. W., S. Solomon, S. R. Kawa, M. Loewenstein, J. R. Podolske, S. E. Strahan, and K. R. Chan (1990), A diagnostic for denitrification in the winter polar stratospheres, *Nature, 345*, 698–702.

Fahre Vik, A. (2003), *NADIR News*, vol. 2, Norwegian Institute for Air Research.

Farman, J. C., B. G. Gardiner, and J. D. Shanklin (1985), Large ozone losses in Antarctica reveal seasonal ClO_x/NO_x interaction, *Nature, 315*, 207–210.

Fayt, C., and M. van Roozendael (2001), *WinDOAS 2.1 - Software user manual*, BIRA-IASB, Uccle, Belgium.

Feng, W., M. P. Chipperfield, S. Davies, B. Sen, G. Toon, J. F. Blavier, C. R. Webster, C. M. Volk, A. Ulanovsky, F. Ravegnani, P. von der Gathen, H. Jost, E. C. Richard, and H. Claude (2005), Three-dimensional model study of the Arctic ozone loss in 2002/2003 and comparison with 1999/2000 and 2003/4, *Atmos. Chem. and Phys., 5*, 139–152.

Fioletov, V. E., and W. F. J. Evans (1997), The influence of ozone and other factors on surface radiation, *Ozone science: a Canadian perspective on the changing ozone layer*, *30*, 73–90, environment Canada Report CARD 97-3, (Editors) D.I.Wardle, J.B. Kerr, C.T. McElroy and D.R. Francis.

Fioletov, V. E., and T. G. Shepherd (2003), Seasonal persistence of midlatitude total ozone anomalies, *Geophys. Res. Lett., 30*, doi:10.1029/2002GL016739.

Fioletov, V. E., J. B. Kerr, D. I. Wardle, J. Davies, E. W. Hare, C. T. McElroy, and D. W. Tarasick (1997), Long-term ozone decline over the Canadian Arctic to early 1997 from ground-based and balloon observations, *Geophy. Res. Lett., 24*, 2705–2708.

Fioletov, V. E., G. E. Bodeker, A. J. Miller, R. D. McPeters, and R. Stolarski (2002),

Global and zonal total ozone variations estimated from ground-based and satellite measurements: 1964-2000, *J. Geophy. Res.*, *107*, doi:10.1029/2001JD001350.

Fish, D. J. (1994), *Measurements of stratospheric composition using ultraviolet and visible spectroscopy*, Cambridge University Press, Cambridge, UK, Ph.D. Thesis.

Fish, D. J., and R. L. Jones (1995), Rotational Raman scattering and the Ring effect in zenith-sky spectra, *Geophys. Res. Lett.*, *22*, 811–814.

Fleig, A. J., P. K. Bhartia, C. G. Wellemeyer, and D. S. Silberstein (1986), 7 years of total ozone from the TOMS instrument - A report on data quality, *Geophys. Res. Lett.*, *13*, 1355–1358.

Fortuin, J. P. F., and H. Kelder (1998), An ozone climatology based on ozonesonde and satellite measurements, *J. Geophys. Res.*, *103*, 31,709–31,734.

Gao, R. S., P. J. Popp, E. A. Ray, K. H. Rosenlof, M. J. Northway, D. W. Fahey, A. F. Tuck, C. R. Webster, D. F. Hurst, S. M. Schauffler, H. Jost, and T. P. Bui (2002), Role of NO_y as a diagnostic of small-scale mixing in a denitrified polar vortex, *J. Geophys. Res.*, *107*, doi:10.1029/2002JD002332.

Gardner, D. (2003), Taking a closer look at camera specifications, *Photonics Spectra*, pp. 84–90.

Goldman, A., C. Paton-Walsh, W. Bell, G. C. Toon, J. F. Blavier, B. Sen, M. T. Coffey, J. W. Hannigan, and W. G. Mankin (1999), Network for the detection of stratospheric change fourier transform infrared intercomparison at Table Mountain Facility, November 1996, *J. Geophys. Res.*, *104*, 30,481–30,503.

Goody, R. M., and Y. L. Yung (1989), *Atmospheric Radiation Theoretical Basis*, Oxford University Press, New York, NY, USA, second edition.

Grainger, J. F., and J. F. Ring (1962), Anomalous Fraunhofer line profiles, *Nature*, *193*, 762.

Greenblatt, G. D., J. J. Orlando, J. B. Burkholder, and A. R. Ravishankara (1990), Absorption measurements of oxygen between 330 and 1140 nm, *J. Geophys. Res.*, *95*, 18,577–18,582.

Grooß, J. U., G. Gunther, R. Müller, P. Konopka, S. Bausch, H. Schlager, C. Voigt, C. M. Volk, and G. C. Toon (2005), Simulation of denitrification and ozone loss for the Arctic winter 2002/2003, *Atmos. Chem. Phys.*, *5*, 1437–1448.

Hampson, J. (1964), *Photochemical Behavior of the Ozone Layer*, Can. Armament Res. and Dev. Estab., Valcartier, Quebec, Canada, Tech. Note 1627/64.

Hansen, J. E., and L. D. Travis (1974), Light scattering in planetary atmospheres, *Space Sci. Rev.*, pp. 16,527–16,610.

Harvey, V. L., and M. H. Hitchman (1996), A climatology of the Aleutian High, *J. Atmos. Sci.*, *53*, 2088–2101.

Hase, F. (2000), Inversion von spurengasprofilen aus hochaufgelösten bodengebundenen FTIR–Messungen in absorption, *FZK Report No. 6512*.

Hase, F., J. W. Hannigan, M. T. Coffey, A. Goldman, M. Höpfner, N. B. Jones, C. P. Rinsland, and S. W. Wood (2004), Intercomparison of retrieval codes used for the analysis of high-resolution, ground-based FTIR measurements, *J. Quant. Spectrosc. Radiat. Transfer*, *87*, 25–52.

Hecht, E. (1998), *Optics*, Addison Wesley Longman Inc., Reading, UK, third edition.

Henriksen, K., S. H. H. Larsen, O. I. Shumilov, and B. Thorkelsson (1994), Ozone variations in the Scandinavian sector of the Arctic during the AASE campaign and 1989, *J. Atmos. Sci.*, *21*, 1775–1778.

Hofmann, D. J., and T. Deshler (1991), Evidence from balloon measurements for chemical depletion of stratospheric ozone in the Arctic winter of 1989–90, *Nature, 349*, 300–305.

Hofmann, D. J., J. W. Harder, S. R. Rolf, and J. M. Rosen (1987), Balloon-borne observations of development and vertical structure of the Antarctic ozone hole in 1986, *Nature, 326*, 59–62.

Hofmann, D. J., S. J. Oltmans, J. M. Harris, B. J. Johnson, and J. A. Lathrop (1997), Ten years of ozonesonde measurements at the South Pole: Implications for recovery of springtime Antarctic ozone, *J. Geophys. Res., 102*, 8931–8943.

Höiskar, B. A. K., A. Dahlback, G. Vaughan, G. O. Braathen, F. Goutail, J. P. Pommereau, and R. Kivi (1997), Interpretation of ozone measurements by ground-based visible spectroscopy - A study of the seasonal dependence of airmass factors for ozone based on climatology data, *J. Quant. Spectros. Radiat. Transfer, 57*, 569–579.

Holton, J. R. (2004), *An Introduction to Dynamic Meteorology*, Elsevier Academic Press, Amsterdam, Holand, fourth Edition.

Höpfner, M., G. P. Stiller, M. Kuntz, T. von Clarmann, G. Echle, B. Funke, N. Glatthor, F. Hase, H. Kemnitzer, and S. Zorn (1998), The Karlsruhe optimized and precise radiative transfer algorithm, Part II: Interface to retrieval applications, *SPIE Proceedings, 3501*, 1860–195.

Houghton, J. (2002), *The Physics of Atmospheres*, Cambridge University Press, Cambridge, UK, third edition.

Jackman, C. H., and A. R. Douglass (2003), Overview of the Upper Atmosphere Research Satellite: Observations from 1991 to 2002, *Adv. Space Res., 31*, 2101–2104.

Jha, N. (1999), Remote sounding of atmospheric composition, *Internal report*, University of Toronto.

Johnston, J. S. (1971), Reduction of stratospheric ozone by nitrogen oxide catalysts from supersonic transport exhaust, *Science*, *173*, 517.

Kerzenmacher, T. E., K. A. Walker, K. Strong, R. Berman, P. F. Bernath, C. D. Boone, J. R. Drummond, H. Fast, A. Fraser, K. MacQuarrie, C. Midwinter, K. Sung, C. T. McElroy, R. L. Mittermeier, J. Walker, and H. J. Wu (2005), Measurements of O_3, NO_2 and temperature during the 2004 Canadian Arctic ACE validation campaign, *Geophys. Res. Lett.*, *32*, doi:10.1029/2005GL023032.

Kondo, Y., H. Irie, M. Koike, and G. E. Bodeker (2000), Denitrification and nitrification in the Arctic stratosphere during the winter of 1996–1997, *Geophys. Res. Lett.*, *27*, 337–340.

Koop, T., B. P. Luo, U. M. Biermann, P. J. Crutzen, and T. Peter (1997), Freezing of $HNO_3/H_2SO_4/H_2O$ solutions at stratospheric temperatures: Nucleation statistics and experiments, *J. Phys. Chem. A*, *101*, 1117–1133.

Kromminga, H., J. Orphal, P. Spietz, S. Voigt, and J. P. Burrows (2003), New measurements of OClO absorption cross sections in the 325–435 nm region and their temperature dependence between 213 and 293 k, *J. Photochem. Photobio. A*, *157*, 149–160.

Kühl, S., A. Dörnbrack, W. Wilms-Grabe, B. M. Sinnhuber, U. Platt, and T. Wagner (2004), Observational evidence of rapid chlorine activation by mountain waves above Northern Scandinavia, *J. Geophys. Res.*, *109*, doi:10.1029/2004JD004797.

Kuntz, M., M. Höpfner, G. P. Stiller, T. von Clarmann, G. Echle, B. Funke, N. Glatthor, F. Hase, H. Kemnitzer, and S. Zorn (1998), The Karlsruhe optimized and precise radiative transfer algorithm, Part III: ADDLIN and TRANSF algorithms for modeling spectral transmittance and radiance, *SPIE Proceedings*, *3501*, 247–256.

Kurucz, R. L., I. Furenlid, J. Brault, and L. Testerman (1984), Solar flux atlas from 296 nm to 1300 nm, *National Solar Observatory Atlas No. 1*.

Lambert, J. C., J. Granville, M. van Roozendael, A. Sarkissian, F. Goutail, J. F. Müller, J. P. Pommereau, and J. M. Russell-III (1999), A climatology of NO_2 profile for improved air mass factors for ground-based vertical column measurements, in stratospheric ozone 1999, *Air Pollution Research Report 73 (CEC DG XII)*, pp. 703–706.

Lanzante, J. R., S. A. Klein, and D. J. Seidel (2003), Temporal homogenization of monthly radiosonde temperature data. Part II: Trends, sensitivities, and MSU comparison, *J. Clim.*, *16*, 241–262.

Lefevre, F., G. P. Brasseur, I. Folkins, A. K. Smith, and P. Simon (1994), Chemistry of the 1991-1992 stratospheric winter - 3-dimensional model simulations, *J. Geophys. Res.*, *99*, 8183–8195.

Liou, K. N. (1980), *An Introduction to Atmospheric Radiation*, Academic Press, New York, NY, USA.

Longhurst, R. S. (1973), *Geometrical and Physical Optics*, Longman Group Limited, London, UK.

Lukyanov, A. N., H. Nakane, and V. A. Yushkov (2003), Lagrangian estimations of ozone loss in the core and edge region of the Arctic polar vortex 1995/1996: Model results and observations, *J. Atmos. Chem.*, *44*, 191–210.

Mackay, C. (1986), Charge-coupled devices in Astronomy, *Annual Rev. Astronomy Astrophys.*, *24*, 255–283.

Manney, G. L., L. Froidevaux, J. W. Waters, R. W. Zurek, W. G. Read, L. S. Elson, J. B. Kumer, J. L. Mergenthaler, A. E. Roche, A. O'Neill, R. S. Harwood, I. MacKenzie, and R. Swinbank (1994), Chemical depletion of ozone in the Arctic lower stratosphere during winter 1992-93, *Nature*, *370*, 429–434.

Manney, G. L., R. W. Zurek, L. Froidevaux, and J. W. Waters (1995), Evidence for Arctic ozone depletion in late February and early March 1994, *Geophys. Res. Lett.*, *22*, 2941–2944.

Manney, G. L., W. A. Lahoz, R. Swinbank, A. O'Neill, P. M. Connew, and R. W. Zurek (1999), Simulation of the December 1998 stratospheric major warming, *Geophys. Res. Lett.*, *26*, 2733–2736.

Manney, G. L., K. Krüer, J. L. Sabutis, S. A. Sena, and S. Pawson (2005), The remarkable 2003/2004 winter and other recent warm winters in the Arctic stratosphere since the late 1990s, *J. Geophys. Res.*, *110*, doi:10.1029/2004JD005367.

McElroy, M. B., R. J. Salawitch, S. C. Wofsy, and J. A. Logan (1986), Reductions of Antarctic ozone due to synergistic interactions of chlorine and bromine, *Nature*, *321*, 759–762.

McIntyre, M. E. (1992), Atmospheric dynamics: Some fundamentals, with observational implications, in *AD92–Proceedings of International School of Physics - 92*, pp. 313–386, Editors J. C. Gille and G. Visconti, North-Holland.

McKenzie, R. L., P. V. J. C. T. McElroy, J. B. Kerr, and S. Solomon (1991), Altitude distribution of stratospheric constituents from ground-based measurements at twilight, *J. Geophys. Res.*, *96*, 15,499–15,511.

McLinden, C. A. (1998), *Observation of atmospheric composition from NASA ER-2 spectroradiometer measurements*, York University, Toronto, Canada, Ph.D. Thesis.

McLinden, C. A., J. C. McConnell, E. Griffioen, and C. T. McElroy (2002), A vector radiative transfer model for the Odin/OSIRIS project, *Can. J. Phys.*, *80*, 375–393.

Meier, A., C. P. Walsh, W. Bell, T. Blumenstock, F. Hase, A. Goldman, Å.Steen, R. Kift, P. Woods, and Y. Kondo (2005), Evidence of reduced measurement uncertainties from

an FTIR instrument intercomparison at Kiruna, Sweden, *J. Quant. Spectrosc. Radiat. Transfer*, *96*, 75–84.

Molina, M. J., and M. J. Molina (1987), Production of Cl_2O_2 from the self reaction of the ClO radical, *J. Chem. Phys.*, *91*, 433–436.

Molina, M. J., and F. S. Rowland (1974), Stratospheric sink for chlorofluoromethanes: Chlorine atom catalyzed destruction of ozone, *Nature*, *249*, 1756–1758.

Müller, R., P. J. Crutzen, J. U. Grooß, C. Brühl, J. M. Russell-III, H. Gernandt, D. S. McKenna, and A. F. Tuck (1997), Severe chemical ozone loss in the Arctic during the winter of 1995-96, *Nature*, *389*, 709–712.

Murphy, C., W. Bell, P. Woods, P. Demoulin, B. Galle, J. Mellqvist, W. Arlander, J. Notholt, A. Goldman, G. C. Toon, J. F. Blavier, B. Sen, M. T. Coffey, J. W. Hannigan, W. G. Mankin, N. Jones, D. Griffith, A. Meier, T. Blumenstock, H. Fast, R. Mittermeier, and Y. Makino (2001), Validation of NDSC measurements of ozone, reservoir compounds and dynamical tracers: Results of a series of side-by-side instrument intercomparisons, NDSC 2001 Symposium, Arcachon, France, 24–27 September.

Murtagh, D., U. Frisk, F. Merino, M. Ridal, A. Jonsson, J. Stegman, G. Witt, P. Eriksson, C. Jimenez, G. Megie, J. de la Noe, P. Ricaud, P. Baron, J. R. Pardo, A. Hauchcorne, E. J. Liewellyn, D. A. Degenstein, R. L. Gattinger, N. D. Lioyd, W. F. J. Evans, I. C. McDade, C. S. Haley, C. Sioris, C. von Savigny, B. H. Solheim, J. C. McConnell, K. Strong, E. H. Richardson, G. W. Leppelmeier, E. Kyrolo, H. Auvinen, and L. Oikarinen (2002), An overview of the Odin atmospheric mission, *Can. J. Phys.*, *80*, 309–319.

Newchurch, M. J., E. S. Yang, D. M. Cunnold, G. C. Reinsel, J. M. Zawodny, and J. M. Russell-III (2003), Evidence for slowdown in stratospheric ozone loss: First stage of ozone recovery, *J. Geophy. Res.*, *108*, doi:10.1029/2003JD003471.

Newman, P. A. (1998), Preserving Earth's stratosphere, *American Soc. Mech. Eng.*, feature Article.

Newman, P. A., N. R. P. Harris, and A. Adriani (2002), An overview of the SOLVE–THESEO 2000 campaign, *J. Geophys. Res.*, *107*, doi:10.1029/2001JD001303.

Notholt, J. (1994a), The moon as a light source for FTIR measurements of stratospheric trace gases during polar night: Application for HNO_3 in the Arctic, *J. Geophys. Res.*, *99*, 3607–3614.

Notholt, J. (1994b), FTIR measurements of HF, N_2O and CFCs during the Arctic polar night with the moon as light source, subsidence during winter 1992/93, *Geophys. Res. Lett.*, *21*, 2385–2388.

Notholt, J., R. Neuber, O. Schrems, and T. V. Clarman (1993), Stratospheric trace gas concentrations in the Arctic polar night derived by FTIR-spectroscopy with the Moon as IR light source, *Geophys. Res. Lett.*, *20*, 2059–2062.

Notholt, J., P. von der Gathen, and S. Peil (1995), Heterogeneous conversion of HCl and $ClONO_2$ during the Arctic winter 1992/1993 initiating ozone depletion, *J. Geophys. Res.*, *100*, 11,269–11,274.

Notholt, J., G. Toon, F. Stordal, S. Solberg, N. Schmidbauer, E. Becker, A. Meier, and B. Sen (1997), Seasonal variations of atmospheric trace gases in the high Arctic at 79°N, *J. Geophys. Res.*, *102*, 12,855–12,861.

Noxon, J. P. (1975), Nitrogen dioxide in the stratosphere and troposphere measured by groundbased absorption spectroscopy, *Science*, *189*, 547–549.

Offermann, D., M. Donner, P. Kneiling, and B. Naujokat (2004), Middle atmosphere temperature changes and the duration of summer, *Sol. Terr. Phys.*, *66*, 437–450.

Olson, J. R., J. V. Allen, P. F. Fogal, F. J. Murcray, and A. Goldman (1996), Calibrated 0.1-cm^{-1} IR emission spectra from 80°N, *Applied Optics*, *35*, 2797–2801.

Panel on Climate Change, I. (2005), *Safeguarding the ozone layer and the global climate system, issues related to haydrofluorocarbons and perfluorocarbons*, Special report of the IPCC/TEAP, Switzerland.

Perrin, F. H. (1948), Whose absorption law?, *J. Opt. Soc. America*, *38*, 72–74.

Pfeilsticker, K., D. W. Arlander, J. P. Burrows, F. Erle, M. Gil, F. Goutail, C. Hermans, J. C. Lambert, U. Platt, J. P. Pommereau, A. Richter, A. Sarkissian, M. V. Roozendael, T. Wagner, and T. Winterrath (1999b), Intercomparison of the influence of tropospheric clouds on UV-visible absorptions detected during the NDSC intercomparison campaign at OHP in June 1996, *Geophys. Res. Lett.*, *26*, 1169–1172.

Pierce, R. B., and T. D. A. Fairlie (1993), Chaotic advection in the stratosphere - Implications for the dispersal of chemically perturbed air from the polar vortex, *J. Geophys. Res.*, *98*, 18,589–18,595.

Platt, U. (1994), *Air Monitoring by Spectroscopic Techniques*, John Wiley and Sons Inc., London, UK, editor M. W. Sigrist.

Pommereau, J. P., and U. Schmidt (1991), CHEOP-III - An ozone research campaign in the Arctic winter stratosphere 1989/90, *Geophys. Res. Lett.*, *18*, 759–762.

Popp, P. J., M. J. Northway, J. C. Holecek, R. S. Gao, D. W. Fahey, J. W. Elkins, D. F. Hurst, P. A. Romashkin, G. C. Toon, B. Sen, S. M. Schauffler, R. J. Salawitch, C. R. Webster, R. L. Herman, H. Jost, T. P. Bui, P. A. Newman, and L. R. Lait (2001), Severe and extensive denitrification in the 1999–2000 Arctic winter stratosphere, *Geophys. Res. Lett.*, *28*, 2875–2878.

Preston, K. E. (1995), *The retrieval of* NO$_2$ *vertical profiles from ground-based twilight UV-visible absorption measurements*, Cambridge University, Cambridge, UK, Ph.D. Thesis.

Preston, K. E., R. L. Jones, and H. K. Roscoe (1997), Retrieval of NO$_2$ vertical profiles from ground-based UV-visible measurements: Method and validation, *J. Geophys. Res.*, *102*, 19,089–19,097.

Proffitt, M. H., J. J. Margitan, K. K. Kelly, M. Loewenstein, J. R. Podolske, and K. R. Chan (1990), Ozone loss in the Arctic polar vortex inferred from high altitude aircraft measurements, *Nature*, *347*, 31–36.

Proffitt, M. H., K. Aikin, J. J. Margitan, M. Loewenstein, J. R. Podolske, A. Weaver, K. R. Chan, H. Fast, and J. W. Elkins (1993), Ozone loss inside the northern polar vortex during the 1991-1992 winter, *Science*, *261*, 1150–1154.

Pyle, J. A., N. R. P. Harris, J. C. Farman, F. Arnold, G. Braathen, R. A. Cox, P. Faucon, R. L. Jones, G. Megie, A. O'Neil, U. Platt, J. P. Pommereau, U. Schmidt, and F. Stordal (1994), An overview of the EASOE campaign, *Geophy. Res. Lett.*, *21*, 1191–1194.

Ramaswamy, V., M. L. Chanin, J. Angell, J. Barnett, D. Gaffen, M. Gelman, P. Keckhut, Y. Koshelkov, K. Labitzke, J. J. R. Lin, A. O'Neill, J. Nash, W. Randel, R. Rood, K. Shine, M. Shiotani, and R. Swinbank (1994), Stratospheric temperature trends: Observations and model simulations, *Rev. Geophys.*, *39*, 71–122.

Randel, W. J., and F. Wu (1995), TOMS total ozone in potential vorticity coordinates, *Geophys. Res. Lett.*, *22*, 683–686.

Randel, W. J., and F. Wu (1999), Cooling of the Arctic and Antarctic polar stratospheres due to ozone depletion, *Geophys. Res. Lett.*, *12*, 1467–1479.

Renard, J. B., M. Chartierand, G. Berthet, C. Robert, M. Pirre, and F. G. Taupin (1999a), A new light balloon-borne UV-visible spectrometer designed for night-time observations of stratospheric trace gas species, in *ES99–Proceedings of 14th ESA Symposium*, pp. 101–104, ESA Spec. Publ., SP-437, Potsdam, Germany.

Renard, J. B., F. G. Taupin, E. D. Reviére, M. Pirre, N. Huret, G. Berthet, C. Robert, and M. Chartier (2001), Measurements and simulation of stratospheric NO$_3$ at mid and high latitudes in the Northern Hemisphere, *J. Geophys. Res.*, *106*, 32,387–32,399.

Rex, M. (2005), Polar processes, *GCC Summer School*.

Rex, M., N. R. P. Harris, P. von der Gathen, R. Lehmann, G. O. Braathen, E. Reimer, A. Beck, M. P. Chipperfield, R. Alfier, M. Allaart, F. O'Connor, H. Dier, V. Dorokhov, H. Fast, M. Gil, E. Kyrö, Z. Litynska, I. S. Mikkelsen, M. G. Molyneux, H. Nakane, J. Notholt, M. Rummukainen, P. Viatte, and J. Wenger (1997), Prolonged stratospheric ozone loss in the 1995-96 Arctic winter, *Nature*, *389*, 835–838.

Rex, M., P. von der Gathen, G. O. Braathen, N. R. P. Harris, E. Reimer, A. Beck, R. Alfier, R. Kruger-Carstensen, M. P. Chipperfield, H. de Backer, D. Balis, F. O'Connor, H. Dier, V. Dorokhov, H. Fast, A. Gamma, M. Gil, E. Kyrö, Z. Litynska, S. Mikkelsen, M. Molyneux, G. Murphy, S. J. Reid, M. Rummukainen, and C. Zerefos (1999), Chemical ozone loss in the Arctic winter 1994/95 as determined by the Match technique, *J. Atmos. Chem.*, *32*, 35–39.

Rex, M., R. J. Salawitch, P. von der Gathen, N. R. P. Harris, M. P. Chipperfield, and B. Naujokat (2004), Arctic ozone loss and climate change, *Geophys. Res. Lett.*, *31*, doi:101029/2003GL018844.

Rinsland, C. P., M. A. H. Smith, P. L. Rinsland, A. Goldman, J. W. Brault, and G. M. Stokes (1982), Ground-based infrared spectroscopic measurements of atmospheric hydrogen cyanide, *J. Geophys. Res.*, *87*, 11,119–11,125.

Rinsland, C. P., A. Goldman, F. J. Murcray, F. H. Murcray, R. D. Blatherwick, and D. G. Murcray (1988), Infrared measurements of atmospheric gases above Mauna Loa, Hawaii, in February 1987, *J. Geophys. Res.*, *91*, 12,607–12,626.

Rinsland, C. P., R. Zander, E. Mahieu, L. S. Chiou, A. Goldman, and N. B. Jones (2002), Stratospheric HF column abundances above Kitt Peak (31.9ºN latitude): Trends from 1977 to 2001 and correlations with stratospheric HCl columns, *J. Quant. Spectrosc. Radiat. Transfer*, *74*, 205–216.

Rinsland, C. P., C. Boone, R. Nassar, K. Walker, P. Bernath, E. Mahieu, R. Zander, J. C. McConnell, and L. Chiou (2005), Trends of HF, HCl, CCl_2F_2, CCl_3F, $CHClF_2$, (HCFC-22), and SF_6 in the lower stratosphere from Atmospheric Chemistry Experiment (ACE) and Atmospheric Trace Molecule Spectroscopy (ATMOS) measurements near 30ºN latitude, *Geophys. Res. Lett.*, *32*, doi:10.1029/2005GL022415.

Rodgers, C. D. (1976), Retrieval of atmospheric temperature and composition from remote measurements of thermal radiation, *Rev. Geophys. Space Phys.*, *14*, 609–624.

Rodgers, C. D. (1990), The characterization and error analysis of profiles retrieved from remote sounding measurements, *J. Geophys. Res.*, *95*, 5587–5595.

Rodgers, C. D. (2000), *Inverse Methods for Atmospheric Sounding - Theory and Practice*, World Scientific Publishing, Singapore, series on atmospheric, ocean and planetary physics - Vol.2.

Rodgers, C. D., and B. J. Connor (2003), Intercomparison of remote sounding instruments, *J. Geophys. Res.*, *108*, doi:10.1029/2002JD002299.

Roscoe, H. K., D. J. Fish, and R. L. Jones (1996), Interpolation errors in UV-visible spectroscopy for stratospheric sensing: Implications for sensitivity, spectral resolution, and spectral range, *Appl. Opt.*, *35*, 427–432.

Rothman, L. S., C. P. Rinsland, A. Goldman, S. T. Massie, D. P. Edwards, J. M. Flaud, A. Perrin, C. Camy-Peyret, V. Dana, J. Y. Mandin, J. Schroeder, A. McCann, R. R. Gamache, R. B. Wattson, K. Yoshino, K. Chance, K. Jucks, L. R. Brown, V. Nemtchinov, and P. Varanasi (1998), The HITRAN molecular spectroscopic database and HAWKS (HITRAN Atmospheric Workstation): 1996 Edition, *J. Quant. Spectros. Radiat. Transfer*, *60*, 665–710.

Sander, S. P. (1986), Temperature dependence of the NO_3 absorption spectrum, *J. Phys. Chem.*, *90*, 4135–4142.

Sander, S. P., A. R. Ravishankara, and R. R. Friedl (2003), Chemical kinetics and photochemical data for use in stratospheric modeling, *JPL Publication*, pp. 2–25, update to Evaluation no. 14.

Sankey, D., and T. G. Shepherd (2003), Correlations of long-lived chemical species in a middle atmosphere general circulation model, *J. Geophys. Res.*, *108*, doi: 10.1029/2002JD002799.

Santee, M. L., G. L. Manney, N. J. Livesey, and J. W. Waters (2000), UARS Microwave Limb Sounder observations of denitrification and ozone loss in the 2000 Arctic late winter, *Geophys. Res. Lett.*, *27*, 3213–3216.

Santee, M. L., G. L. Manney, N. J. Livesey, and W. G. Read (2004), Three-dimensional structure and evolution of stratospheric HNO_3 based on UARS Microwave Limb Sounder measurements, *J. Geophys. Res.*, *109*, doi:10.1029/2004JD004578.

Schnadt, C., and M. Dameris (2003), Relationship between North Atlantic Oscillation changes and stratospheric ozone recovery in the Northern Hemisphere in a chemistry-climate model, *Geophys. Res. Lett.*, *30*, doi:10.1029/2003GL017006.

Schnadt, C., M. Dameris, M. Ponater, R. Hein, V. Grewe, and B. Steil (2002), Interaction

of atmospheric chemistry and climate and its impact on stratospheric ozone, *Clim. Dynamics*, *18*, doi:10.1007/s00382-001-0190-z.

Schoeberl, M. R., A. R. Douglass, E. Hilsenrath, and P. K. Bhartia (2006), Overview of the EOS Aura mission, in press.

Schofield, R., K. Kreher, B. J. Connor, P. V. Johnston, A. Thomas, D. Shooter, M. P. Chipperfield, C. D. Rodgers, and G. H. Mount (2004), Retrieved tropospheric and stratospheric BrO columns over Lauder, New Zealand, *J. Geophys. Res.*, *109*, doi: 10.1029/2003JD004463.

Schreiber, J., T. Blumenstock, and F. Hase (1997), Application of a radiometric calibration method to lunar Fourier transform IR spectra by using a liquid-nitrogen-cooled high-emissivity blackbody, *Appl. Opt.*, *36*, 8168–8172.

Schreiner, J., C. Voigt, A. Kohlmann, F. Anold, K. Mauersberger, and N. Larsen (1999), Chemical analysis of polar stratospheric cloud particles, *Science*, *283*, 968–970.

Senne, T., J. Stutz, and U. Platt (1996), Measurement of the latitudinal distribution of NO_2 column density and layer height in Oct-Nov 1993, *Geophys. Res. Lett.*, *23*, 805–808.

Shepherd, G. G. (2002), *Spectral Imaging of the Atmosphere*, Academic Press, Elsevier Science Limited, London, UK.

Shepherd, T. G. (2003), Large-scale atmospheric dynamics for atmospheric chemists, *Chem. Rev.*, *103*, 4509–4531.

Shindell, D. (2003), Whither Arctic climate?, *Science*, *299*, 215–216.

Shine, K. P., M. S. Bourqui, P. M. D. Forster, S. H. E. Hare, U. Langematz, P. Braesicke, V. Grewe, M. Ponater, C. Schnadt, C. A. Smiths, J. D. H. J. Austin, N. Butchart, D. T. Shindell, W. J. Randels, T. Nagashima, R. W. Portmann, S. Solomon, D. J. Seidel,

J. Lanzante, S. Klein, V. Ramaswamy, and M. D. Schwarzkopf (2003), A comparison of model-simulated trends in stratospheric temperatures, *Q. J. R. Meteorol. Soc.*, *129*, 1565–1588.

Sioris, C. E., W. F. J. Evans, R. L. Gattinger, I. C. McDade, D. A. Degenstein, and E. J. Llewellyn (2002), Ground-based Ring-effect measurements with the OSIRIS development model, *Can. J. Phys.*, *80*, 483–491.

Smit, H. G. J. (1996), JOSIE: The 1996 WMO international intercomparison of ozonesondes under quasi-flight conditions in the environmental chamber at Jülich, in Atmospheric Ozone, in *QOS96—Proceedings of the Quadrennial Ozone Symposium*, pp. 971–974, Editors R. D. Bojkov and G. Visconti, Parco Sci. e Tecnol. d'Abruzzo.

Solomon, S. (1990), Progress towards a quantative understanding of Antarctic ozone depletion, *Nature*, *347*, 347–354.

Solomon, S. (1999), Stratospheric ozone depletion: A review of concepts and history, *Rev. Geophys.*, *37*, 275–316.

Solomon, S., R. R. Garcia, F. S. Rowland, and D. J. Wuebbles (1986), On the Depletion of Antarctic Ozone, *Nature*, *321*, 755–758.

Staehelin, J., N. R. P. Harris, C. Appenzeller, and J. Eberhard (2001), Ozone trends: A review, *Rev. Geophys.*, *39*, 231–290.

Stolarski, R. S., A. J. Krueger, M. R. Schoeberl, R. D. McPeters, P. A. Newman, and J. C. Alpert (1986), Nimbus 7 satellite measurements of springtime Antarctic ozone decrease, *Nature*, *37*, 808–818.

Strahan, S. E., M. Loewenstein, and J. R. Podolske (1999), Climatology and small-scale structure of lower stratospheric N_2O based on in situ observations, *J. Geophys. Res.*, *104*, 219–2208.

Strong, K., G. Bailak, D. Barton, M. R. Bassford, R. D. Blatherwick, S. Brown, D. Chartrand, J. Davies, J. R. Drummond, P. F. Fogal, E. Forsberg, R. Hall, A. Joffrey, J. Kaminski, J. Kosters, C. Laurin, J. C. McConnell, C. T. McElroy, C. A. McLinden, S. M. L. Melo, K. Menzies, C. Midwinter, F. J. Murcray, C. Nowlan, R. J. Olson, B. M. Quine, Y. Rochon, V. Savastiouk, B. Solheim, D. Sommerfeldt, A. Ullberg, S. Werchohlad, H. Wu, and D. Wunch (2005), MANTRA - A balloon mission to study the odd-nitrogen budget of the stratosphere, *Atmos.-Ocean*, *43*, 283–299.

Tabazadeh, A., R. P. Turco, K. Drdla, and M. Z. Jacobson (1994), A study of type I polar stratospheric clouds formation, *Geophys. Res. Lett.*, *21*, 1619–1622.

Tabazadeh, A., M. L. Santee, M. Y. Danilin, H. C. Pumphrey, P. A. Newman, P. J. Hamill, and J. L. Mergenthaler (2000), Quantifying denitrification and its effect on ozone recovery, *Science*, *288*, 1407–1411.

Tarasick, D. W., V. E. Fioletov, D. I. Wardle, J. B. Kerr, and J. Davies (2005), Changes in the vertical distribution of ozone over Canada from ozonesondes: 1980–2001, *J. Geophys. Res.*, *110*, doi:10.1029/2004JD004643.

Toon, O. B., P. Hamill, R. P. Turco, and J. Pinto (1986), Condensation of HNO_3 and HCl in the winter polar stratosphere, *Geophys. Res. Lett.*, *13*, 1284–1287.

Toon, O. B., R. P. Turco, J. Jordan, J. Goodman, and G. Ferry (1989), Physical processes in polar stratospheric ice clouds, *J. Geophys. Res.*, *94*, 11,359–11,380.

UNEP (1998), *Environmental Effects of Ozone Depletion*, United Nations Environment Programme.

UNEP (2003), *Environmental Effects of Ozone Depletion: 2002 assessment. Photochemistry and photobiology*, 1–72 pp., United Nations Environment Programme.

Vaughan, G., P. T. Quinn, A. C. Green, J. Bean, H. K. Roscoe, M. van Roozendael, and F. Goutail (2005), SAOZ measurements of stratospheric NO$_2$ at Aberystwyth, 1991–2004, in press.

Visconti, G., and R. Garcia (1987), *Transport Processes in the Middle Atmosphere*, D. Reidel Publishing Company, NATO ASI Series, Series C: Mathematical and Physical Sciences Vol. 213.

Voigt, C., J. Schreiner, A. Kohlmann, P. Zink, K. Mauersberger, N. Larsen, T. Deshler, C. Kroger, J. Rosen, A. Adriani, F. Cairo, G. D. Donfrancesco, M. Viterbini, J. Ovarlez, H. Ovarlez, C. David, and A. Dornbrack (2000), Nitric acid trihydrate (NAT) in polar stratospheric clouds, *Science*, *290*, 1756–1758.

Wahner, A., G. S. Tyndall, and A. R. Ravishankara (1987), Absorption cross section for OClO as a function of temperature in the wavelength range 240–480 nm, *J. Phys. Chem.*, *91*, 2734–2738.

Wahner, A., A. R. Ravishankara, S. P. Sander, and R. R. Friedl (1988), Absorption cross section for BrO between 312 and 385 nm at 298 and 223 K, *Chem. Phys. Lett.*, *152*, 507–511.

Waibel, A. E., T. Peter, K. S. Carslaw, H. Oelhaf, G. Wetzel, P. J. Crutzen, U. Poschl, A. Tsias, E. Reimer, and H. Fischer (1999), Arctic ozone loss due to denitrification, *Science*, *283*, 2064–2069.

Waugh, D. W., and W. J. Randel (1999), Climatology of Arctic and Antarctic polar vortices using elliptical diagnostics, *J. Atmos. Sci.*, *56*, 1594–1613.

Wayne, R. P. (1991), *Chemistry of Atmospheres*, Oxford Science Publications, second edition.

Weaver, A., S. Solomon, R. W. Sanders, K. Arpag, and H. L. Miller-Jr. (1996), Atmospheric NO_3 5. Off-axis measurements at sunrise: Estimates of tropospheric NO_3 at 40º N, *J. Geophys. Res.*, *101*, 18,605–18,612.

Wehr, T. (2002), The European Space Agency's present and future atmospheric composition sounding missions, *Adv. Space Res.*, *29*, 1603–1608.

Williams, D. (1976), *Spectroscopy*, Academic Press, New York, NY, USA.

WMO (2003), *Scientific assessment of ozone depletion: 2002, Rep. 47, Global Ozone Research and Monitoring Project*, World Meteorological Organization, Geneva, Switzerland.

Wolfe, W. L. (1997), *Introduction to Imaging Spectrometers*, SPIE Optical Engineering Press, Washington, USA.

Wood, S. W., R. L. Batchelor, A. Goldman, C. P. Rinsland, B. J. Connor, F. J. Murcray, T. M. Stephen, and D. N. Heuff (2004), Ground-based nitric acid measurements at Arrival Heights, Antarctica, using solar and lunar Fourier transform infrared observations, *J. Geophys. Res.*, *109*, doi:10.1029/2004JD004665.

Wunch, D., M. P. Tingley, T. G. Shepherd, J. R. Drummond, G. W. K. Moore, and K. Strong (2005), Climatology and predictability of the late summer stratospheric zonal wind turnaround over Vanscoy, Saskatchewan, *Atmos.-Ocean*, *43*, 301–313.

Yokelson, R. J., J. B. Burkholder, R. W. Fox, R. K. Talukhadr, and A. R. Ravishankara (1994), Temperature dependence of the NO_3 absorption spectrum, *J. Phys. Chem.*, *98*, 13,144–13,150.